INTERNATIONAL ATOMIC ENERGY AGENCY
UNITED NATIONS EDUCATIONAL, SCIENTIFIC AND CULTURAL ORGANIZATION
INTERNATIONAL CENTRE FOR THEORETICAL PHYSICS
I.C.T.P., P.O. BOX 586, 34100 TRIESTE, ITALY, CABLE CENTRATOM TRIESTE

UNITED NATIONS INDUSTRIAL DEVELOPMENT ORGANIZATION

INTERNATIONAL CENTRE FOR SCIENCE AND HIGH TECHNOLOGY

SMR.550 - 8

SPRING COLLEGE IN MATERIALS SCIENCE ON

"NUCLEATION, GROWTH AND SEGREGATION IN MATERIALS

SCIENCE AND ENGINEERING"

(6 May - 7 June 1991)

NUCLEATION AND GROWTH OF SECOND PHASES AND RELATED INSTABILITIES

P. HAASEN
Institut für Metallphysik der
Universität Göttingen
Hospitalstrasse 3/5
D-3400 Göttingen
Germany

These are preliminary lecture notes, intended only for distribution to participants.

1429 Mat. Sci. Kap. 4

lecture Notes Haasen

-3-

4 Homogeneous Second Phase Precipitation

R. Wagner and R. Kampmann

Institut für Werkstofforschung, GKSS-Forschungszentrum GmbH, D-2054 Geesthacht, Federal Republic of Germany

Umbruch:
Fahnen:
K. Trillsch, Würzburg
1. Korr.

Verlagsgesellschaft, 6940 Weinheim
ial Science & Technology, Vol 5
ktor: Herr Schmitt

4.1 Introduction

Many technologically important properties of alloys, such as their mechanical strength and toughness, creep and corrosion resistance, and magnetic and superconducting properties, are essentially controlled by the presence of precipitated particles of a second phase. This commonly results from the decomposition of a solid solution during cooling. A fundamental understanding of the thermodynamics, the mechanism and the kinetics of precipitation reactions in metallic solids, leading to a well-defined microstructure, is therefore of great interest in materials science.

As is reflected by the schematic binary phase diagram of Fig. 4-1, for reasons of entropy the single phase state α of a solid solution with composition c_0 is thermodynamically stable only at elevated temperatures. At lower temperatures the free energy of the system is lowered through unmixing ('decomposition' or 'phase separation') of α into two phases, α' and β.

In order to initiate a precipitation reaction, the alloy is first homogenized in the single-phase region at T_H and then either

a) cooled down slowly into the two-phase region $\alpha' + \beta$, or
b) quenched into brine prior to isothermal aging at a temperature T_A within the

VCH Verlagsgesellschaft, 6940 Weinheim
Autor: Umbruch:
Material Science & Technology, Vol. 5 Fahnen:
Herausgeber: Herr Schmitt 1. Korr.: K. Tillisch, Würzburg

In both cases, thermodynamic equilibrium is reached if the supersaturation Δc, defined as

$$\Delta c(t) = \bar{c} - c_s^e \qquad (4\text{-}1)$$

becomes zero. (Here $\bar{c}(t)$ is the mean matrix composition at time t with $\bar{c}(t=0) \equiv c_0$.)

For case a), which prevails frequently during industrial processing, the aging temperature and the associated equilibrium solubility limit $c_s^e(T)$ decrease continuously. Equilibrium can only be reached if the cooling rate is sufficiently low within a temperature range at which the diffusion of the solute atoms is still adequately high. The precipitated volume fraction (f_p) and the dispersion of the particles of the second phase can thus be controlled via the cooling rate.

Procedure b) is frequently used for studies of decomposition kinetics under conditions which are easier to control and describe theoretically ($T = T_A = \text{const.}$; $D = \text{const.}$) than for case a). This leads to precipitate microstructure whose volume fraction and particle dispersion depend on $\Delta c(T)$ and the aging time t.

Decomposition reactions involve diffusion of the atomic species via the vacancy or/and the interstitial mechanism. Hence, the precipitate microstructure proceeding towards thermodynamic equilibrium evolves as a function of both time and temperature. In practice, a metallurgist is often requested to tailor an alloy with a specific precipitation microstructure. For this purpose it would be desirable to have a theoretical concept, e.g. available as a computer algorithm, which allows the derivation of suitable processing parameters for establishing the specific microstructure on grounds of the given thermodynamics of the alloy. This less empirical approach to alloy design, however, would require a comprehensive theory of precipitation kinetics, which at present has not yet been developed to a satisfactory level, despite recent efforts and progress made in elucidating the kinetics of first-order phase transitions in solids. Furthermore, in materials science it is frequently desirable to predict the kinetic evolution of an originally optimized precipitate microstructure under service conditions, e.g. for high temperature applications in two-phase materials, where the precipitate distribution might undergo changes because of coarsening. Even though the kinetics of coarsening are of great practical importance, a completely satisfactory coarsening theory has so far only been developed in the limit of zero precipitated volume fraction (see Sec. 4.6). This limit is, however, is never realized in technical alloys, where the volume fraction of the minor phase frequently exceeds 30%.

In the present chapter recent theoretical and experimental studies on the kinetics of phase separation in solids are reviewed from the point of view of the experimentalist. Special emphasis is placed on the questions to what extent the theoretical results can be verified experimentally and to what extent they might be of practical use to the physical metallurgist. We confine ourselves to dealing only with homogeneous and continuous phase separation mechanism. Heterogeneous nucleation at crystal defects, and discontinuous precipitation reactions at moving interfaces, as well as unmixing in solids under irradiation are treated separately in Chapter 5 of this volume.

VCH Verlagsgesellschaft, 6940 Weinheim
Autor: Umbruch:
Material Science & Technology, Vol. 5 Fahnen:
K. Tillisch, Würzburg

4.2 General Considerations

4.2.1 General Course of an Isothermal Precipitation Reaction

As illustrated for a Ni–37 at.% Cu–8 at.% Al alloy (Figs. 4-2 and 4-3), an isothermal precipitation reaction, the kinetics of which will be dealt with in more detail in Sections 4.5, 4.6, and 4.7, is qualitatively characterized by an early stage during which an increasing number density

$$N_v(t) = \int f(R)\,dR \qquad (4\text{-}2)$$

of more or less spherically shaped solute-rich clusters ('particles') with a size distribution $f(R(t))$ and a mean radius

$$\bar{R} = \frac{\int R f(R)\,dR}{\int f(R)\,dR} \qquad (4\text{-}3)$$

are formed. As is common to all homogeneous precipitation reactions studied so far, in the earliest stages of the reaction the parent phase α and the precipitate phase β share a common crystal lattice, i.e., the two phases are coherent. As inferred from the field ion micrograph of Fig. 4-2 and from the quantitative data of Fig. 4-3, during the early stages $\bar{R}$ increases somewhat and the supersaturation, Δc, decreases slowly. This small reduction in Δc, however, is sufficient to terminate the nucleation of new particles, as indicated by the maximum of $N_v(t)$.

Beyond this maximum the precipitate number density decreases (Fig. 4-3) due to the onset of the coarsening reaction, during which the smaller particles redissolve thus enabling the larger ones to grow (see Sec. 4.6). During this coarsening process the supersaturation Δc decreases asymptotically towards zero.

As mentioned previously, within the miscibility gap, the solid solution α becomes unstable and decomposes into the stable solid solution α' and the precipitated phase β:

$$\alpha \rightarrow \alpha' + \beta$$

The terminal solute concentration of the solvent (A)-rich matrix α' is given by the equilibrium solubility limit $c'_\beta(T)$; the terminal composition c_β of the precipitated phase is given by the solubility at T at the B-rich side of the phase diagram (Fig. 4-1). Frequently, the interfacial energy $\sigma_{\alpha\beta}$ (J m^{-2}) between the matrix and the equilibrium precipitate is rather large, in particular if

CH Verlagsgesellschaft, 6940 Weinheim
Umbruch:
Fahnen:
K. Triltsch, Würzburg
1. Korr.:
Material Science & Technology, Vol. 5
Herausgeber: Herr Schmitt

Sec. 4.7.5). In this case, the decomposition of α proceeds via the sequence

$$\alpha \rightarrow \alpha'' + \beta' \rightarrow \alpha' + \beta$$

During the first step of the precipitation sequence a metastable precipitate (transition phase β') is formed, frequently with large associated coherency strains and a small interfacial energy $\sigma_{\alpha\beta}$. Often the metastable phase β' is an intermetallic compound with a smaller solute concentration ($c'^{e}_{\beta} \equiv c'_\beta$) than the equilibrium precipitate (c_β). Because of the large coherency strains, the metastable ('coherent') solvus line (dashed line in Fig. 4-1) is shifted towards larger solute concentrations. This leads to a reduction of the supersaturation with respect to the (incoherent) equilibrium solvus line (Fig. 4-1), and, hence, to a reduction of the driving force for precipitation (see Sec. 4.2.4). Often only after extended aging do the metastable phases α'' and β' decompose further to the final equilibrium phases α' and β. The crystal structure of the equilibrium phase β finally precipitated is different to that of the parent phase, leading to either a coherent, a semi-coherent or a fully incoherent α'/β interface boundary (Gleiter, 1983). The atomic structure of the latter resembles that of a high-energy, high-angle grain boundary and, thus, is associated with a rather large interfacial energy and small elastic strain energies

The decomposition of Cu–Ti alloys with Ti contents between ≈ 1 at.% and 5 at.% serves as an example for such a complex precipitation sequence (Wagner et al., 1988):

α-Cu-(1 . . . 5 at.%) Ti

↓

1st step $T \approx 350$ °C

↓

α''-Cu-Ti (f.c.c. solid solution) +
β'-Cu_4Ti (metastable, coherent, body-centered-tetragonal structure, large coherency strains, small interfacial energy, $\sigma_{\alpha\beta} \approx 0.067$ J/m^2)

↓

2nd step extended aging at $T > 350$ °C

↓

α'-Cu–Ti (f.c.c. solid solution) +
β-Cu_4Ti (stable, hexagonal structure, incoherent, small strain, large

CH Verlagsgesellschaft, 6940 Weinheim
Umbruch:
Fahnen:
K. Triltsch, Würzburg
1. Korr.:
Material Science & Technology, Vol. 5
Herausgeber: Herr Schmitt

4.2.2 Thermodynamic Considerations – Metastability and Instability

Let us consider a binary alloy consisting of N_A solvent atoms A and N_B solute atoms B with $N_A + N_B = N$, or, in terms of atomic fractions, $c_A = N_A/N$ and $c_B = N_B/N$, with $c_A + c_B = 1$. (The concentrations of atoms A and B are then given as $c_A n_v$ and $c_B n_v$, where n_v is the number of atoms per unit volume.) As only one independent variable remains, we can refer to the composition of the alloy as $c \equiv c_B$ ($0 \leq c \leq 1$).

Decomposition of a supersaturated single-phase alloy into a two-phase state commonly occurs at constant temperature T and pressure p, and is thus prompted by a possible reduction of Gibbs free energy (Gaskell, 1983)

$$G = H - TS \tag{4-4}$$

with the enthalpy

$$H = U + pV \tag{4-5}$$

Thermodynamic equilibrium is attained when G has reached a minimum, i.e.,

$$\delta G_{T,p} = \mathrm{d}U + p\,\mathrm{d}V - T\,\mathrm{d}S = 0 \tag{4-6}$$

Usually for phase separation in solids the term $p\,\mathrm{d}V$ can be neglected with respect to the others in Eq. (4-6). Thus a good approximation for G is given by the Helmholtz free energy

$$F = U - TS \tag{4-7}$$

which will be used in the following sections as the relevant thermodynamic function. Equilibrium is achieved if F or the corresponding free energy density (F per unit volume or per mole) are minimized. Unmixing only takes place if the transition from the single-phase state lowers the free energy, i.e., by convention if $\Delta F < 0$.

H Verlagsgesellschaft, 6940 Weinheim
tor:
terial Science & Technology, Vol. 5
rsteller: Herr Schmitt
Umbruch:
Fahnen:
K. Triltsch, Würzburg
1. Korr.:

For a given temperature, volume, and solute concentration of a heterogeneous binary alloy, equilibrium between the two phases α and β can only be achieved if the concentrations of A and B in the two phases have been established such that

$$\left(\frac{\partial F^{\alpha}}{\partial n_i}\right)_{T,V,n_j} = \left(\frac{\partial F^{\beta}}{\partial n_i}\right)_{T,V,n_j} \tag{4-8}$$

In other words, at equilibrium the chemical potentials $\mu_i^{\alpha} = \dfrac{\partial F^{\alpha}}{\partial n_i}$ and $\mu_i^{\beta} = \dfrac{\partial F^{\beta}}{\partial n^i}$ of the component i (either A or B) in the two phases are identical and the two phases have a common tangent to the associated free energy curves. This fact is illustrated in Fig. 4-4 for a supersaturated solid solution of composition c_0, which decomposes into a B-depleted phase α' and a B-rich phase β of composition c_α^e and c_β^e, respectively. c_α^e and c_β^e are fixed by the common tangent to the free energy curves of the α- and β-phases; thus $c_\beta^e - c_\alpha^e$ represents the width of the miscibility gap at a given temperature (cf. Fig. 4-4).

Fig. 4-5 a shows schematically the phase diagram of a binary alloy with a two-phase region at lower temperatures for $T = T_1$; the associated free energy versus composition curve, $F(c)$, is shown in Fig. 4-5 b. In the single phase field α, F decreases first with increasing solute concentration due to the growing entropy of mixing (Eq. (4-7)). In the thermodynamically equilibrated two-phase region, F varies linearly with c (bold straight line satisfying the equilibrium condition $\mu_i^{\alpha} = \mu_i^{\beta}$).

VCH Verlagsgesellschaft, 6940 Weinheim
Autor
Material Science & Technology, Vol. 5
Hersteller: Herr Schmitt
Umbruch:
Fahnen:
K. Triltsch, Würzburg
1. Korr.:

The *mean field theories* (see Secs. 4.2.2 and 4.5) dealing with the unmixing kinetics of solid solutions quenched into the miscibility gap are now based on the (a priori questionable) assumption that the quenched-in single-phase states within the two-phase region can be described by a 'constraint' free energy $F'(c) > F(c)$, e.g. as is shown in Fig. 4-5b (bold dashed line). Based on this concept, the miscibility gap can be subdivided into a metastable region, where $F'(c) > F(c)$ and $\partial^2 F'/\partial c^2 > 0$, and an unstable region, for which $F'(c) > F(c)$ but $\partial^2 F'/\partial c^2 < 0$. The unique spinodal curve which is defined as the locus of the inflection points $(\partial^2 F'/\partial c^2)_T \equiv 0$ separates the two regions (Fig. 4-5a). The essence of the distinction between metastability and instability will be discussed in the following section.

4.2.3 Decomposition Mechanisms: Nucleation and Growth versus Spinodal Decomposition

Experimentalists are often inclined to distinguish between two different kinds of decomposition reactions, depending on whether i) the solid solution experiences a shallow quench (e.g. from points 0 to 1, Fig. 4-5a) into the metastable region or ii) whether it is quenched deeply into the unstable region of the miscibility gap (e.g. from points 0 to 2).

For *case i)*, unmixing is initiated via the formation of energetically stable solute-rich clusters ('nuclei'). As inferred from Fig. 4-5b, only thermal composition fluctuations with sufficiently large compositional amplitudes $\langle c - c_0 \rangle$ lower ($\Delta F < 0$) the free energy of the system and, hence, can lead to the formation of stable nuclei. According to the tangent construction for the given composition c_0 of the initial solid solution, the largest decrease in ΔF is obtained for a nucleus with composition c_p^{max} (which depends on c_0) rather than with $c_p = c_\beta^s$. The latter is the composition of the terminal second phase β coexisting in equilibrium with the α phase of composition c_α^s. The formation of stable nuclei via localized 'heterophase' thermal composition fluctuations (Fig. 4-6a) requires a nucleation barrier (typically larger than $5\,kT$) to be overcome (see Sec. 4.5.1) and is characterized by an incubation period. This defines the homogeneous solid solution at point 1 (Fig. 4-5a) as being metastable, and the

Verlagsgesellschaft, 6940 Weinheim
r.
rnal Science & Technology, Vol. 5
teiter: Herr Schmitt
Umbruch:
Fahnen:
K. Trittsch, Würzburg
1. Korr.:

As will be outlined in Section 4.5.1, the decay of a metastable solid solution via nucleation and growth has frequently been described in terms of cluster kinetics models. The cluster kinetics approaches are essentially based on the Becker-Döring theory (Becker and Döring, 1935) of the dynamics of solute cluster formation. There it is assumed that the non-equilibrium system consists of non-interacting solute-rich clusters of various size embedded into the matrix. The time evolution of the cluster size distribution and, hence, the dynamics of the decay of the metastable alloy, are assumed to proceed via the condensation or evaporation of single solute atoms by each cluster.

In *case ii)*, the non-equilibrium solid solution with an initial composition $c_0 > c_\beta^s$ (Fig. 4-5b) is unstable with respect to the formation of non-localized, spatially extended thermal composition fluctuations with small amplitudes. Hence, the unmixing reaction of an unstable solid solution, which is termed *spinodal decomposition*, is initiated via the spontaneous formation and subsequent growth of coherent ('homophase') composition fluctuations (Fig. 4-6b).

The dynamic behavior of an unstable alloy proceeding towards equilibrium has often been theoretically approached in terms of spinodal theories (see Sec. 4.5.2), amongst which the most well-known linear theory is due to Cahn (1966) and the most elaborate non-linear one is due to Langer, Bar-On, and Miller (1975). As discussed in Section 4.2.1, the spinodal theories are based on the assumption that in each stage of the decomposition reaction the free energy of the non-equilibrium solid solution, which contains compositional fluctuations, can be defined. As in the cluster kinetics models, the driving force for phase separation is again provided by lowering the free energy of the alloy. If the form of the 'constraint' free energy $F'(c)$ of the non-uniform system is properly chosen, the composition profile with associated minimum free energy can be determined (in principle!) at any instant of the phase transformation.

ellschaft, 6940 Weinheim
al Science & Technology, Vol. 5
ter: Herr Schmitt
Umbruch:
Fahnen:
K. Trittsch, Würzburg
1. Korr.:

The existence of a unique spinodal curve within the framework of the mean-field theories (Cahn, 1966; Cook, 1970; Skripov and Skripov, 1979) has led to the idea (still widespread in the community of metallurgists) that there is a discontinuity of the mechanism and, in particular, of the decomposition kinetics at the boundary between the metastable and unstable regions. Therefore, many experiments have been carried out in order to determine the spinodal curve and to search for a kinetic distinction between metastable and unstable states (see Sec. 4.5.4).

In reality, there is no necessity to develop dynamical concepts which are confined to either the metastable *nucleation and growth regime* (case i) or to the *unstable spinodal regime* (case ii). In fact, the cluster kinetic models and the spinodal theories can be seen as two different approaches used to describe phase separation, the dynamics of which are controlled by the same mechanism, i.e., diffusion of solvent and solute atoms driven by the gradient of the chemical potential (Martin, 1978).

This fact is reflected in the more recent attempts to develop *'unified theories'* which comprise spinodal decomposition as well as nucleation and growth. Langer et al. (1975) tried to develop such a theory on the basis of a non-linear spinodal theory (see Sec. 4.5.2), whereas Binder and coworkers (Binder et al., 1978; Mirold et al., 1977) chose the cluster kinetics approach by treating spinodal decomposition in the form of a generalized nucleation theory (see Sec. 4.5.1). These theories involve several assumptions whose validity is difficult to assess a priori. The quality of all spinodal or cluster kinetic concepts, however, can be scrutinized by Monte Carlo simulations of the unmixing kinetics of binary 'model' alloys. These are quenched into either a metastable or an unstable state (see Sec. 4.5.3) and can be described in terms of an Ising model (Kalos et al., 1978; Penrose et al., 1978).

Although both the 'unified theories' and the Monte Carlo simulations only provide qualitative insight into early stage unmixing behavior of a binary alloy, they have revealed that there is no discontinuity in the decomposition kinetics to be expected during crossing of the mean-field spinodal

VCH Verlagsgesellschaft, 6940 Weinheim
Autor:
Material Science & Technology, Vol. 5
Herstellter: Herr Schmitt
Umbruch:
Fahnen:
K. Trilitsch, Würzburg
1. Korr.:

curve by either increasing the concentration of the alloy and keeping the reaction temperature (T_r) constant or by lowering the reaction temperature and keeping the composition (c_0) constant. On the other hand, the mean-field description is strictly valid only for systems with infinitely long-range interaction forces (Gunton, 1984) and, hence, in general does not apply to metallic alloys (polymer mixtures might be close to the mean field limit: Binder, 1983, 1984; Izumitani and Hashimoto, 1985; see Sec. 4.5.4). Therefore, numerous experiments which have been designed by metallurgists in order to determine a unique spinodal curve simply by searching for drastic changes in the dynamic behavior of an alloy quenched into the vicinity of the mean-field spinodal must be considered with some reservations.

In principle, the above-mentioned theories and, in particular, the Monte Carlo simulations deal mainly with the dynamic evolution of a two-phase mixture in its early stages. They frequently do not account for a further evolution of the precipitate or cluster size distribution with aging time (i.e., coarsening; see Sec. 4.6) once the precipitated volume fraction is close to its equilibrium value. On the other hand, the time evolution of the precipitate microstructure beyond its initial clustering stages has been the subject of many experimental studies and is of major interest in practical metallurgy. For this purpose, numerical approaches have been devised (Langer and Schwartz, 1980; Kampmann and Wagner, 1984) which treat nucleation, growth, and coarsening as concomitant processes and, thus, allow the dynamic evolution of the two-phase microstructure to be computed during the entire course of a precipitation reaction (see Sec. 4.7).

VCH Verlagsgesellschaft, 6940 Weinheim
Autor:
Material Science & Technology, Vol. 5
Herstellter: Herr Schmitt
Umbruch:
Fahnen:
K. Trilitsch, Würzburg
1. Korr.:

As was pointed out in Section 4.2.1, the reaction path of a supersaturated solid solution can be rather complex, sometimes involving the formation of one or more intermediate non-equilibrium phases prior to reaching the equilibrium two-phase microstructure. Unlike in the 'early stage theories' mentioned above, these complications, which are of practical relevance, can be taken into consideration in numerical approaches. Even though they still contain a few shortcomings, numerical approaches lead to a practical description of the kinetic course of a precipitation reaction which lies closest to reality.

There exist quite a few recent comprehensive review articles and books dealing in a more general manner with the kinetics of first-order phase transitions (Gunton and Droz, 1984; Gunton et al., 1983; Binder, 1987; Gunton et al., 1983; Penrose and Lebowitz, 1979). Phase separation in solids (crystalline and amorphous alloys, polymer blends, oxides and oxide glasses) via homogeneous nucleation and growth or via spinodal decomposition represents only one aspect among many others (Gunton and Droz, 1984). Apart from the above-mentioned numerical approaches, the comprehensive articles by Martin (1978) and by de Fontaine (1982) cover most of the recent theoretical developments relevant to the kinetics of (homogeneous) phase separation in metallic systems. A general overview of the broad field of diffusive phase transformations in materials science, including heterogeneous nucleation and discontinuous precipitation not covered in the present chapter, can be found in the article by Doherty (1983) or, as an introduction to this field, in the book by Christian (1975).

4.2.4 Thermodynamic Driving Forces for Phase Separation

Even in the single-phase equilibrium state, the mobility of the solvent and solute atoms at elevated temperatures permits the formation of composition fluctuations which grow and decay again reversibly with time. If the solid solution is quenched into the miscibility gap the two-phase mixture is the more stable state and, thus, some of these fluctuations grow irreversibly

H Verlagsgesellschaft, 6940 Weinheim
tor:
terial Science & Technology, Vol. 5
rsteller: Herr Schmitt
Umbruch:
Fahnen:
K. Trillsch, Würzburg
1. Korr.:

energy. The reduction in free energy during the transformation from the initial to the final state provides the driving force ΔF. As we shall see in Section 4.5.1, it is possible to calculate the formation rate and the size of stable composition fluctuations ('nuclei' of the second phase) by means of the cluster kinetics approach once ΔF is known. It should, however, already be emphasized at this point that for most alloys it is rather difficult to calculate ΔF with sufficient accuracy. This is seen as one of the major hindrances to performing a quantitative comparison between theory and experiment.

The driving force for precipitation is composed of two different contributions:

i) the gain in chemical free energy, $\Delta F_{ch} < 0$, associated with the formation of a unit volume of the precipitating phase β, and

ii) the expenditure of distortion free energy, $\Delta F_{el} > 0$, accounting for the coherency strains which result from a likely variation of the lattice parameter with the spatial composition fluctuations.

i) Chemical contribution, ΔF_{ch}. According to the tangent rule and referring to Fig 4-4, the chemical driving force for precipitation of the equilibrium β phase out of a solid solution with composition c_0 is given by the numerical value of $\overline{xy}$. Assuming the precipitating phase β already has the final bulk composition $c_\beta^e \equiv c_p$ rather than c_p^{nuc} [which is only a reasonable assumption if the supersaturation is not too large (Cahn and Hilliard, 1959)], ΔF_{ch} has been derived for a unit volume of β phase with molar volume V_β as (Aaronson et al., 1970):

$$\Delta F_{ch} = -\frac{R_g T}{V_\beta} \cdot \left[c_\beta^e \ln \frac{a_B(c_0)}{a_B(c_\gamma^e)} + (1 - c_\beta^e) \ln \frac{a_A(c_0)}{a_A(c_\gamma^e)} \right] \tag{4-9}$$

where $a_i(c)$ is the activity of the solvent ($i = A$) or solute component ($i = B$) in the parent phase γ for the given composition.

For most alloy systems the activity data required for a composition of ΔF_{ch} by means of Eq. (4-9) are not available. In principle, they can be derived from a computation of the thermodynamic functions by means of the CALPHAD method. Originally this method was developed for the *calculation* of *phase diagrams* by Kaufman and coworkers (Kaufman and Bernstein, 1970) on the basis of a few accurately mea-

H Verlagsgesellschaft, 6940 Weinheim
ior
ater al Science & Technology, Vol. 5
rsteller: Herr Schmitt
Umbruch:
Fahnen:
K. Trillsch, Würzburg
1. Korr.:

sured thermodynamic data to which suitable expressions for the thermodynamic functions had been fitted. For the sake of a simplified mathematical description, the stable solid solutions of the particular alloy system are frequently described in terms of the regular solution model, whereas the phase fields of the intermetallic compounds are approximated by line compounds. The thermodynamic functions obtained thereby are then used to reconstruct the phase diagram (or part of it). The degree of self-consistency between the reconstructed and the experimentally determined phase diagram (or the agreement between the measured thermodynamic data and the derived data) serves as a measure of the accuracy of the thermodynamic functions. Hence, if, for example, $F(c, T)$ is known for the stable solid solution, this value can readily be extrapolated into the adjacent two-phase region to yield $F'(c)$ (see Fig. 4-5) of the supersaturated homogeneous solid solution or the related chemical potentials and activities. Of course, physically this is only meaningful if one assumes (as, in fact is done for the deviation of Eq. (4-9)) that the free energy of the non-equilibrium solid solution can be properly defined within the miscibility gap.

For many binary alloys and for some ternary alloys of technological significance, the thermodynamic functions have already been evaluated by means of the CALPHAD method and are compiled in volumes of the CALPHAD series (Kaufman, 1977).

Hitherto, due to the lack of available activity data, the activities entering Eq. (4-9) were frequently replaced by concentrations, i.e.,

$$\Delta F_{ch} = -\frac{R_s T}{V_\beta} \cdot \left\{ c_\beta^e \ln \frac{c_0}{c_\alpha^e} + (1 - c_\beta^e) \ln \left(\frac{1 - c_0}{1 - c_\alpha^e} \right) \right\} \tag{4-10}$$

If β is almost pure B, then $c_\beta^e \approx 1$ and the chemical driving force is approximated as

$$\Delta F_{ch} \approx -\frac{R_s T}{V_\beta} \ln \frac{c_0}{c_\alpha^e} \tag{4-11}$$

For many alloys the condition $c_\beta^e \approx 1$ is *not* met. Nevertheless, it has been used for computation of ΔF. As discussed by Aaronson et al. (1970), the resulting error can be rather large. If the nucleating phase is a solvent-rich intermetallic compound (e.g. Ni_3Al or Cu_4Ti), the computation of

VCH Verlagsgesellschaft, 6940 Weinheim
Autor:
Material Science & Technology, Vol. 5
Hersteller: Herr Schmitt
Umbruch:
Fahnen:
K. Triftsch, Würzburg
1. Korr.:

ΔF_{ch} is particularly difficult, since up to now the corresponding activities are neither known nor furnished by the CALPHAD method, and Eqs (4-10) and (4-11) are no longer valid.

ii) Reduction of the driving force by the elastic strain energy, ΔF_{el}. The formation of a composition fluctuation is associated with the expenditure of elastic strain free energy, ΔF_{el}, if the solvent and the solute atoms have different atomic radii. According to Cahn (1962), the free energy of a system containing homophase fluctuations is raised by

$$\Delta F_{el} = \eta^2 \, \Delta c^2 \, Y \tag{4-12}$$

$\eta = (1/a_0)(\partial a/\partial c)$ denotes the change in lattice parameter (a_0 for the homogeneous solid solution of composition c_0) with composition, and Δc the composition amplitude. Y is a combination of elastic constants and depends on the crystallographic direction of the composition modulation. It reduces to $E/(1-\nu)$, E and ν being Young's modulus and Poisson's ratio, respectively, if the elastic anisotropy $A \equiv 2c_{44} + c_{12} - c_{11}$ is zero; otherwise, in order to minimize ΔF_{el}, the composition fluctuations are expected to grow along the elastically soft directions, which for cubic crystals and $A > 0$ are the ⟨100⟩ directions.

In the context of heterophase fluctuations, the barrier against nucleation of the new phase is dominated by the matrix/nucleus interfacial energy (see Sec. 4.5.1). Since coherent interfaces have a lower energy than incoherent ones, a precipitate is usually coherent (or at least semi-coherent) during the early stages of nucleation and growth. Often its lattice parameter, a_β, is slightly different to that of the parent phase, a_α. The resulting misfit between the (unstrained) matrix and the (unstrained) precipitate:

$$\delta = 2 \frac{a_\alpha - a_\beta}{a_\alpha + a_\beta} \tag{4-13}$$

can be accommodated by an elastic strain if both δ and the particles are sufficiently small; this is commonly the case during the early stages of nucleation and growth.

VCH Verlagsgesellschaft, 6940 Weinheim
Autor:
Material Science & Technology, Vol. 5
Hersteller: Herr Schmitt
Umbruch:
Fahnen:
K. Triftsch, Würzburg
1. Korr.:

The problem of calculating ΔF_{el} for coherent inclusions is rather complex. It has been generally treated within the framework of isotropic elastic theory for ellipsoidal precipitates with varying axial ratios by Eshelby (1957), and has recently been extended to the anisotropic case (Lee and Johnson, 1982). Basically, these treatments yield the strain energy to depend on the particular shape of the new phase. Only if the transformation strains are purely dilatational and if α and β have about the same elastic constants does ΔF_{el} become independent of the shape. It is then given as (Eshelby, 1957):

$$\Delta F_{el} = 2\gamma \left(\frac{1+\nu}{1+\nu} \right) \delta^2 \qquad (4\text{-}14)$$

with γ being the shear modulus.

As is shown schematically in Fig. 4-7, with respect to the free energy of the *incoherent* equilibrium phase β, the free energy of the *coherent* phase β' is raised by the elastic energy to match the two lattices. The driving force $\Delta F^{inc} \equiv \overline{xy}$ is reduced to the value of $\Delta F^{coh} \equiv \overline{uv}$, and the solubility limit in the α phase increases from c_α^e to $c_\alpha'^e$.

Hence, if we refer to the resulting coherent phase diagram (cf. Fig. 4-1), the total driving force, ΔF, for coherent unmixing, implicitly already containing the elastic contribution, is obtained by replacing, e.g. in Eq. (4-11), the composition c_α^e of the incoherent phase by the composition $c_\alpha'^e$ of the coherent one:

$$\Delta F = -\frac{R_g T}{V_{\beta'}} \ln \frac{c_0}{c_\alpha'^e} \qquad (4\text{-}15)$$

As an example, for metastable iron-rich f.c.c. precipitates ($c_\beta^e \approx 99.9$ at.%) with $\delta = -8 \times 10^{-3}$ formed at 500 °C in a supersaturated Cu–1.15 at.% Fe alloy ($c_0 = 1.15$ at.%, $c_\alpha^e \approx 0.05$ at.%; Kampmann and Wagner, 1986), Eq. (4-12) yields $\Delta F_{el} \approx 0.13$ kJ/mol. This value is negligibly small with respect to the rather large chemical driving force (≈ 20 kJ/mol). Since, however, ΔF_{ch} decreases markedly with increasing temperature (or decreasing supersaturation), whereas ΔF_{el} does not, coherent nucleation commonly occurs at larger undercoolings or supersaturations, whereas nucleation of incoherent precipitates takes place at smaller ones. This is in fact observed in the Cu–Ti (see Sec. 4.2.1) and Al–Cu systems (Hornbogen, 1967).

As will be shown in Section 4.5.1.1, the barrier ΔF^* against formation of the new phase and, hence the nucleation rate, is not only a function of the driving force but is rather sensitive to the nucleus/matrix interface energy $\sigma_{\gamma\beta}$. Therefore, the phase nucleating first will not necessarily be the equilibrium phase with the lowest free energy but that with the lowest ΔF^*, e.g., a coherent metastable phase with a low value of $\sigma_{\gamma\beta}$. This explains the likely formation of a series of metastable phases (see Sec. 4.2.1) in various decomposing alloys, amongst which Al–Cu ($c_0 \leq 2.5$ at.% Cu) is probably the best known. There the stable phase (θ-$CuAl_2$) is incoherent, with a high associated $\sigma_{\gamma\beta}$ ($\gtrsim 1$ J/m^2) (Hornbogen, 1967). This inhibits homogeneous nucleation and θ is found to form only at small undercoolings, preferentially at grain boundaries (see Fig. 4-8). At larger undercoolings, a series of metastable copper-rich precipitates is formed in the order: GPI zones → GPII zones (θ'') → θ' with different crystal structures (see Fig. 4-8). Guinier-Preston zones of type I (GPI) and type II (GPII or θ'') are coherent and nucleate homogeneously, whereas θ' is semi-coherent and nucleates preferentially at dislocations.

4.3 Experimental Techniques for Studying Decomposition Kinetics

4.3.1 Microanalytical Tools

In general, the course of a decomposition reaction, including the early stages (during which composition fluctuations and second phase nuclei are formed, see Sec. 4.2.1) as well as the coarsening stages, cannot be followed continuously by any one microanalytical technique. The progress of the reaction is usually reconstructed from the microstructure that develops at various stages of the phase transformation. Thus it is necessary to analyze the spatial extension and the amplitude of composition fluctuations of incipient second-phase particles, as well as the morphology, number density, size and chemical composition of individual precipitates at various stages of the phase transformation. For this purpose microanalytical tools are required that are capable of resolving very small (typically a few nm) solute clusters, and which allow (frequently simultaneously) an analysis of their chemical composition to be made.

The tools which, in principle, meet these requirements can be subdivided into two groups: *direct imaging techniques* and *scattering techniques*.

It is beyond the scope of this chapter to discuss any one of the techniques belonging to either group in any detail. We shall only briefly summarize the merits and the shortcomings of the various techniques with respect to both the detection limit and the spatial resolution of microanalysis.

4.3.1.1 Direct Imaging Techniques

Field ion microscopy (FIM) (Wagner, 1982) as well as conventional (CTEM) (Hobbs et al., 1986) and high resolution (HREM) transmission electron microscopy (Smith, 1983) allow direct imaging of the second-phase particles, provided the contrast between precipitate and matrix is sufficient.

In CTEM both the bright field and the dark field contrast of particles less then ≈ 5 nm in diameter are often either too weak or too blurred for an accurate quantitative determination of the relevant structural precipitate parameters. Hence, CTEM does not provide access to an experimental investigation of the early stages of decomposition but remains a technique for studying the later stages. In contrast, HREM allows solute clusters of less than 1 nm diameter to be imaged, as was recently demonstrated for Ni_3Al precipitates in Ni–12 at.% and for silver-rich particles in Al–1 at.% Ag (Ernst and Haasen, 1988; Ernst et al., 1987). As is shown in Fig. 4-9 for the latter alloy, the particles are not ideally spherical but show some irregularities which, however, are small in comparison with their overall dimensions. Hence, describing their shapes by spheres of radius R is still a rather good approximation.

Prior to measuring the particle sizes directly from the HREM micrographs, it must be established via computer image simulations that there exists a one to one correspondence between the width of the precipitate contrast (dark area in Fig. 4-9) and its true size. This was verified for the HREM imaging conditions used in Fig. 4-9. The evolution of the size distribution in Al–1 at.% Ag with aging time at 413 K as derived from HREM micrographs is shown in Fig. 4-10.

VCH Verlagsgesellschaft, 6940 Weinheim
Autor:
Material Science & Technology, Vol. 5
Herstellerin: Herr Schmitt
Umbruch:
Fahnen:
K. Trillsch, Würzburg
1. Korr.:

The HREM lattice imaging technique has also been employed to determine the spacings of adjacent lattice planes in various alloys undergoing phase separation (Sinclair and Thomas, 1974; Gronsky et al., 1975). The smooth variations observed were attributed to variations in lattice parameter caused by composition modulations such as one would expect from spinodal decomposition (see e.g. Fig. 4-6b at t_1 or t_2). Subsequent model calculations of high-resolution images, however, yielded that the spatial modulation of the lattice fringes observed on the HREM image can be significantly different from the spatial modulation of the lattice plane spacings in the specimen (Cockayne and Gronsky, 1981). In practice, it does not appear possible to derive reliable information on composition modulations from modulations of lattice fringe spacings in HREM images.

The composition of the imaged particles can, in principle, be obtained from analytical electron microscopy (AEM), which is routinely based on energy dispersive X-ray analysis (EDX) or, less frequently, on electron energy loss spectroscopy (EELS) (Williams, 1984). Due to beam spreading by electron beam / specimen interaction, the spatial resolution for routine EDX microanalysis is limited to $\gtrsim 10$ nm. This value is rather large and confines EDX microanalysis of unmixing alloys to the later stages of precipitation. The more interesting early stages of decomposition, however, where composition changes of either extended or localized solute fluctuations are expected to occur, are not amenable to EDX microanalysis.

VCH Verlagsgesellschaft, 6940 Weinheim
Autor:
Material Science & Technology, Vol. 5
Umbruch:
Fahnen:
K. Trillsch, Würzburg

Theoretically, the spatial resolution of EFLS is expected to lie below 6 nm (Williams, 1984). In practice, however, this limit has not been approached, and up to now EFLS has not yet been employed for a systematic microanalysis of composition fluctuations during early stage decomposition.

Analytical field ion microscopy (AFIM) (Wagner, 1982) can favorably be applied for an analysis of ultrafine solute clusters in the early stages of decomposition, as both the imaging resolution of the FIM (see Fig. 4-2) and the spatial resolution of microanalysis of the integrated time-of-flight spectrometer ('atom probe') are sufficient, i.e., < 1 nm and ≈ 2 nm, respectively. (Although the atom probe detects single atoms from the probed volume, the requirement for the analysis to be statistically significant confines the microanalytical spatial resolution to ≥ 2 nm.) As is shown in Figs. 4-1 and 4-19, both the morphologies of small particles and their three-dimensional arrangements can also be determined in the FIM, at least for precipitates with sufficient contrast.

The volume sampled during an atom probe FIM analysis is rather small (typically $\approx 10^{-22}$ m^3). Hence, in order to obtain statistically significant data concerning the average size ($\bar{R}$) and the number density (N_v) of the precipitates, the latter ought to exceed $\approx 10^{23}$ m^{-3}. Since after the early stages of precipitation N_v decreases with time (see Sec. 4.2.1), AFIM shows its full potential as a microanalytical tool in studies of the early stages of precipitation, during which $\bar{R}$ is commonly small and N_v sufficiently large (Haasen and Wagner, 1985).

4.3.1.2 Scattering Techniques

The time evolution of the structure of supersaturated alloys, as well as of oxides and polymer blends undergoing phase separation can be analyzed by means of small angle scattering of *X*-rays (SAXS), *neutrons* (SANS), and light. Light scattering is of course confined to transparent specimens, in which the domain sizes of the evolving second phase must be in the order of > 1 μm. It has been successfully applied to studies of decomposition, e.g. a polymer mixture of polyvinyl methyl ether (PVME) and polystyrene (PS) (Snyder, 1983a, 1983b, 1985), and various glass-forming [illegible] (Goldstein, 1965; Binder, 1974;

Verlagsgesellschaft, 6940 Weinheim
or:
terial Science & Technology, Vol. 5
Sheila [illegible]

Umbruch:
Fahnen:
K. Trillsch, Würzburg
1. Korr.

In principle, SAXS (Guinier and Fournet, 1955; Glatter, 1982) and SANS (Kostorz, 1979) provide access to a structural analysis of unmixing alloys, in both the early stages where the composition fluctuations can be small in spatial extension and in amplitude, as well as in the later stages of decomposition where $\bar{R}$ and N_v may have attained values which are quite unfavorable for a quantitative analysis by TEM or FIM. In addition, evaluation of the Laue scattering allows the remaining supersaturation of solute atoms in the matrix to be determined.

The metallurgist is left with the problem of extracting in a quantitative manner all the structural data contained in scattering curves such as are shown in Fig. 4-11. This is often not trivial (Glatter, 1982), in particular for concentrated alloys (i.e., for most technical two-phase alloys). Here the scattering curve reveals a maximum (at position $\varkappa_m$ and with height $S_m(\varkappa_m)$ in Fig. 4-11) which results from an interparticle interference of the scattered waves (Kostorz, 1979). In general, the interparticle interference function is not known, thus impeding a straightforward quantitative analysis. Moreover, the composition and morphology of the fluctuations are required in order to perform such an analysis. For many alloys this information can only be obtained from AFIM or AEM. These complicating factors often demand the abovementioned microanalytical tools to be employed jointly, rendering experimental studies of decomposition rather difficult and tedious.

The SAS intensity is proportional to the structure function $S(\varkappa, t)$; $\varkappa$ is the scattering vector with $\varkappa \equiv |\varkappa| 4\pi \sin\left(\frac{\theta}{2}\right) / \lambda$; λ is the wavelength of the X-rays or neutrons and θ the scattering angle. For binary alloys $S(\varkappa, t)$ is the Fourier transform of the two-point correlation function at time t (Langer, 1975):

$$G(|\boldsymbol{r} - \boldsymbol{r}_0|, t) = \langle (c(\boldsymbol{r}, t) - c_0)(c(\boldsymbol{r}_0, t) - c_0) \rangle \tag{4-16}$$

The right-hand side in Eq. (4-16) denotes the nonequilibrium average of the product of the composition amplitudes at two different spatial positions, $\boldsymbol{r}$ and $\boldsymbol{r}_0$, in the alloy with average composition c_0.

$S(\varkappa, t)$ contains all the structural information on the phase separating system. Many theories and computer simulations dealing with phase separation yield the evolution of $S(\varkappa, t)$ and predict the shift of $\varkappa_m$ (which is a measure of the average spacing of solute clusters) and the growth of $S(\varkappa_m)$ with time (Langer et al., 1975;

Verlagsgesellschaft, 6940 Weinheim
or:
erial Science & Technology, Vol. 5
Sheila [illegible]

Umbruch
Fahnen:
K. Trillsch, Würzburg
1. Korr.

Hence, SAXS and SANS curves measured after different aging times can be directly compared with the predictions from various theoretical kinetic concepts (see Secs. 4.5.4 and 4.8.1).

In ternary systems the situation is much more complicated. There exist three linearly independent pair correlation functions with three related partial structure functions (de Fontaine, 1971, 1973), which linearly combine to the measured SAS intensity.

Thus, an unambiguous characterization of the kinetics of phase separation in *ternary* alloys requires the three partial structure functions to be determined separately. Only recently, this has been attempted by employing the 'anomalous small angle X-ray scattering' technique for an investigation of phase separation in Al–Zn–Ag (Hoyt et al., 1987), Cu–Ni–Fe (Lyon and Simon, 1987, 1988) and Fe–Cr–Co (Simon and Lyon, 1989).

Unlike for X-rays, for thermal neutrons the atomic nuclear scattering length is not monotonically dependent on the atomic number (Kostorz, 1979). For this reason use of SANS is more universal and is frequently superior to SAXS for decomposition studies of binary alloys with mainly transition metal constituents having similar atomic numbers. Consequently, SAXS has only been used extensively for studies of the unmixing kinetics in Al–Zn where the difference (this, in fact, controls the contrast in SAS) in atomic scattering lengths for X-rays is sufficiently large (Rundman and Hilliard, 1967; Hennion et al., 1982; Forouhi and de Fontaine, 1987).

Furthermore, if the two phases differ not only in composition but also in magnetization, both nuclear and magnetic SANS curves can be recorded (see Fig. 4-12). These two independently measurable SANS curves sometimes even allow the composition of the scattering centers to be determined, e.g. for Fe–Cu, where diamagnetic copper-rich particles precipitate in the ferromagnetic α-Fe matrix (Kampmann and Wagner, 1986), or for phase-separated amorphous $Fe_{40}Ni_{40}P_{20}$ (Gerling et al., 1988).

Due to relatively simple calibration procedures in SANS experiments, the scattered intensity which is expressed in terms of the coherent (nuclear or magnetic) scattering cross-section per unit volume, $d\Sigma(\varkappa,t)/d\Omega$, can be measured in absolute units. This is directly related to the structure function $S(\varkappa,t)$ via (Hennion et al., 1982):

$$\frac{d\Sigma}{d\Omega}(\varkappa,t) = \frac{1}{\bar{\Omega}^2}(\bar{b}_M - \bar{b}_p)^2 S(\varkappa,t) \qquad (4\text{-}17)$$

where $\bar{b}_M$ and $\bar{b}_p$ are the locally averaged (nuclear or magnetic) scattering lengths of the matrix and of the solute-rich clusters, respectively, and $\bar{\Omega}$ is the mean atomic volume.

VCH Verlagsgesellschaft, 6940 Weinheim
Autor:
Material Science & Technology, Vol. 5
Hersteller: Herr Schmitt
Umbruch:
Fahnen:
K. Trillsch, Würzburg
1. Korr.:

Material Science & Technology, Vol. 5, Materialwissenschaft, 1422 Mat. spalten PE4042 Mon Jul 3 08:19:56 1990

4.3.2 Experimental Problems

4.3.2.1 Influence of Quenching Rate on Kinetics

For studies on decomposition kinetics the alloy is commonly homogenized in the single-phase region at T_H (Fig. 4-1), quenched into brine and subsequently isothermally aged at T_A. In order to capture the initial stages of the decay of the supersaturated solid solution, both the quenching and the heating rate to T_A are required to be sufficiently high in order to avoid phase separation from occurring prior to isothermal aging. This can be comfortably achieved in alloys with small supersaturations. It is, however, often a problem (or even impossible) for alloys with large supersaturations and/or small interfacial energies, where the nucleation barriers are small (see Secs. 4.2.3 and 4.5.1) and, hence, the nucleation rates large.

The driving force for unmixing in Al–1 at.% Ag at 140 °C is rather small ($\approx$0.5 kJ/mol). Nevertheless, because of the extremely small interfacial energy of only $\approx$0.01 J m^{-2} (Le Goues et al., 1984d), the barrier to nucleation is so low that precipitation commences instantaneously almost as soon as the solvus line is crossed. Thus, except for extremely high quenching rates, the non-equilibrium single-phase state cannot be frozen in and the gas-quenched microstructure already contains a large number of small GP-zones (Fig. 4-13).

The accessible quenching rates have been found to be insufficient for a suppression of phase separation during quenching of homogenized Cu–Ti alloys with Ti concentrations exceeding $\approx$2.5 at.%. This is discernible from the SANS curve of the as-quenched specimen, see Fig. 4-11.

Further problems result from the fact that the decomposition kinetics at T_A are strongly influenced by the concentration of quenched-in excess vacancies. This depends strongly on the chosen homogenization temperature and quenching rate.

Fig. 4-14 shows SANS curves from specimens which were solution-treated at the given homogenization temperature T_H. Following quenching, each specimen was aged for 10 min at 350 °C. The maximum in the SANS curves is found to be the larger, and its position is found to be the smaller, the higher the homogenization temperature. This indicates that phase separation in the early stages progresses faster

VCH Verlagsgesellschaft, 6940 Weinheim
Autor:
Material Science & Technology, Vol. 5
Hersteller: Herr Schmitt
Umbruch:
Fahnen:
K. Trillsch, Würzburg
1. Korr.:

the higher the homogenization temperature is chosen. Obviously, in Cu–Ti the concentration of quenched-in excess vacancies is correlated to T_H and significantly influences the decomposition kinetics. This effect may be minimized if the alloy is first solution-treated at high T_H, and subsequently equilibrated at a homogenization temperature slightly above the solvus temperature prior to quenching.

The inconsistency concerning the exact mode and kinetics of decomposition in Al–22 at.% Zn, investigated by different authors (Rundman et al., 1967; Gerold and Merz, 1967), has been explained by the presence of different quenching rates which unavoidably lead to different states of solute clustering in the as-quenched specimens (Agarwal and Herman, 1973; Bartel and Rundman, 1975).

The problems stated above render particularly difficult those experiments which are devised for an examination of the various spinodal theories.

4.3.2.2 Distinction of the Mode of Decomposition

The criterion which must be satisfied in order to distinguish spinodal *d*ecomposition (s.d.) from a *n*ucleation and growth (n.g.) reaction is to prove by any microanalytical technique that the amplitude of the composition modulations of an alloy deeply quenched into the miscibility gap increases with time during the initial stages of phase separation (see Sec. 4.2.2 and Fig. 4-6). Even apart from the problem outlined in the preceding section, this is a rather difficult task, since the cluster diameters or the modulation wavelengths in most of the more concentrated alloys investigated hitherto have been found to range below the resolution limit of composition analysis, e.g. ≈ 2 nm for AFIM. Fig. 4-15 reveals that the compositions of the solute clusters in Ni–36 at.% Cu–9 at.% Al (Liu and Wagner, 1984) and in a hard magnetic Fe–29 at.% Cr–24 at.% Co (Zhu et al., 1986) alloy have reached their equilibrium values and, hence, remain constant once the clusters have attained sizes which are accessible to chemical analyses by AFIM (3 nm and 1.8 nm, respectively). (In fact both ternary alloys may be considered as being pseudobinary. Thus the thermodynamic considerations of Sec. 4.2.2 still apply.) The observed features suggest the reaction in both alloys to be of the n.g. type. However, it cannot be ruled out a priori that these clusters result from a s.d.

VCH Verlagsgesellschaft, 6940 Weinheim
Autor:
Material Science & Technology, Vol. 5
Herstellerin: Herr Schmitt
Umbruch:
Fahnen:
K. Trittsch, Würzburg
I. Korr.

action which was already terminated after even shorter aging times than could be covered in these studies.

Fig. 4-16 shows the interconnected precipitate microstructure of another hard magnetic alloy Fe–29 at.% Cr–14 at.% Co–2 at.% Al–0.15 at.% Zr, aged to yield its optimum magnetic properties. In order to characterize the decomposition process with respect to the distribution of Cr between the two phases, atom probe microanalysis was performed.

The measured Cr concentration of the strongly imaging precipitating α_2-phase as a function of aging time at $T = 525$ °C and $T = 600$ °C is shown in Fig. 4-17a. During aging at 600 °C for less than 5 min it increases continuously before it attains its constant equilibrium value. This behavior indicates unequivocally a spinodal decomposition mechanism. At the lower aging temperature of $T_A = 525$ °C, the Cr amplitude grows more slowly deeper within the miscibility gap due to the slower diffusion, but ultimately reaches higher equilibrium concentrations in the α_2-precipitates, thus showing the spinodal behavior even more clearly. The observed increase in Cr concentration in the α_2-phase with decreasing aging temperature is due to the widening of the miscibility gap. As the Cr concentration in the α_2-phase increases, the proportions of Co and Fe are reduced in this phase and are correspondingly increased in the α_1-phase. Atom probe analysis yields a Fe/Co ratio of 3 : 1 for both the α_1- and α_2-phases. This ratio corresponds to the tie-line in the ternary system along which spinodal decomposition proceeds. Fig. 4-17b shows the compositions of the iron-rich and chromium-rich phases for various aging times at 525 °C and the tie-line corresponding to an Fe/Co ratio of 3 : 1.

This study is one of the very rare ones on metallic alloys to have identified a decomposition reaction unequivocally to be of the spinodal type.

Frequently, the occurrence of either quasi-periodically aligned precipitates which give rise to side-bands in X-ray or TEM diffraction patterns (Fig. 4-18) or of a precipitated phase with a high degree of interconnectivity (e.g. Fig. 4-16) has been employed as a unique criterion by which to define an alloy as spinodal. However, as will be pointed out in the next section, morphology alone cannot be used to unambiguously distinguish spinodal decomposition from a nucleation and growth reaction (Cahn and Charles, 1965).

4.4 Precipitate Morphologies

4.4.1 Experimental Results

A large variety of different shapes in individual precipitates and of morphologies in precipitate microstructures exists. This is illustrated in Fig. 4-19 for three different Cu–Ni-based alloys with ternary additions of Al, Cr, or Fe, the precipitated volume fraction (f_p) of which is rather large, e.g. f_p (CuNiAl) ≈ 0.20, f_p (CuNiCr) ≈ 0.19, and f_p (CuNiFe) ≈ 0.1.

VCH Verlagsgesellschaft, 6940 Weinheim
Autor:
Material Science & Technology, Vol. 5
Herstellerin: Frau Schmitt
Umbruch:
Fahnen:
K. Trittsch, Würzburg
I. Korr.

Aging of Ni–37 at.% Cu–8 at.% Al for 167 h at 580 °C yields randomly distributed spherical particles with $\bar{R} \approx 11$ nm and a number density of $\approx 3.6 \times 10^{22}$ m^{-3} (Fig. 4-19). In contrast, TEM of Cu–36 at.% Ni–4 at.% Cr aged for 240 h at 650 °C reveals a modulated precipitate structure with cuboidal particles aligned along the three ⟨100⟩ directions (Fig. 4-19 b). Replacing Al or Cr by Fe leads to a mottled ('sponge-like') precipitate microstructure in Cu–48 at.% Ni–8 at.% Fe aged for 8 h at 500 °C. The three-dimensional interconnectivity of the mottled structure becomes discernible by a reconstruction of a sequence of FIM images which were taken at various distances underneath the original surface of the FIM specimen (Fig. 4-19 c).

Modulated structures have been predicted by Cahn (1965; Hilliard, 1970) to evolve from spinodal decomposition in elastically anisotropic cubic matrices, owing to the tendency to minimize the coherency strain energy (see Sec. 4.2.4, Eq. (4-12)). Furthermore, in material which is either isotropic or for which the elastic energy (see Eq. (4-12)) is negligibly small, spinodal decomposition is predicted to generate an interconnected mottled precipitate morphology. Computer simulations of the latter case, which were based on a superposition of randomly oriented sinusoidal composition fluctuations of fixed wavelength, random phase shifts and a Gaussian distribution of amplitudes, yielded an interconnectivity of the two conjugate phases for volume fractions ranging from ≈ 0.15 to ≈ 0.85 (Cahn, 1965). The simulated morphological pattern (Fig. 4-20) resembles the FIM images shown in Figs. 4-16 and 4-19 c remarkably well.

This has made it quite tempting to define these alloys and, more generally, all alloys displaying interconnected or quasi-periodical morphologies, as spinodal alloys. In general, however, in more concentrated alloys where the number density of clusters of the new phase is large and, hence, the intercluster spacing small, interconnectivity and quasi-periodicity in the late stage microstructure may result from other mechanisms. Examples of such mechanisms are coalescence of neighboring particles (e.g. in the $BaO-SiO_2$ system) or selective coarsening of elastically favorably oriented particles (e.g. in Ni–Al (Ardell

VCH Verlagsgesellschaft, 6940 Weinheim
Autor:
Material Science & Technology, Vol. 5
Hersteller: Herr Schmitt
Umbruch:
Fahnen:
K. Triltsch, Würzburg
1. Korr.:

and Nicholson, 1966; Doi et al., 1988). Hence, in essence, the distinction between a spinodal reaction and nucleation and growth *cannot* be based solely on any specific morphological features but requires a complete study of the evolution of the new phase with aging time.

4.4.2 Factors Controlling the Shapes and Morphologies of Precipitates

In the case of homogeneous nucleation, the precipitating particles are commonly coherent with the matrix. Their shape is controlled by the rather complex interplay of various factors, such as the magnitude and anisotropy of the interfacial energy, the difference in the elastic constants between matrix and precipitate, and the crystal structure of the latter (Khachaturyan, 1983).

The complexity of the situation is illustrated in Fig. 4-21 (Lee et al., 1977). There the anisotropic elastic strain energy $\Delta F_{el}/\delta^2$ of an ellipsoidal Ag-rich particle with different orientational relationships with respect to a Cu or Al matrix is plotted as a function of the aspect ratio $K \equiv T/R$, where T and R denote the two axes of an ellipsoid of revolution.

Assuming the interfacial energy to be isotropic, Fig. 4-21 reveals that the minimum strain energy is obtained for platelet-shaped particles ($K \ll 1$), the cubic directions of which lie parallel to those of the Al or Cu matrices.

More generally, theory predicts (Lee et al., 1977) platelets to have the minimum and spheres to have the maximum strain energy if the precipitated phase is elastically softer than the matrix, regardless of the orientation relationship and elastic anisotropy. For the reverse situation of a hard particle embedded into a softer matrix, the sphere represents the minimum strain energy shape.

However, often the elastic constants of the precipitating phase are not available, rendering the computation of the shape with minimum strain energy difficult. In particular, this holds true if the nucleating phase is a metastable transition phase.

In essence, however, the adopted shape is determined by the balance between the interfacial energy ΔF_{int} and the elastic energy ΔF_{el}. ΔF_{int} is minimized for particles with spherical or faceted shape (e.g., Figs. 4-9 and 4-19) whereas ΔF_{el}, which is related to the particle volume, commonly prefers a platelet-like morphology (e.g. Fig. 4-21). Thus, during the early stages of precipitation, ΔF_{int} is the dominating term, whereas ΔF_{el} prevails in the limit of large particles.

VCH Verlagsgesellschaft, 6940 Weinheim
Autor:
Material Science & Technology, Vol. 5
Hersteller: Herr Schmitt
Umbruch:
Fahnen:
K. Triltsch, Würzburg
1. Korr.:

This accounts for the frequently observed morphological sequence from spheres to plates or rotational ellipsoids with changing aspect ratios during coarsening of the precipitates.

In an internally nitrided Fe–3 at.% Mo alloy $(Fe,Mo)_{16}N_2$-type precipitates were already found to nucleate as thin platelets with $K \approx 0.1$ and with an undistorted $\{100\}_{\gamma+\varepsilon}$ plane common to both the α-matrix and the nitrides. The observed morphology as well as the $\{100\}_{\alpha\text{-Fe}}$ habit planes have been accurately predicted by applying macroscopic linear elastic theory to tetragonal $Fe_{16}N_2$ precipitates in ferritic iron, and assuming the interfacial energy to be isotropic (Khachaturyan, 1973). The latter assumption, however, is debatable, since during aging at 600 °C $(Fe,Mo)_{16}N_2$ platelets grow markedly only in diameter whereas their thickness remains almost constant (Fig. 4-22). This has been interpreted in terms of the large difference between the interfacial energy of the habit plane (≈ 0.05 J/m^2) and that of the peripheral plane (≈ 0.3 J/m^2) (Wagner and Brenner, 1978).

Under certain conditions, the elastic or magnetic interaction of precipitates with external stress fields or magnetic fields allows the generation of anisotropic, highly oriented precipitate microstructures which are sometimes of technological importance. If the transformation strain is non-spherical, such as for $Fe_{16}N_2$ in ferritic Fe–N, the particles may interact with an externally applied stress field. The resulting elastic interaction energy depends on the particular orientation of the particle with respect to this field. During aging, this causes a selective coarsening of favorably oriented particles at the expense of the energetically less favorably oriented ones. For instance, if the originally isotropically distributed $Fe_{16}N_2$ platelets undergo coarsening in the presence of an external tensile stress applied along [001], a highly oriented (anisotropic) precipitate structure will result (Ferguson and Jack, 1984, 1985), with the habit planes of all particles being parallel to each other and perpendicular to [001]. In addition, these platelets show a strong uniaxial magnetic anisotropy with the direction of easy magnetization parallel to the plate normal. This magnetic property can also be used for a complete orienting of the platelets during aging in an external magnetic field (Sauthoff and Pitsch, 1985).

4.5 Early Stage Decomposition Kinetics

As outlined in Sec. 4.2.3, the early stages of unmixing of a solid solution quenched into the miscibility gap are triggered by the growth and the decay of concentration fluctuations. Basically, the objective of any theory dealing with the kinetics of early stage decomposition is the prediction of the particular shape, amplitude, and spatial extension (or number of atoms) of a solute fluctuation which becomes critical and, hence, stable against decay. Once formed, the critical fluctuations render the supersaturated alloy unstable with respect to further unmixing.

According to Sec. 4.2.4 and referring to Fig. 4-6, *nucleation theories* consider the formation rate of stable nuclei, the latter representing spatially localized solute rich clusters ('particles' or 'droplets') with large concentration amplitudes. In this context, a distinction is made between *classical* (Sec. 4.5.1.1) and *non-classical* nucleation theory (Sec. 4.5.1.4) depending on how the free energy of the non-uniform solid solution containing the cluster distribution is evaluated. Once the free energy has been specified, the equilibrium distribution of heterophase fluctuations and the nucleation barrier (Sec. 4.2.3) can be calculated. The nucleation rate is then obtained as the transfer rate at which smaller clusters attain the critical size.

A 'composition wave' picture rather than a 'discrete droplet' formalism is employed in the spinodal theories (Sec. 4.5.4) which, as another approach, describe the early stage decomposition kinetics in terms of the time evolution of the amplitude and the wavelength of the certain stable 'homophase' fluctuations (Fig. 4-6b).

Quite a few recent articles exist dealing with the early stage unmixing kinetics. Russel (1980) and Aaronson and Russel (1982) consider both classical and non-classical nucleation phenomena from a more metallurgical point of view; recent progress made in the formulation of a microscopic cluster theory of nucleation is found in the article by Binder and Stauffer (1976). The comprehensive articles by Martin (1978) and by Gunton and Droz (1984) disclose recent developments of both nucleation and spinodal concepts not only to the theoretician but also to the materials scientist.

4.5.1 Cluster Kinetics Approach

4.5.1.1 Classical Nucleation - Sharp Interface Model

Suppose the homogenized solid solution is quenched not too deeply into the metastable regime of the miscibility gap (e.g. to point 1 in Fig. 4-5). There it is isothermally aged at a temperature sufficiently high for solute diffusion. After a certain time a distribution of *microclusters* containing i atoms (i-mers) will form in the matrix.

Generally, classical nucleation is now based on both a *static* and a *dynamic* part. In the static part the changes of free energy associated with the formation of an i-mer and the cluster distribution $f(i)$ must be evaluated. In the dynamic part the kinetics of the decay of the solid solution which now is described by the given distribution of non-interacting microclusters, are calculated in terms of the time evolution of $f(i)$; ultimately this will furnish the formation rate of stable clusters, i.e., the nucleation rate.

Classical nucleation theory treats the solute fluctuations as droplets which were cut from the equilibrium precipitate phase β and embedded into the α matrix; in this *capillarity* or *droplet model* the interface between α and β is assumed to be sharp, e.g. Fig. 4-6a. In essence, the approximation reduces the number of independent variables which characterize a cluster, and which may vary during the nucleation process (e.g. the solute concentration, the atomic distribution within the cluster, its shape, the composition profile across the interface, etc.) and, hence, determine the free energy of the system, to virtually a single one. That is the number i of atoms contained in the cluster or, in terms of a more macroscopic picture, the radius R of the droplet; $\frac{4\pi}{3} R^3 = i\,\Omega_\beta$ if Ω_β denotes the atomic volume in the droplet.

Once the small nucleus containing only a few atoms is treated as a droplet of the new phase β having bulk properties (which, in fact, is a rather debatable approximation), the interfacial free energy and the free energy are also considered to be entirely macroscopic in nature.

The formation of a coherent droplet with radius R which gives rise to some elastic coherency strains, leads to a change of free energy,

$$\Delta F(R) = (\Delta f_{ch} + \Delta f_{el}) \frac{4\pi}{3} R^3 + 4\pi R^2 \sigma_{\alpha\beta} \qquad (4\text{-}18)$$

VCH Verlagsgesellschaft, 6940 Weinheim
Autor:
Material Science & Technology, Vol 5
Hersteller: Herr Schmitt
Umbruch:
Fahnen:
K. Trillsch, Würzburg
1. Korr.:

where, according to Sec. 4.2.4, $(\Delta f_{ch} + \Delta f_{el})$ is the driving force per unit volume and $\sigma_{\alpha\beta}$ the specific interfacial energy.

The first term in Eq. (4-18) which scales with R^3 accounts for the gain of free energy on forming the droplet (i.e., it is negative). The second term which scales with R^2 has to be expanded on forming the interphase boundary and, hence, is a positive contribution to $\Delta F(R)$.

Fig. 4-23 shows the dependence of the two contributions in Eq. (4-18) on the droplet radius. The resulting droplet formation energy $\Delta F(R)$ passes through a maximum at $R \equiv R^*$ or $i \equiv i^*$ with

$$R^* = \frac{2\sigma_{\alpha\beta}}{-(\Delta f_{chem} + \Delta f_{el})} \quad \text{or}$$

$$i^* = \frac{4\pi}{3\Omega_\beta} \left[\frac{2\sigma_{\alpha\beta}}{-(\Delta f_{chem} + \Delta f_{el})} \right]^3 \qquad (4\text{-}19)$$

Accordingly, clusters with $R = R^*$ are in unstable equilibrium with the solid solution, i.e., the free energy of the system is lower if it contains clusters with sizes below or beyond R^* or i^*. Therefore, only clusters with radii which exceed the radius R^* of the *critical nucleus* are predicted to grow continuously. This requires a fluctuation to become a critical nucleus, first to overcome the activation barrier for nucleation, or the nucleation energy,

$$\Delta F(R^*) \equiv \Delta F^* = \frac{16\pi}{3} \frac{\sigma_{\alpha\beta}^3}{(\Delta f_{chem} + \Delta f_{el})^2} \qquad (4\text{-}20)$$

As outlined in Sec. 4.2.4, Δf_{chem} decreases strongly with decreasing supersaturation, or, for a given concentration, with increasing aging temperature (Fig. 4-1). Correspondingly, since $\sigma_{\alpha\beta}$ and Δf_{el} are only weakly dependent on temperature, both R^* and ΔF^* increase strongly with decreasing supersaturation. Hence, the droplet model ought to approximate the energetics of an unmixing alloy better the smaller the supersaturation.

VCH Verlagsgesellschaft, 6940 Weinheim
Autor:
Material Science & Technology, Vol. 5
Hersteller: Herr Schmitt
Umbruch:
Fahnen:
K. Trillsch, Würzburg
1. Korr.:

Once we have specified the free energy of formation of a droplet in terms of its size R or i (Eq. (4-18)), the free energy of the system containing a number $f(i,t)$ of non-interacting clusters of size i per unit volume at time t is given as (Frenkel, 1939; Russell, 1980):

$$F = \sum_{i}^{n} \Delta F(i) \cdot f(i,t) - T \cdot S_{mix} \qquad (4\text{-}22)$$

The entropy of mixing S_{mix} arises from distributing the clusters on the available N_0 lattice sites per unit volume of the crystal.

The kinetics of early stage unmixing are governed by the change of the cluster size distribution function $f(i,t)$ with aging time. Microscopically, this may occur via different processes.

Volmer and Weber (1926), Becker and Döring (1935) and Zeldovich (1943), the works which most nucleation theories are based on, assume the transitions between size classes in an assembly of non-interacting droplets to occur via the condensation or evaporation of *single* solute atoms. Hence, since only a transition between size classes i and $i+1$ is allowed, its flux J_i is given as (Russell, 1980):

$$J_i = \beta(i)\, f(i,t) - z(i+1)\, f(i+1,t) \qquad (4\text{-}23)$$

$\beta(i)$ is the condensation rate and $z(i+1)$ the evaporation rate of a single atom to a cluster of size i or from a cluster of size $(i+1)$, respectively.

In equilibrium, the fluxes J_i must vanish and $f(i,t)$ becomes identical with the equilibrium cluster size distribution $C(i)$ for which F in Eq. (4-22) attains a minimum:

$$C(i) = N_0 \cdot e^{-\Delta F(i)/kT} \qquad (4\text{-}24)$$

It is worth noting that in this case the number of critical nuclei $C^* \equiv C(i=i^*)$ is proportional to $\exp\{-\Delta F^*/kT\}$. Then, according to Eq. (4-23), the condensation rate and evaporation rate are related to each other via

$$z(i+1) = \frac{\beta(i)}{C(i+1)}\, C(i) \qquad (4\text{-}25)$$

In the conventional nucleation theory it is now assumed that the evaporation rate $z(i+1)$ derived for the equilibrium situation ('principle of detailed balance') is still valid for the non-equilibrated system where $f(i,t) \neq C(i)$ and $J_i \neq 0$. Under such an assumption, which becomes reasonable when i-mers are able to relax internally between atomic condensation or evaporation, the flux of clusters between size classes i and $i+1$ is obtained from Eqs. (4-23) and (4-25) (Russell, 1980):

$$J_i = \beta(i)\, C(i) \left[\frac{f(i+1,t)}{C(i+1)} - \frac{f(i,t)}{C(i)} \right]$$
$$\approx -\beta(i)\, C(i) \left[\frac{\partial f(i,t)/C(i)}{\partial i} \right] \qquad (4\text{-}26)$$

In the earliest theory on nucleation (Volmer and Weber; V-W, 1926) it is assumed that $f(i,t) = 0$ for clusters with $i > i^*$ (or $R > R^*$), and that clusters with $R > R^*$ decay artificially into monomers, thus keeping the matrix supersaturation about constant. The resulting quasi-steady state distribution of cluster sizes is obtained from Eq. (4-24) and shown in Fig. 4-24. In this theory the *steady state nucleation* rate $J^*_{V\text{-}W}$ is obtained as the product between the number C^* of critical nuclei and the rate β at which a single solute atom impinges on the critical nucleus rendering it supercritical, i.e.:

$$J^*_{V\text{-}W} = \beta C^* = \beta N_0 \exp\{-\Delta F^*/kT\} \qquad (4\text{-}27)$$

One of the shortcomings of the V-W theory is that supercritical droplets with $i > i^*$ are assumed *not* to belong to the cluster size distribution. This was cleared up by the theory of Becker and Döring (1935). In their theory (B-D) the non-equilibrium *steady state* distribution of small clusters with $i \ll i^*$ is identical with that of V-W but unlike in the latter theory, clusters with $i^* \leqq i \leqq i_c$ (i_c is a somewhat arbitrarily chosen cut-off size) are considered to belong to the size distribution (Fig. 4-24).

Hence, according to Eq. (4-23) a decay or dissolution of supercritical droplets with $i > i^*$ becomes a likely process in the B-D theory and is accounted for by the *Zeldovich factor* Z. With the assumption that the rate $\beta \ldots \beta^*$ at which a solute atom impinges at a *critical* droplet is proportional to

its surface area, integration of the cluster flux equation (Eq. (4-26)) yields the *steady state nucleation rate* $J^{S}_{B,D}$ of the Becker-Döring theory as (Russell, 1980):

$$J^{S}_{B,D} = Z\beta^* N_0 \exp\{-\Delta F^*/kT\} \qquad (4\text{-}28)$$

with

$$Z = \left[\frac{-1}{2\pi kT}\left.\frac{\partial^2 \Delta F}{\partial i^2}\right|_{i=i^*}\right]^{1/2} \qquad (4\text{-}29)$$

According to Eq. (4-28), nucleation is a thermally activated process with the activation energy being identical to that (ΔF^*) of forming a critical nucleus of size i^* or R^*. Furthermore, like the thermodynamic model which yields the number of critical nuclei to be proportional to $\exp\{-\Delta F^*/kT\}$ (Eq. (4-24)), the kinetic treatment predicts the steady state nucleation rate also to be proportional to the same exponential factor.

The Zeldovich factor Z is in the order of 1/20 to 1/40; graphically, its reciprocal value corresponds approximately to the width of the potential barrier, $\Delta F(R)$ or $\Delta F(i)$, at a distance kT below the maximum (Fig. 4-23).

4.5.1.2 Time-Dependent Nucleation Rate

It must be pointed out that the above given steady state nucleation theories do not provide any information on the momentary cluster size distribution nor on the nucleation rate prior to reaching steady state conditions, i.e., the time-dependent nucleation rate $J^*(t)$. Commonly the latter is considered in terms of the steady-state nucleation rate J^s and an *incubation period* τ via:

$$J^*(t) = J^s \exp\{-\tau/t\} \qquad (4\text{-}30)$$

Steady state will be achieved once the clusters have attained sizes for which the probability of redissolution is negligibly small. Referring to Fig. 4-23 and recalling the physical meaning of the Zeldovich factor Z, this will be the case for clusters with $i > i^* + 1/2Z$ (Feder et al., 1966). As the gradient of $\Delta F(i)$ within the region $1/Z$ is rather small, the clusters will move across this region predominantly by random walk with the jump frequency β^*. The time

$$\tau = \frac{1}{2\beta^* Z} \qquad (4\text{-}31)$$

to cover the distance $1/Z$ by random walk is identified with the incubation period.

VCH Verlagsgesellschaft, 6940 Weinheim
Autor:
Material Science & Technology, Vol. 5
Hersteller: Herr Schmitt
Umbruch:
Fahnen:
K. Tiltsch, Würzburg
1. Korr.:

So far it has been assumed that during nucleation the supersaturation and, hence, the driving force remains unchanged. At its best this may be valid for extremely low nucleation rates: in this case ΔF^*, Z and τ may be considered as time independent quantities. Russell (1980) proposed the nucleation process to terminate itself under steady state conditions if the incubation time τ is shorter than some critical time t_c. If, however, $\tau > t_c$, phase separation will be completed without steady state ever having been achieved. This situation which, in fact, is met in most decomposing alloys studied hitherto (see Sec. 4.7.4.1), is referred to as *catastrophic nucleation;* under such conditions ΔF^*, Z and τ become time dependent. Assuming that nucleation ceases once the diffusion fields around precipitates with radius R and composition c^e_β embedded into a matrix with initial composition c_0 begin to overlap (Fig. 4-6a), and furthermore that nucleation becomes unlikely within a region $\frac{1}{2}R$ ($\varepsilon \approx 1/10$) around the particle where the solute content has decreased below $(1-\varepsilon)c_0$, the critical time t_c is estimated to be:

$$t_c = \left[\varepsilon^6 \Big/ \left(\frac{c^e_\beta}{c_0}\right)^3 \frac{1}{(2D)^3} \frac{1}{J^6}\right]^{1/5} \qquad (4\text{-}32)$$

where D is the solute diffusion coefficient.

For a quantitative assessment of classical nucleation theory, the atomic impingement rate β^* in Eq. (4-28) must be known. For spherical nuclei it was evaluated to be (Russell, 1970):

$$\beta^* = \frac{4\pi R^{*2} D c_0}{a^4} \qquad (4\text{-}33)$$

where a is the lattice parameter. β^* is proportional to the nucleus surface as has already been assumed in the original Becker-Döring theory.

According to Sec. 4.4.2 the nucleus shape with minimum energy may deviate from the spherical one due to different energies of the interfaces (some may be coherent, some semi- or incoherent, Sec. 4.2.1) bounding the nucleus in different crystallographic directions. It has been shown

VCH Verlagsgesellschaft, 6940 Weinheim
Autor:
Material Science & Technology, Vol. 5
Hersteller: Herr Schmitt
Umbruch:
Fahnen:
K. Tiltsch, Würzburg
1. Korr.:

(Chan et al., 1978) that in this case the expressions for ΔF^*, Z, β^* and τ given above for spherical clusters, have merely to be multiplied with numerical factors but otherwise remain unchanged. The magnitude of these numerical factors depends on the perpendicular equilibrium shape of the nucleus. Ignoring volume strain energy, the nucleus equilibrium shape can be determined by means of the Wulff construction on a three dimensional $\sigma_{x\theta}$-plot (Herring, 1953). The latter is obtained from a radial plot of different vectors in every direction (e.g. v_1, v_2, v_3 in Fig. 4-25), the length of which is proportional to the energy of the interface perpendicular to the particular vector. The surface connecting the tips of all vectors represents the polar $\sigma_{x\theta}$-plot, wherein the cups indicate interfaces with good atomic matching, i.e., low interfacial energies. Subsequently planes are drawn (the so-called *Wulff planes*) perpendicular to the vectors v_1, v_2, v_3, etc. which intersect the $\sigma_{x\theta}$-plot (Fig. 4-25). The inner envelope of the Wulff planes yields the equilibrium shape of the nucleus with facets at the cusps of the $\sigma_{x\theta}$-plot (Martin and Doherty, 1976).

LeGoues et al. (1982) employed a nearest neighbour interaction, regular solution model for a computation of the $\sigma_{x\theta}$-plot as a function of T/T_c (T_c is the critical temperature) within the miscibility gap of an f.c.c. solid solution. At low temperatures they found the nucleus shape to be fully faceted by (100) and (111) planes whereas at 0.5 T_c and near-zero supersaturation, the nucleus shape can be rather well approximated by a sphere. They furthermore showed that beyond $T \approx 0.4\,T_c$ the parameters ΔG^*, Z, τ, and β^* which enter the time-dependent (classical) nucleation rate (Eqs. (4-28) and (4-30)) must no longer be corrected in order to account for deviations from spherical shape.

4.5.1.3 Experimental Assessment of Classical Nucleation Theory

A quantitative assessment of classical nucleation theory in solids is inherently difficult and, thus, has prompted only a few studies. First of all, the range of supercooling (or supersaturation) has to be chosen such that nucleation is homogeneous and the nucleation rates are neither unmeasurably slow nor beyond the limits of catastrophic nucleation. Secondly, the quenching rate must be sufficiently high in order to avoid phase separation during the quench but also sufficiently low in order to avoid excess vacancies to be quenched in.

Servi and Turnbull (1966) studied in a well-designed experiment homogeneous nucleation kinetics of coherent Co-rich precipitates in Cu - 1 ... 2.7 wt.% Co alloys. By using electrical resistivity measurements, they could determine rather accurately the precipitated volume fraction. Assuming that the growth is diffusion-controlled (Sec. 4.5.2), from the latter the particle density at the end of the precipitation process could be derived as a function of aging temperature and composition. The thus indirectly obtained number density of Co-rich particles which was later on corroborated by CTEM studies, agreed within one order of magnitude with the one predicted by classical nucleation theory if the interfacial energy was taken as $\approx 0.19\ J/m^2$; this value was derived from more recent discrete lattice calculations (Shiflet et al., 1981).

The validity of classical nucleation theory as evidently proven by the Servi-Turnbull study on Cu–Co alloys, was recently challenged by LeGoues and Aaronson (1984d). They argued that the supersaturation employed in the Servi-Turnbull investigations were probably too high for avoiding phase separation during quenching and also likely too high for avoiding concomitant coarsening during the precipitation reaction. Employing a discrete lattice point model, which incorporates coherency strain energy, LeGoues and Aaronson first evaluated the *'window'* of temperatures ($\Delta T \approx 50$ °C) and compositions (0.5 to 1.0 at.% Co) at which homogeneous nucleation kinetics would be neither too sluggish nor too fast, and at which no interference with coarsening would be expected. Prior to CTEM analyses, the isothermally nucleated particles had to be subjected to

diffusion-controlled growth in order to increase their radius beyond a certain size ($R \approx 5$ nm) at which the Co-rich particle became easily discernible in the CTEM. The experimental results were interpreted in terms of classical nucleation theory (Eq. (4-30)). The agreement between the experimentally obtained nucleation rates and the theoretically predicted ones was again found to be rather good, thus providing further support for the validity of classical nucleation theory. Furthermore, as is shown in Fig. 4-27, for smaller supersaturations the nucleation energies ΔF^* and the critical radii R^* as evaluated from classical nucleation theory are almost identical with the corresponding quantities calculated from either the non-classical nucleation theory (cf. Sec. 4.5.1.4, Eq. (4-38)) or a discrete lattice point theory. Hence, at least for smaller supersaturation, the classical theory predicts the nucleation rates about as well as the two more sophisticated theories.

In another attempt to assess classical nucleation theory, Kirkwood and coworkers (Kirkwood, 1970; West and Kirkwood, 1976; Hirata and Kirkwood, 1977) studied early stage precipitation of γ'-Ni_3Al in Ni–Al alloys using also CTEM. They found the γ'-Ni_3Al precipitate number density to decrease instantaneously upon aging which is indicative of an extremely fast nucleation process and the observation of a coarsening process rather than a nucleation event. By making certain assumptions they attempted to infer the steady state nucleation rate from the particle density observed during coarsening. The observed lack of agreement between the experimentally derived nucleation rates and the theoretically predicted ones may be seen to result from these experimental difficulties.

4.5.1.4 Non-Classical Nucleation – Diffuse Interface Model

In the droplet model classical nucleation is based on; it is assumed that the composition of the nucleus is more or less constant throughout its volume and that its interface is sharp. This made it possible to take the change of volume free energy and the interfacial free energy separately into account (Eq. (4-18)). In *non-classical nucleation theory* developed by Cahn and Hilliard (1959) the inhomogeneous solid solution in its metastable state is considered to contain homophase fluctuations with *diffuse interfaces* and a composition which varies with position throughout the cluster (Fig. 4-6 b). Hence, unlike in the droplet model a critical fluctuation has now to be characterized by at least two parameters, its spatial extension or wavelength λ and its spatial composition variation. The necessary free energy formalism which treats volume free energy and surface free energy no longer separately has been elaborated by Cahn and Hilliard (1958). They wrote the free energy change associated with the transfer from the homogeneous system with composition c_0,

$$F_0 = \int_V f(c_0)\,dV \qquad (4\text{-}34\,a)$$

to that of the inhomogeneous system with

$$F = \int_V \{f(c) + K^*(\nabla c)^2\}\,dV \qquad (4\text{-}34\,b)$$

as:

$$\Delta F = (F - F_0) = \int_V \{[f(c) - f(c_0)] + K^*(\nabla c)^2\}\,dV \qquad (4\text{-}34\,c)$$

The basic idea behind these expressions is to subdivide the solid with volume V into many small volume elements dV, a procedure which is often referred to as *'coarse graining'* (Langer, 1971). The free energy of each volume element is taken as $f(c)\,dV$. $f(c)$ is considered to be the free energy per unit volume of the bulk material with composition c which is equal to the mean composition $c(r)$ with dV located at position r. In essence, coarse graining requires the number of atoms within each volume element to be sufficiently large such that $c(r)$, as well as $f(c)$, can be specified as continuous functions. On the other hand, the number of atoms within dV must be small enough in order to avoid phase separation within the individual volume element. For the non-uniform system with composition fluctuations, Cahn and Hilliard (1958, 1959) assumed that the local free energy contains further terms depending on the composition gradient (∇c). They finally showed that the non-uniform environment of atoms in a composition gradient, may be accounted for by adding to the local free

VCH Verlagsgesellschaft, 6940 Weinheim
Autor:
Material Science & Technology, Vol. 5
Hersteller: Herr Schmitt
Umbruch:
Fahnen:
K. Trillsch, Würzburg
1. Korr.:

VCH Verlagsgesellschaft, 6940 Weinheim
Autor:
Material Science & Technology, Vol. 5
Hersteller: Herr Schmitt
Umbruch:
Fahnen:
K. Trillsch, Würzburg
1. Korr.:

energy a single *gradient energy* term which is proportional to $(\nabla c)^2$. Hence, the resulting free energy of a volume element dV is expressed as $f(c) + K^*(\nabla c)^2$ where the constant K^* denotes the gradient energy coefficient. Summing up all contributions from the various volume elements yields Eq. (4-34c).

The continuum model is based on the assumption that the free energy $f(c)$ varies smoothly with composition, i.e., the wavelength of the fluctuations must be large compared with the interatomic spacing. Furthermore, as a continuum model it is required that the two evolving phases are fully coherent with each other and thus have the same crystal structure with similar lattice parameters. If the lattice parameter changes with composition, which is commonly the case in crystalline solids, the requirement for coherency leads to coherency strains which according to Eq. (4-12) are accounted for by an elastic free energy term

$$f_{el}(c) = \eta^2 Y(c - c_0)^2 \tag{4-35}$$

Combining Eqs. (4-35) and (4-34c) yields:

$$\Delta F = \int_V [f(c) - f(c_0) + K^*(\nabla c)^2 + \eta^2 Y(c - c_0)^2]\, dV \tag{4-36}$$

This expression may be interpreted in similar terms as for classical nucleation (Eq. (4-18)): neglecting the elastic free energy terms, the positive contribution of the gradient free energy as a barrier to nucleation acts like the surface free energy in the droplet model and is finally overcome by the gain in chemical free energy once the composition difference between the fluctuation and the homogeneous matrix has become sufficiently large.

VCH Verlagsgesellschaft, 6940 Weinheim
Autor
Material Science & Technology, Vol 5
Herausgeber Herr Schmitt
Umbruch:
Fannen.
K. Tittisch, Würzburg
1. Korr

Assuming isotropy, the composition profile $c(r)$ of a spherical fluctuation (r is the radial distance from the fluctuation center) is obtained from a numerical integration of (Cahn and Hilliard, 1959):

$$2K^* \frac{d^2c}{dr^2} + 4\frac{K^*}{r}\frac{dc}{dr} = \left.\frac{\partial f}{\partial c}\right|_c - \left.\frac{\partial f}{\partial c}\right|_{c_0} \tag{4-37}$$

with the boundary conditions $\frac{dc}{dr} = 0$ at the nucleus center ($r \approx 0$) and far away from it ($r \to \infty$) where $c \equiv c_0$. The critical nucleus is then determined as that fluctuation which, like a critical droplet, is in unstable equilibrium (Eq. (4-36)) with the matrix. Its composition is established such that the nucleation barrier (e.g. de Fontaine, 1982),

$$\Delta F[c^*(r)] \equiv \Delta F^* = 4\pi \int_0^r \left[\Delta f(c^*) + K^*\left(\frac{dc}{dr}\right)^2\right] r^2\, dr \tag{4-38}$$

attains a minimum. Like in classical nucleation, Δf^* is the vertical distance from the tangent at c_0 to the free energy curve at c^* (cf. Fig. 4-5b). Suppose ΔF^* is known; the nucleation rate is then obtained from Eq. (4-28) or (4-30). Provided the constraint free energy $f(c)$ is known, the composition profile of a critical nucleus in a solid solution with composition c_0 and gradient energy coefficient K^* (K^* is of the order $10 - 100\ J/m \cdot \frac{1}{V}$ (at. fract.)$^{-2}$) can be obtained from integrating Eq. (4-37). Fig. 4-26 shows the composition profiles of nuclei in supersaturated solid solutions with different solute concentrations c_0 quenched to $T/T_c = 0.25$, where T_c is the critical temperature (LeGoues et al., 1984b); these calculations are based on the regular solution model for $f(c)$ (cf. Sec. 4.2.4). For *small supersaturation* ($c_0 = 2 \cdot 10^{-3}$) the composition within the nucleus is constant and corresponds to c_β^e of the equilibrium β phase. The interface is almost sharp similar to that assumed in the classical droplet model. Correspondingly, the free energy of formation of the nucleus (ΔF^*) and its size (R^*) as evaluated from either classical or non-classical theory are almost identical (Fig. 4-27) and tend to infinity as c_0 approaches c_β^e. With increasing supersaturation the composition profile becomes increasingly diffuse and the solute concentration at the nucleus center decreases (Fig.

VCH Verlagsgesellschaft, 6940 Weinheim
Autor
Material Science & Technology, Vol 5
Umbruch:
Fannen.
K. Tittisch, Würzburg
1. Korr

4-26); this situation is no longer accounted for by the droplet model. Furthermore, as the initial composition (c_0) approaches the spinodal one (c_0^s), unlike the droplet model, non-classical theory predicts ΔF^* to go to zero (Fig. 4-27a), and the spatial extent of the critical fluctuations (or R^*) to increase again: at $c_0 \equiv c_0^s$, R^* finally becomes infinite (Fig. 4-27b) suggesting a discontinuity of the decomposition mechanism exists at the spinodal line (cf. Sec. 4.2.3).

This *apparent discontinuity* at the spinodal results from the assumption that the decomposition path is controlled by the minimum height of the nucleation barrier, i.e., by ΔF^* which close to the spinodal is in the order of a few kT (Fig. 4-27a) and, hence, rather low. As pointed out by de Fontaine (1969), in a system close to the spinodal many fluctuations exist, the spatial extent of which is *much smaller* than that of the critical fluctuation; nevertheless, their formation energies are only slightly higher than ΔF^*. In this case, the probability for the alloy to decay via the formation of those 'short-wavelength' fluctuations requiring a slightly higher activation energy is much higher than for a decay via the formation of critical 'long-wavelength' fluctuations.

4.5.1.5 Distinction Between Classical and Non-Classical Nucleation

For a practical application of non-classical nucleation theory to experimental studies of unmixing, the total constraint free energy $f'(c)$ rather far away from equilibrium as well as K^* have to be known in order to calculate the composition profile (Eq. (4-37)) and the nucleation energy (Eq. (4-38)). This is the case only for simple alloy systems and, hitherto, has inhibited the application of the non-classical theory to either scientifically or industrially important alloy systems. Furthermore, so far it has been assumed that a nucleus is in equilibrium with the infinite matrix and that the nuclei do *not* interact amongst each other during the nucleation stage. This may be a valid approximation as long as the supersaturation is small, i.e., where according to Figs. 4-26 and 4-27 classical nucleation theory applies. It ought to become, however, a poor approximation for more concentrated alloys where non-classical nucleation applies. In this case the nucleation rate is high (then the steady state nucleation regime will not be observed) and, hence, the nucleus density large. These complications in non-classical nucleation make it desirable to provide the

experimentalist with a criterion for the applicability of classical nucleation theory which is much easier to handle. Cahn and Hilliard (1959) suggest classical theory will apply if the width l of the (diffuse) interface is considerably smaller than the core of the nucleus where the composition is about constant (Fig. 4-26).

If one assumes that a perceptible nucleation rate is obtained for $\Delta F^* \leq 25\,kT$ (in the literature, $\Delta F^* \approx 60\,kT$ is frequently stated for the maximum barrier at which nucleation becomes measurable; this value, however, is much too high for homogeneous nucleation to occur in solids) and employs Eqs. (4-19) and (4-20), classical nucleation theory may be applied if (Cahn and Hilliard, 1959):

$$l^2 \frac{4\pi\sigma_{\alpha\beta}}{75\,kT} \ll 1 \qquad (4\text{-}39)$$

For *Cu*–Ti ($\sigma_{\alpha\beta} = 0.067$ J m^{-2}; $T = 623$ K), *Fe*–Cu ($\sigma_{\alpha\beta} = 0.25$ J m^{-2}; $T = 773$ K) and *Cu*–Co ($\sigma_{\alpha\beta} = 0.17$ J m^{-2}; $T = 893$ K); this means that the interfacial width has to be smaller than ≈ 0.56, 0.33, and 0.42 nm, respectively, and, hence, has to be rather sharp. So far it has not been possible to measure the composition profile across a *nucleus*/matrix interface. However, analytical field ion microscopy of Cu–1.9 at.% Ti aged at 350 °C for 150 s revealed the Ti concentration of particles with radii of *only* ≈ 1 nm to decrease from 20 at.% (corresponding to Cu_4Ti, cf. Sec. 4.2.1) to that of the matrix within one to two atomic (111)-layers (v. Alvensleben and Wagner, 1984). For the chosen aging conditions nucleation was evaluated to terminate within about 60 s (Kampmann and Wagner, 1984); thus after aging for 150 s the analyzed particles must have already experienced some growth beyond the original size of the nucleus. Nevertheless, these results provide rather good evidence that during nucleation the Cu_4Ti clusters may be considered as droplets with sharp interfaces rather than as spatially extended (long-wavelength) fluctuations with diffuse interfaces even though ΔF^* is only about $10\,kT$.

Although some caution is advisable in treating these tiny particles (critical nuclei in solid state transformation are tens to hundreds of atoms in size) in terms of a continuum theory[1], and assigning them a macroscopic surface and thermodynamic bulk properties, classical nucleation theory seems to be appropriate for an estimation of the nucleation rate. This conclusion will be corroborated in Sec. 4.7.4.

1 Many FIM studies of two-phase alloys (e.g. Cu–1 at % Fe revealed the shapes of even tiny clusters with as little as about twenty atoms to be already compact rather than ramified (Wagner, 1982)

4.5.2 Diffusion-Controlled Growth of Nuclei from the Supersaturated Solid Solution

Suppose that after nucleation the *stable nucleus* is embedded into a still supersaturated matrix. As is illustrated in Fig. 4-28, the particle will then be surrounded by a concentration gradient which provides the driving force for solute diffusion, and thus gives rise to its growth.

The growth rate can be controlled either by the rate at which atoms are supplied to the particle matrix interface by diffusion or by the rate at which they cross the interface. It may be rationalized that for small particles the interface reaction is likely to be the rate controlling step since the diffusion distances are rather short; once the particles have grown to a certain size, the matrix will be depleted from solute atoms and the associated reduction of the driving force makes diffusion likely to be the slower and, thus, rate controlling step (Shewmon, 1965). The transition from one step to the other depends upon the relative magnitudes of solute diffusion and interphase mobility.

©DH Verlagsgesellschaft, 6940 Weinheim
Autor:
Material Science & Technology Vol 5
Herstellter: Herr Schmitt
Umbruch:
Fahnen:
K. Tritsch Würzburg
1. Korr

Satzspiegel DIN A5 Mac-Spalten 24 pt Mon Jul 9 08:47:12 1990
Materialwissenschaft 1. Korrektur

After termination of nucleation it is commonly assumed that the mobility of the interface is sufficiently high in order to allow the solute concentration c_R at the curved interface to achieve local equilibrium (Doherty, 1983). In this case diffusion is the rate controlling step for the growth of *stable* coherent nuclei in a homogeneous precipitation reaction. An analytical solution of the adequate field equation,

$$D\nabla^2 c(r,t) = \frac{\partial c(r,t)}{\partial t} \tag{4-40}$$

requires certain approximations to be made (Zener, 1949). These were critically examined and compared by Aaron et al. (1970) for the diffusion-controlled growth of spherical and platelet-shaped particles. Regardless of the particular approximation used, both the radius R of a spherical precipitate and the half-thickness T of a platelet grow with time according to a *parabolic growth law* as:

$$R = \lambda_1 (Dt)^{1/2} \tag{4-41}$$

and

$$T = \lambda_2 (Dt)^{1/2} \tag{4-42}$$

respectively. The rate constants λ_1 and λ_2 increase with increasing supersaturation, or, more specifically with an increase of the factor

$$k^* = 2\frac{\bar{c}(t) - c_R}{c_p - c_R} \tag{4-43}$$

in a manner which, in particular for larger values of k^*, depends upon the approximation assumed (Aaron et al., 1970). For precipitating intermetallic compounds k^* is one or two orders of magnitude larger (e.g. ≈ 0.3 for γ'-Ni_3Al in *Ni–Al* and ≈ 0.2 for β'-Cu_4Ti in *Cu–Ti*) than for precipitating phases with $c_p \approx 1$ such as *Fe–Cu*, *Cu–Fe*, and *Cu–Co*.

For small supersaturations, $c(r,t)$ in Eq. (4-40) may be approximated as being time-independent. In this case, an isolated spherical particle with radius R surrounded by the concentration field illustrated in Fig. 4-28, will grow at a rate

$$\frac{dR}{dt} = v(R) = \frac{c(t) - c_R}{c_p - c_R}\frac{D}{R} \tag{4-44}$$

©DH Verlagsgesellschaft, 6940 Weinheim
Autor:
Material Science & Technology Vol 5
Umbruch:
Fahnen:
K. Tritsch Würzburg
1. Korr

where D (assumed to be independent on composition) is the volume diffusion coefficient in the matrix. According to the Gibbs Thomson equation, the composition c_R of the matrix phase at a curved interface is different from that of a flat interface the latter being in equilibrium with the equilibrium solute concentration c_α^e of the α-matrix phase, and varies with the precipitate radius as (Martin and Doherty, 1976)

$$\ln \frac{c_R(R)}{c_\alpha^e} = \frac{1 - c_\alpha^e}{c_\beta - c_\alpha^e}\left(\frac{2\sigma_{\alpha\beta}}{R_g T}\frac{V_\beta}{R}\right) - \ln \frac{\gamma_\alpha(c_R)}{\gamma_\alpha(c_\alpha^e)} \tag{4-45}$$

with $\gamma_\alpha(c_R)$ and $\gamma_\alpha(c_\alpha^e)$ being the activity coefficients of the solute atoms in the α-phase at the concentrations c_R and c_α^e, respectively. If the solid solution shows regular solution behavior (γ_α then becomes independent on c), Eq. (4-45) yields the well-known Gibbs-Thomson equation:

$$c_R(R) = c_\alpha^e \cdot \exp\left\{\frac{2\sigma_{\alpha\beta} V_\beta}{R_g T}\frac{1}{R}\right\} \tag{4-46a}$$

or for larger radii in its linearized version,

$$c_R(R) = c_\alpha^e\left(1 + \frac{2\sigma_{\alpha\beta} V_\beta}{R_g T}\frac{1}{R}\right) \tag{4-46b}$$

By assuming a monodispersive particle distribution and $c_R \approx \bar{c}(t \to \infty) = c_\alpha^e$ (or $c_\alpha'^e$), and $\bar{c}(t) \approx c_0$, integration of Eq. (4-44) yields

$$R(t) = \left(2\frac{c_0 - c_\alpha^e}{c_\beta - c_\alpha^e}\right)^{1/2}(Dt)^{1/2} \tag{4-47}$$

It should, however, be pointed out that, so far, there is little experimental evidence for the existence of a precipitation regime during which particle growth strictly follows Eq. (4-47) (Kampmann and Wagner, 1984). In Sec. 4.7.4.3 the reason for this lack of experimental evidence will be provided as well as a guideline to the design of experiments which allow a verification of the existence of diffusion-controlled particle growth with the predicted kinetics to be made. Most quantitative experimental observations of growth rates which yielded good agreement with the diffusion-controlled models outlined above, were confined to large particles, frequently with sizes in the micrometer range (Aaronson et al., 1970; Doherty, 1982).

VCH Verlagsgesellschaft, 6940 Weinheim
Autor:
Material Science & Technology, Vol. 5
Hersteller: Herr Schmitt
Umbruch:
Fahnen:
K. Trillsch, Würzburg
I. Korr.:

4.5.3 The Cluster-Dynamics Approach Towards Generalized Nucleation Theory

As has been pointed out in Sec. 4.5.1.1 the clusters-dynamics approach chosen by Becker-Döring is based on the assumption that the equilibrium cluster distribution function can be specified by Eq. (4-24) and (4-18). Even though the resulting predictions of classical nucleation theory ought to become valid asymptotically for large droplets at small supersaturations there remain some inherent deficits (Binder, 1980; Gunton et al., 1983).

For instance, for small clusters the surface free energy entering Eq. (4-18) should contain size dependent corrections to the macroscopic equilibrium energy of a flat interface. Furthermore, the separation of the droplet formation free energy into a bulk and a surface term appears rather debatable. To avoid some of these deficits, there have been several attempts to develop more accurate descriptions of clusters, taking into account their different sizes and shapes (e.g. Binder and Stauffer, 1976; Stauffer, 1979), and to derive an equilibrium distribution of clusters which is more realistic than the one given by Eq. (4-24). Like in the classical nucleation theory, the latter is an important quantity for a computation of the cluster formation rate in terms of the more recently elaborated theories of cluster dynamics which, in essence, are extensions of the Becker-Döring theory (Binder and Stauffer, 1976; Penrose and Lebowitz, 1979; cf. Gunton et al., 1983 for a general discussion of the various developments).

Unlike Becker-Döring, however, who confined the microscopic mechanism of cluster growth or shrinkage to the condensation or evaporation of monomers (Sec. 4.5.1.1), in their *generalized nucleation theory* Binder and coworkers consider the time evolution of the cluster size distribution function $f(i,t)$ more generally in terms of a *cluster coagulation* or *cluster splitting mechanism*, i.e., in a single cluster reaction step i-mers also ($i = 2, 3, \ldots$) are also allowed to be added or separated from an existing cluster (e.g. Binder, 1977; Mirold and Binder, 1977). Thus, the related kinetic equation for the time evolution of $f(i,t)$ (Binder, 1977),

$$\frac{\mathrm{d}}{\mathrm{d}t} f(i,t) = \sum_{i'=1}^{\infty} \alpha_{i,i'} f(i+i',t) - \tag{4-48}$$

$$- \frac{1}{2}\sum_{i'=1}^{i-1} \alpha_{i',i} f(i,t) + \frac{1}{2}\sum_{i'=1}^{i-1} \beta_{i',i} \cdot$$

$$f(i',t) f(i-i',t) - \sum_{i'=1}^{\infty} \beta_{i,i'} f(i,t) f(i',t)$$

VCH Verlagsgesellschaft, 6940 Weinheim
Autor
Material Science & Technology, Vol. 5
Hersteller: Herr Schmitt
Umbruch:
Fahnen:
K. Trillsch, Würzburg
I. Korr.:

contains four different terms. The first one accounts for an increase of i-mers due to splitting reactions $(i + i') \rightarrow (i, i')$ which are assumed to be proportional to the momentary number $f(i + i', t)$ of clusters of size $(i + i')$ where the proportionality coefficient $\alpha_{i+i'}$ is the rate constant. The second term describes the decrease of i-mers because of splitting reactions $i \rightarrow (i - i', i')$; as a reverse process, coagulation of clusters with sizes $(i - i')$ and i' contributes to a further increase of i-mers (third term), some of which are lost again by coagulation reactions between i-mers and i'-mers to yield $(i + i')$-mers (fourth term). Evidently, for $i' = 1$ the monomer evaporation and condensation process, assumed to be the rate controlling step in the Becker-Döring theory, is contained in Eq. (4-48).

If again, like in classical nucleation (Sec. 4.5.1.1, Eq. (4-25)), detailed balance conditions are assumed to apply between splitting and coagulation, then the rates α and β in Eq. (4-48) can be replaced by a single reaction rate W, e.g.

$$W(i, i') \equiv \alpha_{i+i', i'} C(i + i') = \beta_{i, i'} C(i) C(i') \tag{4-49}$$

Here, $C(i)$ denotes again the cluster concentration which is in thermal equilibrium with the metastable matrix.

Numerical integration of Eq. (4-48) with Eq. (4-49) provides the time evolution of the cluster concentration. This requires, however, a knowledge of the initial cluster distribution $f(i, t = 0)$, of the reaction rates such as $W(i, i')$, and of $C(i)$. These quantities are not commonly available for alloys undergoing phase separation, hitherto this lack has impeded a quantitative comparison between the predictions of the generalized nucleation theory and experimental results on nucleation kinetics.

However, the solution of the kinetic equations with plausible assumptions for the lacking quantities (Mirold and Binder, 1977) has provided a profound, though basically qualitative, insight into the dynamics of cluster formation and growth. As is shown in Fig. 4-29, the initially ($t = 0$) monotonically decreasing cluster size distribution attains for intermediate times a minimum at a size which corresponds to about that of the critical nucleus in classical nucleation theory.

VCH Verlagsgesellschaft, 6940 Weinheim
Autor:
Material Science & Technology, Vol. 5
Herstellen: Hans Schmidt
Umbruch:
Fahnen:
K. Trittsch, Würzburg
Korr

The broad maximum of $f(i, t)$ (which, in fact, does not appear in the corresponding curve of the Becker-Döring nucleation theory [cf. Fig. 4-24]), and its shift to larger sizes with increasing time is due to those particles which have nucleated at earlier times and, hence, have already experienced growth. At $t \rightarrow \infty$, equilibrium is reached. In this case large clusters ($i \rightarrow \infty$) of the precipitated equilibrium phase with composition c_β^e are embedded in a matrix (with composition c_α^e) which then still contains *small* clusters with the equilibrium size distribution shown in Fig. 4-29.

The qualitative features of the $f(i, t)$-curves emerging from the generalized nucleation theory and displayed in Fig. 4-29 are corroborated by computer simulations (cf. Sec. 4.5.6). They are indicative of the occurrence of nucleation and growth as concomitant processes during the early stages of unmixing. For most solids undergoing phase separation, therefore, it is *not possible* to investigate experimentally nucleation and growth as individual processes proceeding subsequently on the time scale. Apart from well designed experiments, commonly it is thus impossible to verify experimentally the kinetics predicted by classical or non-classical nucleation theory (Secs. 4.5.1.1 to 4.5.1.3) or predicted by growth theories (Sec. 4.5.2). This will be substantiated in more detail in Sec. 4.7.4.

The *generalizing character* of the nucleation theory of Binder and coworkers is founded on the fact that, in the sense of Sec. 4.2.3, it comprises nucleation in the metastable regime as well as the transition to spinodal decomposition in the unstable regime of the two-phase region. Consequently, the artificial divergency of both the critical radius R^* of the nucleus and the wavelength λ^* of a critical fluctuation, inherent to the Cahn-Hilliard theories of non classical nucleation (Sec. 4.5.1.4) and spinodal decomposition (Sec. 4.5.4), is no longer discernible on approaching the spinodal line either from the metastable ('nucleation') or from the unstable ('spinodal') regime of the two-phase region (Fig. 4-30). On crossing the spinodal curves the size of a critical cluster decreases steadily until it becomes comparable with the correlation length of typical thermal fluctuations (Binder et al., 1978). Thus, no discontinuity of the mechanism and of the decomposition kinetics is expected to occur on crossing the border between the metastable and unstable regions.

VCH Verlagsgesellschaft, 6940 Weinheim
Autor:
Material Science & Technology, Vol. 5
Umbruch:
Fahnen:
K. Trittsch, Würzburg
Korr

From the experimental point of view it is rather difficult and tedious to obtain *statistically significant* information from directly imaging techniques (FIM, HREM) on the time evolution of the cluster size distribution during the earliest stages of unmixing. (One attempt was made by Si-Qun (1989) by employing HREM to binary Ni-Al alloys.) This information, however, is implicitly contained in the structure function $S(\varkappa, t)$ from small angle scattering techniques, e.g. SAXS or SANS (Sec. 4.3.1.2). Binder et al. (1978) computed the time evolution of $S(\varkappa, t)$ on grounds of their cluster dynamics model. For this purpose, rather crude approximations and simple assumptions had to be made concerning the originally complex shape of the size distribution function of the clusters, their shapes and their composition profiles. Hence, the resulting $S(\varkappa, t)$ is only *qualitative* in nature and can not be used for a quantitative comparison with experimentally obtained structure functions.

As is shown in Fig. 4-31 a, $S(\varkappa, t)$ is predicted to develop a peak the height $S_m \equiv S(\varkappa_m)$ of which increases with time due to the increasing cluster volume fraction; the peak position is shifted towards smaller values of $\varkappa$ reflecting the coarsening of the cluster size distribution with time. Fig. 4-31 b shows the variation of both the peak height $S_m (\varkappa \equiv \varkappa_m)$ and the peak position $\varkappa_m$ with time. On a double-logarithmic plot both curves display some curvature though the shift of $\varkappa_m$ may be reasonably well represented as a power law,

$$\varkappa_m(t) \propto t^{-1/3} \qquad (4\text{-}50)$$

during the 'aging period' covered in Fig. 4-31 a and 4-31 b.

Even though it is not feasible to convert the scaled times shown in Fig. 4-31 a and 4-31 b into real times, experimental SANS curves (Fig. 4-32 a) and the related $S_m(t) \propto \mathrm{d}\Sigma^m(t)/\mathrm{d}\Omega$ (cf. Eq. (4-17)) and $\varkappa_m(t)$-curves (Fig. 4-32 b) from Cu - 2.9 at.% Ti homogenized at T_H, quenched and isothermally aged at 350 °C (Eckerlebe et al., 1986) display the characteristic features qualitatively predicted by the generalized nucleation theory.

VCH Verlagsgesellschaft, 6940 Weinheim
Author:
Material Science & Technology, Vol. 5
Herstellen: Herr Schmitt
Umbruch:
Fahnen:
K. Trillsch, Würzburg
1. Korr.:

4.5.4 Spinodal Theories

As has been pointed out in Sec. 4.2.3 the evolution of non-localized, spatially extended solute-enriched fluctuations into stable second phase particules is treated in terms of spinodal theories. The general concepts of the spinodal theories including more recent extensions, are comprehensively discussed by Binder in Chapter 7 of this volume. We therefore will restrict ourselves to a summary of the essential predictions of those theories which may be examined by experimental studies. Although commonly not justified, in materials science some of these predictions are frequently employed as sufficient criteria to distinguish a spinodal reaction from an unmixing reaction via nucleation and growth.

In their continuum model for spinodal decomposition, which is based on the free energy formalism of a non-uniform binary alloy outlined in Sec. 4.5.1.4 (Eq. (4-36)), Cahn and Hilliard (1959) derived the following (linearized) diffusion equation,

$$\frac{\partial c(r,t)}{\partial t} = \frac{M}{n_v} \nabla^2 \left[\left(\left. \frac{\partial^2 f}{\partial c^2} \right|_{c_0} + 2\eta^2 Y \right) \cdot \nabla^2 c(r,t) - 2M K^* \nabla^4 c(r,t) \right] \qquad (4\text{-}51)$$

for the time dependence of the composition $c(r, t)$ at position r. As the number of atoms per unit volume, n_v, accounts for the fact that the derivative has to be taken with respect to the concentration of component B. M is the atomic mobility and is related to the interdiffusion coefficient $\tilde{D}$ via

$$M \equiv \tilde{D} n_v \Big/ \left. \frac{\partial^2 f}{\partial c^2} \right|_{c_0} \qquad (4\text{-}52)$$

The other symbols entering Eq. (4-51) have been defined in Sec. 4.5.1.4.

As M is always positive, $\tilde{D}$ takes the sign of $\partial^2 f / \partial c^2$ and, thus, is negative inside the spinodal regime (Sec. 4.2.2), giving rise to an *'uphill diffusion'* flux of solute atoms (cf. Fig. 4-6 b).

The linearized version of the more general nonlinear diffusion equation holds if the amplitude $c(r) - c_0$ of the composition fluctuation is rather small and both M and $(\partial^2 f / \partial c^2)|_{c_0}$ are independent of composition. These approximations inherently confine the Cahn-Hilliard theory (CH-theory) to the earliest stages of phase separation.

By expanding the atomic distribution $c(r, t)$ into a Fourier series, Eq. (4-51) can be written as

$$\frac{\partial A(\varkappa)}{\partial t} = R(\varkappa) A(\varkappa) \qquad (4\text{-}53)$$

VCH Verlagsgesellschaft, 6940 Weinheim
Autor:
Material Science & Technology, Vol. 5
Herstellen: Herr Schmitt
Umbruch:
Fahnen:
K. Trillsch, Würzburg
1. Korr.:

with the amplitude

$$A(\varkappa) = \int [c(\mathbf{r}) - c_0] \exp\{i\varkappa \mathbf{r}\}\, d\mathbf{r} \qquad (4\text{-}54)$$

of a Fourier component with wavenumber $\varkappa = \frac{2\pi}{\lambda}$ if λ denotes the wavelength of the composition fluctuation. Eq. (4-51) has a solution for every $A(\varkappa, t)$ with

$$A(\varkappa, t) = A(\varkappa, 0) \exp\{R(\varkappa) t\} \qquad (4\text{-}55)$$

where $A(\varkappa, 0)$ is the initial amplitude of the Fourier component with wavenumber $\varkappa$. The so-called *amplification factor* $R(\varkappa)$ is defined as:

$$R(\varkappa) = -\frac{M}{N_v}\left[\left.\frac{\partial^2 f}{\partial c^2}\right|_{c_0} + 2\eta^2 Y + 2K^* \varkappa^2\right]\varkappa^2 \qquad (4\text{-}56)$$

With reference to Eqs. (4-16), (4-54), and (4-55), the structure function $S(\varkappa, t)$ or the related small angle scattering intensity (Eq. (4-17)) at time t is obtained as

$$S(\varkappa, t) = S(\varkappa, 0) \exp\{2R(\varkappa) t\} \qquad (4\text{-}57)$$

where $S(\varkappa, 0)$ denotes the equal-time structure function of the system equilibrated at the homogenization temperature.

Inside the spinodal region $(\partial^2 f/\partial c^2)|_{c_0}$ is negative. Thus for a given negative value of the latter, $R(\varkappa)$ becomes positive for all wavenumbers $\varkappa$ satisfying

$$\varkappa^2 < \varkappa_c^2 = \left(\left.\frac{\partial^2 f}{\partial c^2}\right|_{c_0} - 2\eta^2 Y\right)\Big/ 2K^* \quad (4\text{-}58\,a)$$

or, respectively for all fluctuation wavelengths λ larger than λ_c with

$$\lambda_c^2 = 4\pi K^* \Big/ \left(\left.\frac{\partial^2 f}{\partial c^2}\right|_{c_0} - 2\eta^2 Y\right) \qquad (4\text{-}58\,b)$$

Long wavelength fluctuations with $\lambda > \lambda_c$ thus will be amplified exponentially whereas short wavelength fluctuations will decay with aging time. For $\lambda_m = \sqrt{2}\cdot\lambda_c$, $R(\lambda)$ attains a maximum giving rise to fastest growth of fluctuations with wavelength λ_m. On approaching the coherent spinodal curve where the denominator in Eq. (4-58b) becomes zero (cf. Sec. 4.5.3), the critical wavelength λ_c diverges in a similar manner as does the critical radius R^* (Fig. 4-30). Thus both the linear theory on spinodal decomposition and the non-classical nucleation theory (Sec. 4.5.1.4) predict abrupt changes in the decomposition kinetics on crossing the spinodal line from either side. This has prompted quite a few experimental studies to determine the spinodal curve on grounds of a kinetic distinction between metastable and unstable states.

In terms of the time evolution of the structure function (Eq. (4-57); now assumed to be isotropic) or the SAS intensity, $S(\varkappa, t)$ should increase exponentially for $\varkappa < \varkappa_c$ with a peak at the *time-independent* position $\varkappa_m = \varkappa_c \sqrt{2}$. Furthermore, all $S(\varkappa)$-curves taken at various times should cross at a *common cross-over point* at $\varkappa_c$.

Most SAXS or SANS studies of binary alloys, oxides, or glasses which were deeply quenched into the miscibility gap did *not corroborate* the predictions of the linearized CH-theory. This is exemplified by Cu - 2.9 at.% Ti isothermally aged at 350 °C. As illustrated in Fig. 4-32b, the peak position of the structure function, which is frequently identified with the mean cluster spacing $T\left(T \approx \frac{2\pi}{\varkappa_m} = \lambda_m\right)$, is *not* found to be time-independent but is rather shifted towards smaller values of $\varkappa$ owing to spontaneous coarsening of the clustering system. Furthermore, *no* common cross over point at any $\varkappa_c$ (Fig. 4-32a) exists nor does $S(\varkappa, t)$ grow exponentially for any value of $\varkappa$ (Fig. 4-33).

According to Eqs. (4-56) and (4-57), a plot of

$$R(\varkappa)\,\varkappa^2 = (1.2\,\varkappa^2)\,\frac{\partial}{\partial t}\ln[S(\varkappa, t)/S(\varkappa, 0)] \qquad (4\text{-}59)$$

versus $\varkappa^2$ should yield a straight line with $R(\varkappa) = 0$ at $\varkappa_c$, whereas a pronounced curvature at larger values of $\varkappa$ has been observed experimentally in alloy (e.g. Fig. 4-34) and glass systems (Neilson, 1969). Cook (1970) attributed this curvature to random thermal composition fluctuations which were not accounted for in the original CH-theory. Even with the incorporation of the thermal fluctuations into the linearized theory, at its best the resulting Cahn-Hilliard-Cook (CHC) spinodal theory is seen (Langer, 1973, Gunton, 1984) to be valid only for the earliest stages of decomposition in systems for which the range of the interaction force is considerably larger than the nearest-neighbour distance, i.e., in systems which are almost mean-field-like in nature. This is not the case for metallic alloys, oxides, and glasses, but is for polymer blends. In fact, results from kinetic studies of decomposition in various polymer mixtures, some of which are cited in Table 4-1 (for a review, cf. Gunton et al., 1983, Binder, Chap. 7, this volume), were found to be consistent with the predictions

of the linearized spinodal theory of Cahn, Hilliard and Cook (e.g. Okada and Han, 1986). In contrast, apart from a recent SANS study on the kinetics of phase separation in Mn–33 at.% Cu (Gaulin et al., 1987), *none* of the scattering experiments on metallic alloys or oxides which are listed in Table 4-1 and which likely had been quenched into the unstable region of the miscibility gap, did corroborate the predictions of the CHC theory. SANS curves taken from Mn–33 at.% Cu during short term aging (between 65 s and 210 s at 450 °C) could be fitted to the CHC structure function with $\varkappa_m$ being time independent during this period. Thus, it was concluded that phase separation in Mn–33 at.% Cu is of the spinodal type and kinetics follow the CHC predictions (Gaulin et al., 1987). The $S(z)$-curve of the as-quenched state already revealed a peak, in fact, at a smaller value of $\varkappa_m$ than for the aged samples. This is indicative of the fact that phase separation already occurred during the quench owing to a finite quench rate. In this case, as has been extensively discussed by Hoyt et al. (1989a), $\varkappa_m$ may indeed become initially time independent, thus pretending an apparent experimental confirmation of the CHC linear approximation.

In the frame work of the mean-field theories the spinodal curve is well-defined as the locus where $\partial^2 f / \partial c^2$ vanishes (Sec. 4.2.2). It can then easily be evaluated, e.g. from an extrapolation of the thermodynamic data which are known for the single-phase solid solution, into the ('mean-field') spinodal regime (Hilliard, 1970). Since, however, neither metallic alloys, nor glass or oxide mixtures behave as mean-field-like systems, *no uniquely defined* spinodal curve exists for these solid mixtures (cf. Binder, Ch. 7.2.5, this volume). Thus in general, it is currently not feasible to predict on theoretical grounds whether a metallic, glass, or oxide solid mixture has been quenched into the metastable or unstable region of the miscibility gap. In this context, it remains debatable whether each of the metallic, glass, or oxide mixtures which were studied by means of SAXS or SANS, and which have been reported to undergo spinodal decomposition (Table 4-1), were truly quenched into and aged within the spinodal region of the phase diagram. Nevertheless, extensive experimental SAXS or SANS studies, in particular on Al–Zn alloys and Fe–Cr (Table 4-1), did not reveal any evidence for a drastic change in the time evolution of the $S(z,t)$ curves with a change in the initial supersaturation. For the Al–Zn systems in particular, it was shown (Simon et al. 1984) that the clustering rate increases rapidly with increasing supersaturation, i.e., both $\varkappa_m$ and S_m are larger the deeper the quench.

Extensions of the Cahn-Hilliard theory of spinodal decomposition to ternary or multicomponent systems have been elaborated by de Fontaine (1972, 1973) and Morral (1971). To our knowledge the kinetic predictions from these extensions have, however, not yet been compared with experimental results, most likely because of difficulties in determining the partial structure functions of ternary alloys (cf. Sec. 4.3.1.2).

As has been pointed out in Sec. 4.2.3, the formulation of a 'unified theory' comprising both nucleation and growth as well as spinodal decomposition can also be attacked on grounds of a spinodal theory. This has been attempted in the statistical model of *L*anger, *B*ar-On and *M*iller (1975) which takes into account thermal fluctuations and nonlinear terms which are neglected in the CH theory. The LBM nonlinear theory of spinodal decomposition also accounts for the later stages of phase separation, though *not* for the coarsening regime. If coherency strains are neglected it approximates the kinetic evolution of the structure function as

$$\frac{\mathrm{d}S(z,t)}{\mathrm{d}t} = -2Mz^2 \cdot \left[\left(K^* z^2 + \frac{\partial^2 f}{\partial c^2}\bigg|_{c_m}\right) S(z,t) + A^*(t)\right] + 2MkTz^2 \qquad (4\text{-}60)$$

With certain approximations, non-linear effects and thermal fluctuations are contained in the term $A^*(t)$ and in the last term, respectively. Setting $A^*(t) \equiv 0$ reproduces the corresponding equation of motion of the CHC-theory, and, if the fluctuation term is also omitted, Eq. (4-57) of the original linear CH-theory is regained. Langer et al. (1975) proposed a computational technique for solving Eq. (4-60). This required several approximations to be made, e.g. on $f(c)$ and on M, which inherently leaves the LBM-approach with some fundamental shortcomings. Nevertheless, with respect to the features displayed in the time evolution of $S(\approx, t)$, the predictions of the LBM-theory (Fig. 4-35) are in rather good agreement with both experimental studies (e.g. Fig. 4-32a and 4-34) and Monte Carlo studies (Sec. 4.5.6, Fig. 4-41).

In their recent study of phase separation in Fe (20, 30, 40, and 60) at.% Cr alloys, Furukawa et al. (1986) compared the experimental $S(\approx, t)$ curves with Eq. (4-60) of the LBM-theory. For shorter aging times at 515 C, the experimental data points taken from Fe - 40 at.% Cr could well be fitted by Eq. (4-60) (Fig. 4-36) if $kT\,K^*$, $M\,K^*$, and $A^*\,K^*$ were employed as three independent fitting parameters. On the grounds of the agreement with the spinodal theory of LBM, and, additionally, as this particular alloy was evaluated to lie within the (mean-field) spinodal region, it has been concluded that Fe-40 at.% Cr is a *'spinodal alloy'*.

Recently the nonlinear theory of spinodal decomposition developed by Langer (1971) for binary alloys was extended to ternary systems (Hoyt, 1989) by deriving the time dependent behavior of the three linearly independent partial structure functions (cf. Sec. 4.3.1.2). An experimental examination of the kinetic predictions, however, is still lacking.

VCH Verlagsgesellschaft 6940 Weinheim
Autor:
Material Science & Technology, Vol. 5
Hersteller: Herr Schmitt
Umbruch:
Fahnen:
K. Trilisch, Würzburg
1. Korr.:

4.5.5 The Philosophy of Defining a 'Spinodal Alloy' - Morphologies of 'Spinodal Alloys'

Referring to the previous section it is rather difficult or even impossible to assess on a thermodynamic basis whether an alloy, glass, or oxide system was truly quenched into and aged within the spinodal region of the miscibility gap. Furthermore, the various spinodal theories are difficult to handle and many parameters entering the resulting kinetic equations are commonly not available for most solid mixtures. Hence, like the non-classical nucleation theory, the various elegant theories which describe the kinetics of phase separation of a 'spinodal alloy' are of little use for the practical metallurgist.

Because of these problems, materials scientists have up to now employed *morphological criteria* for the definition of a 'spinodal alloy'. These are simply related to the predictions of the linear spinodal CH-theory concerning the morphological evolution of a solid mixture undergoing spinodal decomposition.

Most crystalline solid solutions show a variation of lattice parameter with composition leading to coherency strains. The associated strain energy $f_{el} = \eta^2 Y(c - c_0)^2$ (Eq. (4-35)) which is accounted for in Eq. (4-51), reduces the driving force for phase separation. This effect shifts the locus of the original *chemical* (mean field) spinodal to lower temperatures yielding the *coherent* spinodal curve (Eq. (4-58)). If the parameter Y (cf. Sec. 4.2.4) which is a combination of various elastic constants, depends on the crystallographic direction, f_{el} also becomes anisotropic. Therefore, the locus of the coherent spinodal may also vary with the crystallographic direction. This becomes particularly discernible for the tetragonal TiO_2-SnO_2 oxide system (Park et al., 1976), where f_{el} attains a minimum for composition waves along [001] and is larger for waves along [100] and [010]. Hence, the coherent spinodal splits up into a [001], a ⟨101⟩, and a ⟨100⟩ branch (Fig. 4-37). As a consequence the SnO_2-rich modulations form preferentially along [001] giving rise to a lamellar structure at later aging stages (Fig. 4-38). For most cubic metallic systems the elastic anisotropy parameter A (Sec. 4.2.4a) is positive, rendering the minimum f_{el} along the elastically soft ⟨100⟩ directions. According to the CH-theory the growth rate will thus be

VCH Verlagsgesellschaft 6940 Weinheim
Autor:
Material Science & Technology, Vol. 5
Hersteller: Herr Schmitt
Umbruch:
Fahnen:
K. Trilisch, Würzburg
1. Korr.:

highest along the three ⟨100⟩ directions giving rise to the frequently observed modulated precipitate microstructures (Table 4-2, Figs. 4-18, 4-19 b). In isotropic materials such as polymers, glasses, or, for instance, Fe–Cr and Fe–Cr–Co alloys, the modulations do not grow along any preferential directions. The resulting two-phase microstructure is of the 'sponge-like' type and sometimes referred to as a *'mottled'* or *'interconnected'* precipitate microstructure (e.g. Figs. 4-16, 4-19 c, 4-20). Based on these considerations, two-phase alloys displaying either *lamellar*, *modulated*, or *interconnected* precipitate microstructures are commonly termed *'spinodal alloy'* by metallurgists. Furthermore, sometimes the morphology of a two-phase material is even employed to derive the locus of the spinodal. This is illustrated in Fig. 4-39 for the Cr-rich ferrite phase of a cast duplex stainless steel which undergoes phase separation during tempering between 350 °C and 450 °C with an associated embrittlement (Auger et al., 1989). Increasing the Cr content of the ferritic Fe–Ni–Cr solid solution leads to the formation of Cr-rich α'-precipitates during tempering. As the α'-phase is discernible as individual particles by CTEM, it is concluded that phase separation occurred via nucleation and growth. A further increase of the Cr content to about 25 wt.% yielded a 'sponge-like' microstructure after tempering below 400 °C. This was attributed to a spinodal mechanism. Thus the spinodal is drawn as the line which separates the two morphologies (Fig. 4-39).

It must be pointed out, however, that interconnected or modulated structures represent two-phase microstructures in the *later* stages of the reaction (e.g. Fig. 4-18). Even though they are widely believed to result from spinodal decomposition in the sense of the CH-theory, their formation might be of a rather different origin. For instance, a strong elastic interaction of a high number density of individual nuclei, each of which is surrounded by a solute depleted zone in which no further nucle-

VCH Verlagsgesellschaft, 6940 Weinheim
Autor:
Material Science & Technology, Vol. 5
Hersteller: Herr Schmitt
Umbruch:
Fahnen:
K. Trittsch, Würzburg
1. Korr.

ation may occur, may also lead to regularly arranged precipitates, i.e., modulated structures (Ardell et al., 1966; Doi et al., 1984, 1988; Doi and Miyazaki, 1986). On the other hand, initially interconnected microstructures in Cu–Ni–Fe alloys were found to break up into isolated plates (Piller et al., 1984). The later stage microstructure is thus neither sufficient to draw any conclusions on the early stage decomposition mode nor for a definition of a 'spinodal alloy'. We therefore are still left with the question what really is a spinodal alloy? To answer this question unequivocally, one must verify by any microanalytical technique that the amplitude of the composition waves increases gradually with time until the evolving second phase has finally reached its equilibrium composition. Such an experimental verification is a difficult task and, to our knowledge, was only shown for decomposing Fe–Co–Cr (Fig. 4-16 and 4-17), AlNiCo permanent magnetic materials (Hütten and Haasen, 1986) and Fe–Cr (Brenner et al., 1984) by means of AFIM, and for a phase separating polystyrene-polyvinylmethylether polymer mixture employing nuclear magnetic resonance methods (Nishi et al., 1975).

As has been outlined in Sec. 4.2.3, regardless of whether phase separation occurs via nucleation and growth or via spinodal decomposition, the underlying microscopic mechanism is diffusion of the solvent and solute atoms. In this sense there is thus no necessity to distinguish amongst the two different decomposition modes and the term 'spinodal alloy' is simply *semantic* in nature. This is also reflected in the various attempts to develop 'unified theories' comprising either mode.

VCH Verlagsgesellschaft, 6940 Weinheim
Autor:
Material Science & Technology, Vol. 5
Hersteller: Herr Schmitt
Umbruch:
Fahnen:
K. Trittsch, Würzburg
1. Korr.

From the practical point of view the microstructure of virtually all technical two-phase alloys corresponds to that of the later stages. Hence, the practical metallurgist worries little about the initial stages of unmixing but is instead interested in predicted the growth and coarsening behavior of precipitate microstructures in the later stages. This will be the subject of Secs. 4.6 and 4-7.

4.5.6 Monte Carlo Studies

The basic features of early stage composition as a stochastic process have been extensively studied in model alloys by means of Monte Carlo computer simulations, mainly by Lebowitz, Kalos, and coworkers (Lebowitz and Kalos, 1976; Binder, 1979; Marro et al., 1975, 1977; Penrose et al., 1978; Lebowitz et al., 1982; see also Binder in Chapter 4 of this volume). The binary model alloys are usually described in terms of a three-dimensional Ising model with nearest-neighbour interactions on a simple cubic lattice the sites of which are occupied by either A or B atoms, and a phase diagram which displays a symmetrical miscibility gap centered at 50 at.% solute concentration (Fig. 4-40). The microscopic dynamics of this system are commonly described by the Kawasaki model (Kawasaki, 1972). There a nearest neighbor pair of lattice sites is chosen at random, then the atoms on those sites may be interchanged with a probability which depends on the energies of the configuration before and after the exchange in such a way that detailed balancing holds (Penrose, 1978). Monte Carlo techniques are then employed to carry out this stochastic process.

The model alloys employed for MC simulations are far from being representative of a real binary alloy system. One reason is the fact that the atomic exchange is assumed to occur directly rather than indirectly via the vacancy mechanism. Nevertheless, MC simulations represent a convenient way to study in a quantitative microscopic manner the time evolution of the cluster configuration and the structure function in an 'alloy' quenched into any region below the solubility line (Fig. 4-40) without worrying about complicating factors, such as an insufficient quenching rate, excess vacancies, or lattice defects, which one commonly faces when investigating real alloys (Sec. 4.3.2). Furthermore, MC simulations have allowed a critical examination of the various theoretical approaches in terms of cluster dynamic models or spinodal models to be made. For practical computational limitations, however, the maximum size of the model alloy has commonly been restricted to $50 \times 50 \times 50$ lattice sites. Because of this size limitation, in general, computer experiments can only cover the early stages of a precipitation reaction in alloys where the supersaturation is sufficiently high for the formation of a large number density of clusters or nuclei, and where the cluster sizes are still considerably smaller than the linear dimension of the model system. This is frequently not the case in real alloys. For instance, once nucleation is terminated, the maximum number density of Cu_4Ti particles in Cu - 1.9 at.% Ti aged at 350 °C ($\Delta F^*/kT \approx 8$) is found to be about $10^{25}\ m^{-3}$ with diameters of ≈ 2 nm (von Alvensleben and Wagner, 1984). This would correspond to only fifteen precipitates within a simple cubic lattice with $50 \times 50 \times 50$ sites typically used in MC simulations. The same crystal would contain even less than one Co-rich particle at the end of the nucleation period in Cu - 1 at.% Co ($\Delta F^*/kT \approx 25$) aged at 620 °C (LeGoues and Aaronson, 1984). Thus for such an alloy with a large nucleation barrier, computer simulations may cover, at best, the transient period of nucleation but certainly not the entire nucleation period.

In essence, the results from computer simulations corroborate the predictions both from the generalized nucleation theory of Binder and coworkers (Sec. 4.5.3) and from the non-linear spinodal LBM-approach. In particular, the time evolution

model displays qualitatively the same features as the corresponding ones obtained from the latter theories (cf. Figs. 4-31 a and 4-35 b) or from experiment (e.g. Fig. 4-32 a). For instance, $S(k,t)$ of 'alloy' #4 (Fig. 4-41 b), which according to Fig. 4-40 lies close to the spinodal line within the metastable regime, evolves similarly to that of 'alloy' #5 quenched into the center of the spinodal region. Thus, in agreement with the generalized nucleation theory and the LBM-spinodal approach, but unlike the predictions of linearized CH-theory of spinodal decomposition, MC simulations again reveal i) *no* evidence for any *abrupt change* of the decomposition kinetics on crossing the spinodal curve, ii) *no common cross-over point* of the $S(k)$-curves taken after different aging times, iii) *no exponential growth* of the scattering intensity for a certain time-independent wave vector in any time regime, and, furthermore, iv) the peak position of $S(\approx, t)$ at $\approx_m$ is *not* found to be *time-independent* but is shifted towards smaller values of $\approx$ indicating the immediate growth of clusters.

Frequently, the MC data for the time evolution of the peak position ($\approx_m$) and the peak height (S_m) of the structure function have been fitted to simple power-laws (cf. Sec. 4.8.2), such as $\approx_m(t) \propto t^{-a}$ and $S_m(t) \sim t^b$; a and b were estimated to range from 0.16 to 0.25 and 0.41 to 0.74, respectively, depending on the initial supersaturation of the 'alloy' (Marro et al., 1975, 1977; Sur et al., 1977). Lebowitz et al. (1982) have pointed out, however, that due to the finite (small) size of the system it is difficult to extract from computer simulations precise and reliable information about the analytical form of $\approx_m(t)$, e.g., and that it is possible to fit the same MC data with other functional forms than the power-laws given above. In Sec. 4.8.2 we shall show, in fact, that apart from the late stages of coarsening, it is commonly not feasible to interpret experimental kinetic data *over an extended aging period* in terms of a power-law behavior with a time independent exponent.

VCH Verlagsgesellschaft, 6940 Weinheim
Autor:
Material Science & Technology, Vol 5
Herstellter Herr Schmitt
Umbruch:
Fahnen:
K. Trillsch, Würzburg
1. Korr.

4.6 Coarsening of Precipitates

4.6.1 General Remarks

For most two-phase alloys, the simple model of diffusional growth of isolated non-interacting particles with uniform size Eq. (4-47) is based on, frequently does not give a realistic description of the further dynamic evolution of the precipitate microstructure beyond its nucleation stage. In reality, towards the end of the nucleation period a more or less broad particle size distribution $f(R)$ is established (Fig. 4-10 and 4-29). According to the Gibbs-Thomson equation (4-46), the solubility $c_R(R)$ of *small* particles with a large ratio of surface area to volume is larger than that for *larger* ones. With reference to Eq. (4-44), this leads to a size-dependent growth rate, which is positive for larger particles with $\bar{c} > c_R$ and negative for smaller ones with $\bar{c} < c_R$. The growth rate becomes zero for particles with $\bar{c} = c_R$ which are in unstable equilibrium with the matrix. Their radius R^* is derived from Eq. (4-46) as

$$R^* \approx \frac{2\sigma_{\alpha\beta} V_m}{R_g T} \frac{1}{\ln \frac{\bar{c}}{c_\alpha^e}} \equiv K' \sigma_{\alpha\beta} \frac{1}{\ln \frac{\bar{c}}{c_\alpha^e}} \quad (4\text{-}61)$$

Hence, driven by the release of excess interfacial free energy, larger precipitates will grow at the expense of smaller ones which dissolve again giving rise to a change of the precipitate size distribution. This process, which is commonly referred to as *coarsening* or *Ostwald ripening*[1], frequently reduces the precipitate number density from $\approx 10^{25}\,m^{-3}$ to less than $10^{19}\,m^{-3}$ in typical two-phase alloys during aging (cf. Fig. 4-3). Usually, the coarsening process is considered to be confined to the latest stages of a precipitation reaction. However, as will be shown in Sec. 4-7, coarsening may accompany the growth process outlined in Sec. 4.5.2, or may even start while the system is still in its nucleation period depending on the initial supersaturation of the solid solution.

[1] In its original meaning, Ostwald ripening is confined to a coarsening reaction where the second phase particles act as the only sinks or sources of solute atoms

Umbruch:
VCH Verlagsgesellschaft, 6940 Weinheim

4.6.2 The LSW-Theory of Coarsening

In essence, the coarsening of randomly dispersed second phase particles is a multi-particle diffusion problem which is difficult to handle theoretically. In their classic LSW-coarsening theory, *Lifshitz* and *Slyozov* (1961), and *Wagner* (1961) calculated the time evolution of $f(R,t)$ which satisfies the continuity equation:

$$\frac{\partial f}{\partial t} + \frac{\partial}{\partial R}\left[f\,\frac{\partial R}{\partial t}\right] = 0$$

On the basis of the continuity equation and of Eq. (4-44), the time evolution of the mean particle radius $\bar{R}(t)$ and the precipitate number density $N_v(t)$ are derived. Certain approximations, however, had to be made in order to solve the equations of motion analytically:

a) The precipitated volume fraction $f_p = (4\pi/3)\bar{R}^3 N_v$ is close to zero, i.e., the system is highly diluted. Under such a condition, a particle the interface of which is in local equilibrium, interacts only with the infinite matrix; interactions with the specific environment of adjacent particles as expected in less-diluted systems may thus be ignored.

b) $f_p \approx$ const., i.e., the decomposition is close to completion and, thus the supersaturation $\Delta c \approx 0$. This inherently confines the LSW-theory to the late stages of a precipitation reaction.

c) The linearized version, Eq. (4-46 b), of the Gibbs-Thomson equation may be used.

VCH Verlagsgesellschaft, 6940 Weinheim
Autor:
Material Science & Technology, Vol. 5
Herausgeber: Herr Schmitt
Umbruch:
Fahnen:
K. Trittsch, Würzburg
1. Korr.

With these approximations, the LSW theory yields in the asymptotic limit ($t \to \infty$) for a diffusion-controlled process the coarsening rate of $\bar{R}$ to be proportional to the cube root of the time, or more specifically,

$$\bar{R}^3(t) - \bar{R}_0^3 = \frac{4}{9} K' D \sigma_{\alpha\beta} \frac{c_\gamma^e}{c_p - c_\gamma^e} t \equiv \alpha_{LSW} t \qquad (4\text{-}62\,a)$$

and accordingly for the decrease of N_v with time:

$$N_v^{-1}(t) - N_{v_0}^{-1} = \frac{4\pi}{3} f_p^{-1} \alpha_{LSW} t \qquad (4\text{-}62\,b)$$

$\bar{R}_0$ and N_{v_0} denote the mean particle radius and number density at the onset ($t = 0$) of coarsening. With $\bar{R} = R^*$ and $\bar{R}(t) \gg \bar{R}_0$, Eq. (4-62 a) yields for the supersaturation:

$$\Delta c(t) = \left[\frac{4}{9} K' (c_\gamma^e)^2 \frac{V_m}{f_p} \frac{D}{\sigma_{\alpha\beta}^2}\right]^{-1/3} t^{-1/3} \qquad (4\text{-}63)$$

The asymptotic solution of the size distribution is of the form (Fig. 4-42):

$$f_{LSW}(R,\bar{R},t) = \frac{N_v(t)}{\bar{R}(t)} h(R/\bar{R}) \quad \text{for } R/\bar{R} < 1.5 \qquad (4\text{-}64)$$

$$f_{LSW}(R,\bar{R},t) = 0 \quad \text{for } R/\bar{R} \geq 1.5$$

and contains the *time invariant shape function* $h(R/\bar{R})$; in this limit, $\bar{R}(t)$ is identical with $R^*(t)$.

Numerous experimental studies on a large variety of two-phase alloys attempted to examine the coarsening kinetics predicted by the LSW-theory. Regardless of the particular alloy system and the employed microanalytical technique (e.g. CTEM on Ni–Al and Ni–Ti: Ardell, 1967, 1968, 1970; AFIM on Ni–Al: Wendt and Haasen, 1983; SANS on Fe–Cu: Kampmann and Wagner, 1986), these studies commonly revealed the experimental size distribution function to be considerably broader than $f_{LSW}(R,t)$ (Fig. 4-42) whereas a plot of $\bar{R}^3 - \bar{R}_0^3$ or $N_v^{-1} - N_{v_0}^{-1}$ versus t yielded more or less straight lines (due to limited statistics, the error bars are usually rather large). From the sloper of these *LWS-plots* the product $\sigma_{\alpha\beta} \cdot D$ can be derived. Frequently Δc was also measured and plotted versus $t^{-1/3}$ (Eq. (4-63)) in order to determine $D/\sigma_{\alpha\beta}^2$ (e.g. Ardell, 1967, 1968; Wendt and Haasen, 1983). Thus apparently absolute values for both $\sigma_{\alpha\beta}$ and D have been determined from values of $D\sigma_{\alpha\beta}$ and $D/\sigma_{\alpha\beta}^2$. However, Eq. (4-62) and, in particular, Eq. (4-63) and the rate constant (α_{LSW}) in Eq. (4-62 a) were derived with the assumption b): $\Delta c \approx 0$ for $f_p \approx$ const. Once this condi-

VCH Verlagsgesellschaft, 6940 Weinheim
Autor:
Material Science & Technology, Vol. 5
Herausgeber: Herr Schmitt
Umbruch:
Fahnen:
K. Trittsch, Würzburg
1. Korr.

tion is fulfilled, it is no longer feasible to follow minor changes of Δc with time quantitatively by any of the experimental techniques frequently employed, such as CTEM, AFIM, SAXS or SANS (Sec. 4.3.1); in the asymptotic limit $\Delta c \to 0$, it even appears difficult to measure $\Delta c(t)$ in alloys containing a ferromagnetic phase with magnetic techniques (Ardell, 1967, 1968), though these direct methods are certainly more sensitive than CTEM, AFIM or SAS. On the other hand, in those earlier decomposition stages, where $\Delta C(t)$ is experimentally accessible, a LSW-analysis *cannot* be performed, and, in particular, the rate constant α_{LSW} (Eq. (4-62a)) is no longer valid (see Sec. 4.7.4.3). Thus, in practice, an LSW-analysis, at its best, can be performed only in diluted systems on the basis of Eq. (4-62a) and yields only a value for the *product* $D \cdot \sigma_{\alpha\beta}$. This fact was ignored in most LSW-analyses based on the independent measurement of both $\bar{R}(t^{1/3})$ and $\Delta c(t^{-1/3})$; hence, the values of D and $\sigma_{\alpha\beta}$ derived from this type of analysis must be regarded with some reservation. However, in Sec. 4.7.4.4 two different methods will be discussed which allow a separate derivation of $\sigma_{\alpha\beta}$ and D to be made from experimental data, one method with even knowing $\Delta c(t)$.

A priori, it is difficult to check to what extent α_{LSW} in Eq. (4-62a) is affected by the usage of Eq. (4-46b) rather than Eq. (4-46a) or Eq. (4-45). This approximation is suggested to be valid for $R > 3K'\sigma_{\alpha\beta}$ (Wagner, 1961) which corresponds to $\ln(\bar{c}/c_\infty^\alpha) \approx \bar{c}/c_\infty^\alpha - 1$. Since, however, one is dealing with a distribution function, $R > 3K'\sigma_{\alpha\beta}$ has to be satisfied not only for $\bar{R}$ but also for particles within $f(R,t)$ which are considerably smaller than $\bar{R}$. This is the case for all particles in the Ni–14 at.% Al system even during the early stages of precipitation since $3K'\sigma_{\alpha\beta} \approx 0.5$ nm ($\sigma_{\alpha\beta} = 0.016$ J/m^2, see Sec. 4.7.4.4). In contrast, for Cu–1.9 at.% Ti aged at 350 °C, $3K'\sigma_{\alpha\beta} = 3.7$ nm; hence, linearization of Eq. (4-46a) becomes reasonable only in the late stages of the precipitation reaction. (In Sec. 4.7.4.3 the influence of linearization of Eq. (4-46a) on $f(R,t)$ for Cu–Ti will be discussed in more detail.)

VCH Verlagsgesellschaft, 6940 Weinheim
Autor:
Material Science & Technology, Vol. 5
Hersteller: Herr Schmitt
Umbruch:
Fahnen:
K. Triltsch, Würzburg
1. Korr.:

4.6.3 Extensions of the Coarsening-Theory to Finite Precipitate Volume Fractions

There have been many efforts to extend the LSW-theory to the more realistic case of finite precipitated volume fractions and to investigate its influence on the shape of $f(R,t)$, its time invariance, and on the coarsening kinetics of $\bar{R}$ (Ardell, 1972; Brailsford and Wynblatt, 1979; Davies et al., 1980; Tsumuraya and Miyata, 1983). Basically most of these extensions attempted to consider the particle interaction for finite volume fractions in terms of a modification of the diffusion geometry and, thus, of the concentration gradient around a particle with a given size. Regardless of the statistical averaging procedure necessarily employed in these (still 'mean-field-like') LSW-extensions in order to evaluate the mean effective diffusion field, they jointly recapture the $\bar{R} \propto t^{1/3}$ kinetic behavior but predict the rate constants to increase, and the particle distribution to flatten and to broaden with increasing volume fraction.

In the mean-field type LSW-theory and its above-mentioned extensions to finite volume fractions, particles with $R > R^*$ grow and those with $R < R^*$ dissolve with a rate which depends only on their specific size (e.g. Eq. (4-44)). In reality, however, and in particular for non-zero volume fractions, the precise growth rate of a given particle will depend on the details of its *local* environment rather than on a constant effective diffusion field. This fact was taken into account more recently by employing systematic statistical physics analyses to diffusion-controlled particle growth (Marqusee and Ross, 1983; Tokuyama and Kawasaki, 1984). Solutions to the related multi-particle diffusion problem of particles interacting through their diffusion fields at various volume fractions were obtained from computer simulations (Voorhees and Glicksman, 1984; Enomoto et al., 1987).

VCH Verlagsgesellschaft, 6940 Weinheim
Autor:
Material Science & Technology Vol 5
Umbruch:
Fahnen:
K. Triltsch, Würzburg

From the computer simulations it became possible to calculate the 'source/sink strength' B_i of individual particles with radius R_i in different environments. B_i is related to the particle growth rate via $\dot{R}_i = B_i R_i^2$. Thus, particles with $B_i > 0$ will grow, while those with $B_i < 0$ will shrink during further aging. In Fig. 4-43 the distribution of B_i is plotted versus the normalized particle size $R_i/\bar{R}$ for a concentrated precipitating system with $f_p = 0.35$ undergoing coarsening under steady state conditions. It is evident that particles with identical sizes may have different growth rates owing to different local environments (Voorhees and Glicksman, 1984). In contrast, the LSW-theory predicts the source/sink strength as $B_{LSW} = (R/\bar{R}) - 1$ and, hence, assigns to each given particle size just one unique value of B.

Despite the observed dependence of the growth rate of an individual precipitate on its local environment, the computer simulations of the multi-particle diffusion problem have established that regardless of the volume fraction, $\bar{R}^3$ coarsens linearly with time; the rate constant $\alpha(f_p)$, however, depends on f_p as is shown in Fig. 4-44 for various theoretical approaches and numerical techniques.

Evidently, the different theoretical approaches predict somewhat different coarsening rates for a given f_p. From the practical point of view, however, the consistency is sufficient for a prediction of the coarsening rate of a two-phase system.

Furthermore, the computer simulations revealed that at non-zero volume fractions the shape of the normalized size distribution also becomes time invariant in the asymptotic limit regardless of the initial distribution at the beginning of coarsening. The particular shape of the steady-state distribution, however, depends on f_p and becomes flatter and broader the large f_p (Fig. 4-45). Hence, the observed differences between experimental size distributions and f_{LSW} (e.g. Fig. 4-42) can be attributed to particle interactions not accounted for in the original LSW-theory. Systematic experiments on the late stage coarsening kinetics and the shape of $f(R, t)$ as a function of f_p, however, are still lacking.

VCH Verlagsgesellschaft, 6940 Weinheim
Autor:
Material Science & Technology, Vol. 5
Herausgeber: Horst Schmalt

Umbruch:
Fahnen.
K. Trillsch, Würzburg
1. Korr.:

4.6.4 Other Approaches Towards Coarsening

In addition to the LSW-type coarsening mechanism which is based on the evaporation and condensation of *single* atoms from dissolving and growing precipitates, Binder and Heermann (1985) have also considered a *cluster-diffusion-coagulation mechanism* likely to become operative during the *intermediate* stages of coarsening. Depending on the specific (local) microscopic diffusional which is assumed to contribute to the shift of the center of gravity of the particle and their likely coagulation, the time exponents a for the related coarsening rate were evaluated between $a = 1/6$ and $a = 1/4$ and, hence are smaller than predicted by the LSW-theory ($a = 1/3$).

According to Fig. 4-32b the position of the SANS-peak intensity at x_m varies in proportion to $t^{0.25}$. This might, in fact, be interpreted in terms of a cluster-diffusion-coagulation mechanism being dominant prior to LSW-type coarsening. In Sec. 4.8.2 it will be shown, however, that even if single atom evaporation or condensation in the LSW sense is assumed to be the only microscopic mechanism contributing to particle growth, the time exponent a already displays a strong time dependence. Depending on the initial supersaturation of the alloy, $a(t)$ may then vary between almost zero and 0.5 during the course of a precipitation reaction. The question of whether a even reaches its asymptotic value 1/3 depends on whether the experiment spans a sufficiently long range of aging times.

From the experimental point of view it thus does not appear feasible to decide merely on grounds of the measured time exponent whether the cluster-diffusion-coagulations mechanism influences the growth or coarsening kinetics of a precipitate microstructure.

4.6.5 Influence of Coherency Strains on the Mechanism and Kinetics of Coarsening – The Problem of Stability Bifurcations

The LSW-theory as well as the extensions to finite volume fractions assume the coarsening process to be driven entirely by the associated release of interfacial energies. In the presence of elastic strains, however, such as induced by coherency strains, the coarsening process may be driven by a release of the total energy of the two-phase

VCH Verlagsgesellschaft, 6940 Weinheim
Autor:
Material Science & Technology, Vol. 5
Herausgeber: Horst Schmalt

Umbruch:
Fahnen.
K. Trillsch, Würzburg
1. Korr.:

microstructure $U_{tot} = U_{surf} + U_{str} + U_{int}$, comprising the surface energy and *additionally* the elastic strain energy and the interaction energy between neighbouring precipitates.

In the presence of misfit strains, elastic interaction may give rise to pronounced changes of the shape and spatial correlation of the particles. Ardell et al. (1966) proposed elastic interaction between γ'-Ni_3Al precipitates to establish a fairly uniform particle distribution along the elastically soft ⟨100⟩ directions during coarsening of Ni–Al alloys. In fact, at a first glance, CTEM of many nickel-base alloys reveals the γ'-type precipitates to be rather uniformly distributed (e.g. Fig. 4-19c) which is sometimes reminiscent of modulated structures.

More recently it was observed (Miyazaki et al., 1982; Doi et al., 1984) that during coarsening individual cuboidal γ'-type precipitates split up into groups of two (e.g. in Ni–Ti, Ni–Al, and Ni–Cu–Si alloys) or even eight (e.g. in Ni–Si, Ni–Al, Ni–Al–Ti alloys) smaller cuboidal precipitates (Fig. 4-46). The observed splitting has not been accounted for by the conventional coarsening theory and, thus, has prompted a theoretical reexamination of the influence of elastic interactions on the stability of precipitate microstructures during coarsening (Johnson, 1984; Miyazaki et al., 1982, 1986; Johnson et al., 1988), and on the degree of regularity in the particle distribution (Doi et al., 1988). Commonly the multi-particle interaction problem has been reduced to considering, on the basis of isotropic or anisotropic microelasticity theory, only a *pair* of diffusionally and elastically interacting spherical particles with radii R_1 and R_2 and a constant total volume $V^0 = 4\pi/3(R_1^3 + R_2^3)$. The relative size change of the two particles may be expressed by introducing the parameter (Johnson, 1984)

$$R^0 = \frac{R_1 - R_2}{R_1 + R_2} \qquad (4\text{-}65)$$

In the paradigm of Ostwald-ripening where the larger ~~[larger]~~ particle will grow at the expense of the smaller one, the extreme values of R^0 are ± 1; for $R^0 \equiv 0$, both particles have equal sizes. By assuming a fairly periodic distribution of particles with a center-to-center distance L between the two particles, their volume fraction f_p may be approximated by

$$f_p = \frac{V^0}{2L^3} = \frac{\pi}{6d^3} \qquad (4\text{-}66)$$

VCH Verlagsgesellschaft, 6940 Weinheim
Autor:
Material Science & Technology, Vol. 5
Hersteller: Herr Schmitt
Umbruch:
Fahnen:
K. Tiltsch, Würzburg
1. Korr.:

with $d \equiv L \cdot 2\bar{R} \geq 1$ being the [illegible] distance normalized with respect to the mean particle diameter $2\bar{R}$. (For $d = 1$ the particles just touch each other.) According to Eq. (4-66), the precipitated volume fraction is now fully determined by d regardless of the particle volume V^0 (Miyazaki et al., 1986). Fig. 4-47 shows the variation of the elastic interaction energy ($F_{int.}$) normalized by the elastic strain energy ($F_{str.}$) with the intercenter distance or the related volume fraction for various relative particle sizes R^0. Evidently the elastic interaction decays rapidly with increasing interparticle distance or decreasing volume fraction and is strongest (the most negative) if the two particles have the same size ($R^0 \equiv 0$), as is the situation after splitting of a γ'-particle into a pair of two γ'-plates (Fig. 4-46). Fig. 4-48 shows the dependence of the total energy as a function of the relative particle size for three different normalized center-to-center distances d or, as $2\bar{R} = 200$ nm was kept constant, for three different volume fractions f_p. At smaller f_p or larger d, the total energy is dominated by the surface energy which is largest if the two interacting particles have equal sizes, i.e., for $R^0 = 0$. Hence, the two-particle system can minimize its total energy if it follows the paradigm of Ostwald-ripening where the larger particle grows at the expense of the smaller one until $R^0 = \pm 1$ is reached. According to Fig. 4-47, the influence of the elastic interaction energy increases with decreasing d and is largest for $R^0 = 0$. Thus below a certain interparticle distance (e.g. $d = 1.6$ in Fig. 4-48), $F_{tot.}$ additionally develops a local minimum around $R^0 = 0$ which even becomes absolute if the volume fraction is still further increased, e.g. to about 40%. The larger surface energy of the two-particle system with $R_1 = R_2$ is now compensated by the strong (negative) elastic interaction energy. The occurrence of three minima in the $F_{tot.}(R^0)$ curve which are separated by the maxima at R^0_{max} (the *bifurcation points*) gives rise to *'stability bifurcations'* during coarsening. A pair of precipitates with $|R^0| > R^0_{max}$ can lower its total energy by approaching a final state with $R^0 = \pm 1$ via the growth of the larger particle at the expense of the smaller one, i.e., via Ostwald-ripening. In contrast, a pair of particles with $|R^0| < R^0_{max}$ adopts its minimum energy state if the smaller particle grows at the expense of the larger one until both have equal sizes, i.e., $R^0 = 0$. If the energy

VCH Verlagsgesellschaft, 6940 Weinheim
Autor:
Umbruch:
Fahnen:

minimum at $R^0 = 0$ is absolute, the one-particle state at $R^0 = \pm 1$ is metastable and the pair of *equal-sized* precipitates at $R^0 = 0$ represents the stable configuration. In this case the splitting of a particle into two particles with equal sizes which, in fact, occurs without any energy barrier to be overcome, is energetically more favourable. As illustrated in the *bifurcation diagram* of Fig. 4-49, for a given volume fraction the bifurcation point is reached once the particles have coarsened to a certain mean size which depends on the surface energy and on the misfit strains. Precipitate coarsening thus commences along the lines of Ostwald-ripening (region I) until the two-phase system has reached its bifurcation point beyond which the tendency for the growth of smaller particles at the expense of larger ones ($R^0 \to 0$ within region II) increases. By transferring the results from the two-particle consideration to the multi-particle reality, a rather monodispersive particle size distribution will finally be established which is stabilized against further aging. The formation of precipitate microstructures with a fairly uniform size distribution and an increased stability towards coarsening, therefore, is more likely to be observed in concentrated alloys. The stability bifurcation *may* thus account for the experimentally observed sluggish coarsening kinetics in alloys with a large volume fraction ($f_p \geq 30\%$) of *isolated* coherently misfitting precipitates such as modulated Cu–Ni–Fe (Wagner et al., 1984), Cu–Ni–Si (Yoshida et al., 1987), or modulated Co–Cu (Miyazaki et al., 1986). The time exponent a of the coarsening rate, defined by $\bar{R} \propto t^a$, of these alloys was consistently found to be smaller than 1/3, i.e., the value expected from conventional coarsening theory on the basis of Ostwald-ripening. Furthermore, it was shown that coarsening of a ⟨100⟩ modulated structure in less-concentrated Co–Cu alloys (≤ 20 at.% Cu, $f_p \approx 20\%$) still follows the $t^{1/3}$-kinetics, whereas the coarsening rate becomes extremely small in Co–50 at.% Cu alloy ($f_p \approx 50\%$) as indicated by the small time exponent $a \ll 1/50$ (Miyazaki et al., 1986).

74

VCH Verlagsgesellschaft, 6940 Weinheim
Autor:
Material Science & Technology, Vol. 5
Hersteller: Herr Schmitt

Umbruch:
Fahnen:
K. Tritsch, Würzburg
1. Korr.

As was pointed out in Sec. 4.5.5 'mottled structures' or 'interconnected microstructures' can result from spinodal decomposition of alloys with *vanishing* coherency strains. Unlike for modulated structures, elastic interactions therefore should not stabilize the interconnected microstructure against coarsening. Nevertheless, the coarsening rate of interconnected phases is frequently found *not* to follow the $t^{1/3}$-kinetics. Experimental studies on the coarsening kinetics of interconnected phases in hard magnet materials such as Fe–Cr–Co (Zhu et al., 1986), Al–Ni–Co (Hütten and Haasen, 1986), and Fe–Cr (Brenner et al., 1984; Katano and Iizumi, 1982) instead yielded time exponents a between 1/4 and 1/10. Evidently, an adequate theoretical description of the coarsening kinetics of such a complex interconnected microstructure has to go beyond the mere modelling of diffusional interaction between two or even more isolated *spherical* particles.

4.7 Numerical Approaches Treating Nucleation, Growth, and Coarsening as Concomitant Processes

4.7.1 General Remarks on the Interpretation of Experimental Kinetic Data of Early Decomposition Stages

In this section we address our attention to decomposition studies of alloys with sufficiently high nucleation barriers ($\Delta F^*/kT \gtrsim 7$) decomposing via nucleation, growth, and coarsening. In contrast to the considerations of the preceding sections we now ask, how experimental kinetic data can be interpreted if they refer to very early decomposition stages which include *nucleation*, *growth*, and *coarsening* as concomitant rather than consecutive processes on the time scale. In attempting such interpretations one has to recall that these early decomposition stages especially are characterized by dramatic changes of supersaturation and, thus, of the driving forces for nucleation and growth processes. Furthermore, during these early stages the size distribution function evolves and is subjected to drastic alterations within rather short aging periods where nucleation, growth, and coarsening must be seen as competing and overlapping processes. Evidently these rather complicated phenomena are not properly accounted for by splitting the course of decomposition into a nucleation

VCH Verlagsgesellschaft, 6940 Weinheim
Autor:
Material Science & Technology, Vol. 5
Hersteller: Herr Schmitt

Umbruch:
Fahnen:
K. Tritsch, Würzburg
1. Korr.

regime, a growth regime, and a coarsening regime. Moreover, the kinetic theories developed for either regime (Sec. 4.5.1, 4.5.2, and 4.6, respectively) are based on idealized assumptions which are frequently not expected to be close to reality. This holds true for the classical nucleation theories of Volmer and Weber and Becker and Döring (Sec. 4.5.1). In these theories the supersaturation is assumed to be constant. This may be fulfilled – if at all – only during the *earliest* nucleation stage. Furthermore, these theories are based on artificial assumptions of the cluster size distribution in the vicinity of the critical radius (Fig. 4-24) which are not consistent with the fact that, during the nucleation process, many growing precipitates slightly larger than the critical size are formed. The theory of diffusional growth by Zener and Ham (Sec. 4.5.2) describes only the time evolution of precipitates with *uniform* size. However, towards the end of nucleation as well as at the beginning of the LSW-coarsening regime one certainly has to deal with a *polydispersed* precipitate microstructure. Thus, even if nucleation and LSW-coarsening were to be well separated on the time scale, in between these two regimes the Zener-Ham theory can not be expected to correctly predict the measured growth kinetics quantitatively. Finally, the coarsening theories of Lifshitz, Slyozow and Wagner are based on the linearized version of the Gibbs-Thomson equation (Eq. (4-46b)) and on the assumption that the supersaturation is close to zero. These restrictions also hold for the more recent theories (Sec. 4.6.3) which take into account finite precipitated volume fractions and overlapping concentration profile between precipitates.

Thus, any theory for the kinetics of precipitation which can be employed either for a more realistic interpretation of experimental data or for a prediction of the dynamic evolution of a second phase microstructure under elevated temperature service conditions, has to treat nucleation, growth, and coarsening as concomitant processes. This was accounted for in the cluster dynamic theories of Binder and coworkers (Secs. 4.5.3, 4.6.4). However, as was pointed out by these authors (Binder et al., 1978; Mirold and Binder, 1977), the theory developed yields a reasonable *qualitative* prediction of the features of experimentally observable quantities but does not attempt their *quantitative* interpretation.

A further decomposition theory treating nucleation, growth, and coarsening as concomitant processes was developed by Langer and Schwartz (LS-model; Langer and Schwartz, 1980). This theory was formulated for describing droplet formation and growth in near-critical fluids. Later on it was modified by Wendt and Haasen (1983) and further improved by Kampmann and Wagner (MLS-model; 1984) in such a way that it could be applied for the description of the kinetics of precipitate formation and growth in metastable alloys of rather high degrees of supersaturation. The MLS-model is still based on the same assumptions as the original LS-theory. In particular, the explicit form of the size distribution is not accounted for and the long-time coarsening behavior is assumed to match the LSW-results, i.e., is described by Eq. (4-62). A priori, it is not possible to foresee the influence of these assumptions on the precipitation kinetics.

Therefore, Kampmann and Wagner (KW; 1984) have devised an algorithm which accurately describes the entire course of precipitation within the framework of classical nucleation and growth theories. Accurate is meant in the sense that, unlike the LS- and the MLS-theory, no simplifying assumption enters this algorithm; in particular, in this algorithm, termed *Numerical model (N-model)*, the time evolution of the size distribution is computed without any approximations. From a comparison of the N-model with experimental data it is possible to determine some crucial precipitation parameters of the particular alloy system as well as to scrutinize the existing nucleation and

VCH Verlagsgesellschaft, 6940 Weinheim
Autor:
Material Science & Technology, Vol. 5
Umbruch:
Fahnen:
K. Trillsch, Würzburg

growth theories with respect to their applicability to decomposition reactions in real materials. Furthermore, the N-model allows an evaluation to be made of how realistic the various approximations are which enter both the LSW-theory and the MLS-model.

In this section we shall briefly introduce the MLS- and the N-model. An attempt is made to demonstrate their capability of describing the entire course of the decomposition reaction; it will also be shown how some essential parameters of the decomposing alloy such as the diffusion constant and the specific interfacial energy can be evaluated by fitting the theoretically predicted curves $\bar{R}(t)$ and $N_v(t)$ to the corresponding experimental data. Furthermore, on the grounds of the N-model, it becomes possible to examine whether certain time intervals exist during the course of a precipitation reaction in which the kinetic evolution is predicted by either the growth or the coarsening theory with sufficient accuracy.

4.7.2 Theory of Langer and Schwartz (LS-Model) and its Modification by Kampmann and Wagner (MLS-Model)

In the LS-theory it is assumed that the system contains N_{LS} droplets per unit volume of uniform size $\bar{R}_{LS}$. In order to account for coarsening, the continuous distribution function $f(R,t)$ and the number of particles of critical size, i.e., $f(R^*,t)\,dR^*$, must be known. However, in the LS-theory this is not the case. LS, therefore, introduced an apparent density $f_a(R^*,t)$ (Fig. 4-50) which is given as:

Papier

$$f_a(R^*,t) = N_{LS}\,\frac{b}{\bar{R}_{LS}} \qquad (4\text{-}67)$$

$f_a(R^*,t)$ is thus proportional to N_{LS} and inversely proportional to the width of $f(R,t)$. The constant $b = 0.317$ is chosen in such a way that for $t \to \infty$ the coarsening rate $d\bar{R}_{LS}^3/dt$ is identical to α_{LSW} (Eq. (4-62)). Unlike the LSW-theory, where $\bar{R} = R^*$, in the LS-theory only particles with $R > R^*$ are counted as belonging to $f(R,t)$, i.e.:

$$\bar{R}_{LS} = \frac{1}{N_{LS}} \int_{R^*}^{\infty} f(R,t)\,R\,dR \qquad (4\text{-}68)$$

Thus, $\bar{R}_{LS} > R^*$ in all stages of decomposition keeping $f_a(R^*,t)$ in Eq. (4-67) finite. Due to nucleation at a rate J and dissolutioning, N_{LS} changes with time according to:

$$\frac{dN_{LS}}{dt} = J - f_a(R^*,t)\,\frac{dR^*}{dt} \qquad (4\text{-}69)$$

The growth of particles having the mean size $\bar{R}_{LS}$ is given as:

$$\frac{d\bar{R}_{LS}}{dt} = r(\bar{R}_{LS}) + (\bar{R}_{LS} - R^*)\,\frac{f_a(R^*,t)}{N_{LS}}\,\frac{dR^*}{dt} + \frac{1}{N_{LS}}\,J[R^*(t)]\,(R^* + \delta R^* - \bar{R}_{LS}) \qquad (4\text{-}70)$$

The term $r(\bar{R}_{LS})$ is given by Eq. (4-44) and accounts for the growth rate of the particles in the supersaturated matrix. The second term accounts for the change of the true distribution function caused by the dissolution of $f_a(R^*,t)\,dR^*$ particles with radii between R^* and $R^* + dR^*$. The third term describes the change of $f(R,t)$ caused by the nucleation of particles which must be slightly larger than those of critical size, i.e., $R = R^* + \delta R^*$ and $\delta R^* \ll R^*$. Together with the continuity equation [1],

$$(c_p - \bar{c})\,\frac{4\pi}{3}\,\bar{R}_{LS}^3\,N_{LS} = (c_0 - \bar{c}) \qquad (4\text{-}71)$$

[1] Note that particles with $R < R^*$ are not contained in Eq. (4-71); we therefore call these particles "apparent"

and Eqs. (4-67), (4-69), and (4-70) are the rate equations which describe the *entire* course of precipitation in the LS-model. After proper scaling, these equations were numerically integrated in conjunction with steady state nucleation theory (Eq. (4-28))

The *LS-model* is based on the assumption that the equilibrium solubility of small clusters can be determined from the linearized version of the Gibbs-Thomson equation, i.e. Eq. (4-46b). This linearization, however, generally does not hold for small clusters in metallic alloys. This becomes immediately evident for the Cu–1.9 at.% Ti system isothermally aged at 350 C. At $t = 0$, R^* is 0.48 nm or only 0.13 nm depending on whether R^* is computed ($\sigma_{\alpha\beta} = 0.067$ J/m^2, see Sec. 4.7.4.4) from the non-linearized or from the linearized version of Eq. (4-46). This example clearly demonstrates that Eq. (4-46) has to be used in its *non-linearized* version, in particular for systems with large values of $\sigma_{\alpha\beta}$ and/or large supersaturations.

The *MLS-model* is based on the *non-linearized* Gibbs-Thomson equation. Thus, the growth rate in the MLS-model is obtained as:

$$\frac{dR_{LS}}{dt} = v(R_{LS}) = \frac{1}{c_p - c_\alpha^e} \frac{D}{R_{LS}} \cdot \left[\bar{c} - c_\alpha^e \exp\left\{ \frac{2\sigma_{\alpha\beta} V_m}{R_g T} \frac{1}{R_{LS}} \right\} \right] \tag{4-72}$$

In order to write the rate Eqs. (4-69) to (4-71) in a properly scaled version, we introduce the following parameters:

$$R_N = \frac{2 V_m \sigma_0}{R_g T}; \quad k_\sigma = \sigma_{\alpha\beta}/\sigma_0; \quad \xi_0 = c_0/c_\alpha^e; \quad \xi = \bar{c}/c_\alpha^e; \quad \xi_p = c_p/c_\alpha^e; \quad \varrho = \bar{R}_{LS}/R_N; \quad \varrho^* = R^*/R_N; \quad \delta\varrho^* = \delta R^*/R_N; \quad n = N_{LS} \frac{4\pi}{3} R_N^3; \quad \tau = \frac{D}{R_N^2} t; \quad \bar{J} = J \frac{dn}{dN} \frac{dt}{d\tau} \tag{4-73}$$

Apart from R_N, all parameters are dimensionless; unlike in both the original LS-model, and the study of Wendt and Haasen (1983), in the MLS-model R_N rather than the correlation length is used as scaling length. By straight forward scaling of Eqs. (4.28), (4-61), and (4-72) one obtains the scaled version of the equations of motion (4-69) and (4-70). From these, the number density n of particles is eliminated by virtue of scaled continuity equation

$$n = \frac{1}{\varrho^3} \frac{\xi_0 - \xi}{\xi_\varrho - 1} \tag{4-74}$$

One finally obtains

$$\frac{d\varrho}{d\tau} + \frac{\varrho}{3} \left[\frac{1}{\xi_0 - \xi} + \frac{b k_\sigma}{\varrho \ln \xi - k_\sigma} \frac{1}{\xi \ln \xi} \right] \frac{d\xi}{d\tau} = -\bar{J} \frac{\varrho^4}{3} \frac{\xi_p - 1}{\xi_0 - \xi} \tag{4-75a}$$

$$\frac{d\varrho}{d\tau} + \frac{b k_\sigma}{\xi (\ln \xi)^2} \frac{d\xi}{d\tau} = \frac{1}{\xi_\varrho - 1} \frac{1}{\varrho} \left[\xi - \exp\left\{ \frac{k_\sigma}{\varrho} \right\} \right] + \varrho^3 \frac{\xi_p - 1}{\xi_0 - \xi} \bar{J} \left(\frac{k_\sigma}{\ln \xi} + \delta\varrho^* - \varrho \right) \tag{4-75b}$$

Eqs. (4-75a) and (4-75b) are the basic equations of the MLS-model and are numerically integrated with $\sigma_0 = 0.1$ J/m^2; values of $\delta\varrho^*/\varrho^*(\xi_0)$ used by KW (1984) ranged from 0.05 to 0.2.

In the LS-theory only the steady state nucleation rate has been used in Eq. (4-75); in contrast, in the MLS-model, KW employed the time dependent nucleation rate J^* (Eq. (4-30)) which involves the incubation time τ or τ_w in the scaled version. The latter was evaluated from:

$$\tau_w(\xi) = \frac{1}{2} \frac{\xi_p - 1}{\xi - 1} \varrho^{*2} c_w^2 \cong \tau_{w,\min} c_w^2 \tag{4-76}$$

When deriving this equation, it was assumed that the minimum time ($\tau_{w,\min}$) for a particle to reach the critical size ϱ^* is given by Eq. (4-47). However, for subcritical nuclei c_R is considerably larger than c_α^e, and the probability for their redissolution is rather large; hence, Eq. (4-47) overestimates the growth rate significantly. This fact is counterbalanced by the introduction of the parameter c_w. For each particular alloy system, c_w is determined in such a way that after a period $\tau_{w,\min}$ the first particles become 'observable' with a reasonable number density. For all alloy systems investigated so far, c_w ranged from 1.4 to 3.5. Hence, because of the stochastic nature of cluster growth and dissolutioning, on the average it takes about two to twelve times longer for a cluster to attain a size $R > R^*$ beyond which its further growth may be evaluated in a deterministic manner on the basis of Eq. (4-47).

VCH Verlagsgesellschaft, 6940 Weinheim
Autor:
Material Science & Technology, Vol. 5
Hersteller: Herr Schmitt
Umbruch:
Fahnen:
K. Tiltsch, Würzburg
1. Korr.:

VCH Verlagsgesellschaft, 6940 Weinheim
Autor:
Material Science & Technology, Vol. 5
Hersteller: Herr Schmitt
Umbruch:
Fahnen:
K. Tiltsch, Würzburg
1. Korr.:

82

4.7.3 The Numerical Model (N-Model) of Kampmann and Wagner (KW)

Unlike the MLS-model, in the N-model the time evolution of $f(R,t)$ – or $f(\varrho,\tau)$ if we stick to the same nomenclature – is computed. For this purpose $f(\varrho,\tau)$ is subdivided into intervals $[\varrho_{j+1}, \varrho_j]$ with $|\varrho_j - \varrho_{j+1}|/\varrho_j \ll 1$ and n_j particles in the j-th interval. In contrast to the MLS-model, dissolving particles with $\varrho < \varrho^*$ are assumed to belong to the precipitating phase, i.e.,

$$n = \sum_{j=1}^{j_0} n_j \quad \text{and} \quad \bar{\varrho} = \frac{1}{n} \sum_{j=1}^{j_0} n_j \bar{\varrho}_j$$

$$\text{with} \quad \bar{\varrho}_j = \frac{1}{2}(\varrho_j + \varrho_{j+1}) \tag{4-77}$$

The continuity equation in the N-model reads then as:

$$(\xi_R - 1) \sum_{j=1}^{j_0} \bar{\varrho}_j^3 n_j = \xi_0 - \xi \tag{4-78}$$

Thus, continuous time-evolution of $f(\varrho,t)$ is split into a sequence of individual decomposition steps; these steps are to be chosen in such a manner that within each corresponding time interval $\Delta\tau_i$ the changes of all radii $\varrho_j(\tau_i)$ and of the supersaturation $\xi(\tau_i)$ remain sufficiently small. Then, both the nucleation and the growth rate can be considered as being constant during $\Delta\tau_i$ and the change of $f(\varrho,\tau)$ and of ξ can be reliably computed. The N-model of KW contains some algorithms by which a rather high accuracy of the numerical calculation is ensured; it amounts to $\approx 0.5\%$ in the case of the growth rate of ϱ.

VCH Verlagsgesellschaft, 6940 Weinheim
Autor:
Material Science & Technology, Vol. 5
Herstellerin: Herr Schmitt
Umbruch:
Fahnen:
K. Trillsch, Würzburg
1. Korr.:

83

4.7.4 Decomposition of a Homogeneous Solid Solution

4.7.4.1 General Course of Decomposition

KW have discussed the decomposition reaction of an ideally quenched alloy with $c_s^e = 0.22$ at.%, $f = 0.20$ at.%, $c_0 = 1.9$ at.% and $\sigma_{\alpha\beta} = 0.067$ J/m^2. Just on the basis of those input data the decomposition reaction can be calculated within the framework of the MLS- and N-model. Fig. 4-51 reveals the predictions from both the MLS (full lines) and the N-model (discrete symbols) for the time evolution of the radii $\bar{\varrho}(\tau)$ and $\varrho^*(\tau)$, the number density $n(\tau)$, the supersaturation $\xi(\tau)$, and the nucleation rate $\bar{J}(\tau)$. The chosen values of $\xi_0 = 8.7$, c_s^e, σ and D correspond to those for Cu–1.9 at.% Ti aged at 350 °C (see Secs. 4.7.4.3 and 4.7.4.4). Surprisingly, both models yield qualitatively similar results. During the early nucleation period ($\tau \lesssim 1$) both $\bar{J}$ and n increase, whereas ξ and, hence, ϱ^* remain roughly constant. At this stage, the N-model yields the size distribution function $f(\varrho,t)$ to be rather narrow (Fig. 4-52). Since c_R is still close to $\bar{c} \approx c_0$, the growth rate of nucleated precipitates is also close to zero, i.e., $\bar{\varrho}$ remains about constant. After $\tau \gtrsim 1$, those precipitates nucleated first become considerably larger than ϱ^* and $f(\varrho,\tau)$ becomes much broader. This is the beginning of the growth period is characterized by (i) the largest growth rate ever observed during the course of precipitation; (ii) a ratio $\bar{\varrho}/\varrho^*$ which becomes significantly larger than 1; (iii) the maximum number density ($n_{max}, N_{v,max}$) of particles which remains about constant; (iv) a stronger decrease of ξ; and, consequently, (v) a decrease of $\bar{J}$ from its maximum value; in this particular case, $\bar{J}$ never reaches its steady state value. At the end of the growth regime ($\tau \approx 15$) the supersaturation has dropped significantly and the growth rate becomes small. This effect causes ϱ^* to converge towards $\bar{\varrho}$ as well as to make $dn/d\tau < 0$ (Eq. (4-69)). During the subsequent transition period ($\tau \approx 15$), the growth rate of $\bar{\varrho}$ is primarily controlled by the dissolution of particles with $\varrho < \varrho^*$ and only to a lesser extent by the uptake of solute atoms from the matrix, the supersaturation of which is still about 20%. During the transition period, the true distribution function $f(\varrho,t)$ continuously approaches the one predicted by LSW (Fig. 4-52). At this

VCH Verlagsgesellschaft, 6940 Weinheim
Autor:
Material Science & Technology, Vol. 5
Herstellerin: Herr Schmitt
Umbruch:
Fahnen:
K. Trillsch, Würzburg
1. Korr.:

stage, however, f_{LSW} (Eq. (4-64)) is still a rather poor approximation for $f(\varrho, t)$. This simply reflects the influence of the linearization of the Gibbs-Thomson equation (Eq. (4-46b)) on which the LSW-theory is based. For $\tau \to \infty$, $d\bar{\varrho}^3/d\tau$ approaches asymptotically a constant value, i.e., the reaction is within the asymptotic limit of *coarsening* where the supersaturation is almost zero. At this stage $f(\varrho, \tau)$ is well approximated by f_{LSW} with only minor deviations for small particle radii.

4.7.4.2 Comparison Between MLS- and N-model

The precipitation reaction starts with an identifical nucleation rate and identical particle sizes in both the MLS- and the N-model. Therefore, both models are expected to yield identical results which, in fact, is observed in Fig. 4-51. During the later growth period dissolution of particles with $\varrho < \varrho^*$ commences. At this stage, the MLS-model only counts particles with $\varrho > \varrho^*$ as belonging to the second phase (Eq. (4-68)), and, furthermore, assumes $f_a(\varrho = \varrho^*)$ to be proportional to $1/(\bar{\varrho} - \varrho^*)$ (Eq. (4-67)). At this stage, this is a rather poor approximation since the N-model yields a steep slope for $f(\varrho \to \varrho^*, \tau)$ with a rather small density $n(\varrho = \varrho^*)$. These facts make the MLS-model predict considerably larger rate constants for the decrease of the particle number density and, hence, for the growth of $\bar{\varrho}$ at the end of the growth period ($\tau \approx 15$).

According to the particular choice of b (Eq. (4-67)), the coarsening rate of the MLS-model approaches asymptotically the value α_{LSW} (Eq. (4-62a)) from the LSW-theory. In this asymptotic limit the mean radii from both models and, hence, their coarsening rates become identical. At this stage the N-model yields $\bar{\varrho} \cong \varrho^*$ as predicted by LSW, whereas the MLS-model yields $\bar{\varrho} - \varrho^* \approx$ const., i.e., $\bar{R}_{LS} > R^*$, as required by Eq. (4-68).

One can conclude that the MLS-model, which requires much less computing time than does the N-model, provides a good survey of the general course of precipitation. However, due to the simplifying assumptions made, it does not predict the precipitation kinetics with the same accuracy as does the N-model. This is particularly evident for those precipitation stages where the shape of $f(\varrho, \tau)$ is extreme, as, for instance, during the later growth stages in the example discussed above.

4.7.4.3 The Appearance and Experimental Identification of the Growth and Coarsening Stages

In the following, the results from the MLS- and the N-model are compared with experimental data obtained from a FIM-atomprobe study of early stage precipitation in Cu–1.9 at.% Ti at 350 °C (von Alvensleben and Wagner, 1984).

Fig. 4-53 shows the time evolution of R^* and of $\bar{R}$ in physical units. Again these experimental data points are well described by the N-model. Fig. 4-53 also reveals that the experimental data cover neither the early nucleation period nor the growth regime, but rather start ($t = 2.5$ min) at the end of the latter region. From Fig. 4-54a, where $\bar{R}^3$ is plotted as a function of t, it is recognized that during the period $t \approx 0.7$ min to 1.2 min, $\bar{R}^3$ varies linearily with t as suggested by Eq. (4-41). Since this time period extends only over 0.5 min, KW have concluded that for Cu–1.9 at.% Ti the time window is too short for discovering the $\bar{R} \sim t^{1/3}$ kinetics experimentally; in fact, the same holds true for many other alloy systems analyzed by KW using the N-model. Furthermore, from Fig. 4-54a the slope of the straight line has been evaluated to be 0.88 nm^3/min whereas the cor-

responding growth rate from Eq. (4-47) is computed ($c_\alpha^e = 0.22$ at.%, $c_\beta = 20$ at.%, $D = 2.5 \times 10^{-15}$ cm^2/sec) to be 2.5 nm^2/min. This result clearly demonstrates that no growth regime exists which is adequately accounted for by Eq. (4-47). In other words, the idealizations made in the derivation of Eq. (4-47) do not approximate the true situation in Cu–1.9 at.% Ti. However, if $\bar{c}(t)$ and c_R in Eq. (4-43) are replaced by their mean values, respectively, during the period for which $\bar{R} \sim t^{1/2}$ holds, then Eq. (4-41) with $\lambda_t = \sqrt{k^*}$ yields a value for the growth rate (0.104 nm^2/min) which is only 16% larger than the true value.

In Fig. 4-54b the rate constant $d\bar{R}^3/dt$ for coarsening is plotted versus t. It is evident that for Cu–1.9 at.% Ti the rate constant $\alpha_{LSW} = 1.2 \cdot 10^{-24}$ cm^3/sec from the LSW-theory (Eq. (4-62a)) is only reached for aging times beyond $\approx 10^4$ min! At this stage $\bar{R}$ has already grown to ≈ 6.4 nm. From this result, which reflects the influence of the linearization of Eq. (4-46), KW inferred that the LSW-theory predicts the correct coarsening rate once

$$\bar{R} \geq 13 \frac{V_m \sigma_{\alpha\beta}}{R_g T}, \quad \bar{R} \geq 13 \frac{V_m \sigma_{\alpha\beta}}{R_g T} \qquad (4\text{-}79)$$

If this relation holds, $f(R,t)$ is almost identical to f_{LSW} (Fig. 4-52) and $\bar{c}/c_e \approx 1$.

According to the results from the N-model, during the early coarsening stages the precipitation kinetics deviate significantly from those predicted by the LSW-theory (e.g. Fig. 4-54b). Thus the widely used LSW-analyses resulting in a determination of D and $\sigma_{\alpha\beta}$ on the basis of Eq. (4-62) and Eq. (4-63) should not be applied to early coarsening stages during which the relation does not hold.

4.7.4.4 Extraction of the Interfacial Energy and the Diffusion Constant from Experimental Data

KW determined $\sigma_{\alpha\beta}$ and D separately by fitting $\bar{R}(t)$ and $N_v(t)$ as obtained from the N-model to the corresponding experimental data. In Fig. 4-55 the variation of N_v and J^* with aging time as computed with the N- and the MLS-model are shown together with the corresponding experimental data. The peak number density $N_{v,max}$ of particles in a precipitation reaction is essentially governed by the value of ΔF^* via the nucleation rate Eq. (4-28). Since $\Delta F^* \sim \sigma_{\alpha\beta}^3$ (Eq. (4-20)), $N_{v,max}$ depends sensitively on the value of the interfacial energy $\sigma_{\alpha\beta}$. The very strong dependence of $N_{v,max}$ on $\sigma_{\alpha\beta}$ is clearly revealed by Fig. 4-55 showing a good fit of $N_v(t)$ for $\sigma_{\alpha\beta} = 0.067$ J/m^2 and only poor agreement for $\sigma_{\alpha\beta} = 0.071$ J/m^2. On the other hand, a variation of D manifests itself in a parallel shift of the entire curve on the time scale. Thus, a fit of $\bar{R}(t)$ and of $N_v(t)$ as obtained from the N-model, to the experimental curves allows both $\sigma_{\alpha\beta}$ and D to be determined quite accurately.

From a variety of different two-phase alloys, the available kinetic data have been interpreted in terms of the N-model. Table 4-3 presents the interfacial energies $\sigma_{\alpha\beta}$ together with the width of the (coherent miscibility gap for each given alloy. It is evident that there is a pronounced correlation between $\sigma_{\alpha\beta}$ and the compositional width, i.e., the broader the gap, the larger is $\sigma_{\alpha\beta}$. This is consistent with various theoretical predictions on the interfacial energy (cf. Lee and Aaronson, 1980, for a comprehensive discussion of this aspect).

4.7.5 Decomposition Kinetics in Alloys Pre-Decomposed During Quenching

The versatility of the N-model is further illustrated by its application to predict the precipitation kinetics in alloys which experienced some phase separation already during quenching. This is exemplified for Cu–2.9 at.% Ti, the decomposition reaction which was recently studied by Kampmann et al. (1987) by means of SANS-techniques. They found that the cooling rate of their specimen was not sufficient to suppress the formation of Cu_4Ti-precipitates during the quench, in fact, as is shown in Fig. 4-56, the solute concentration decreased from $c_0 = 2.9$ at.% to 2.2 at.% Ti

VCH Verlagsgesellschaft, 6940 Weinheim
Autor:
Material Science & Technology, Vol. 5
Herausgeber: Herr Schmitt
Umbruch:
Fahnen:
K. Trittsch, Würzburg
1. Korr.:

clusters and the growth of existing ones. After aging for ≈ 100 min/350 °C the metastable β'-solvus line is nearly reached at $c_i^{\beta'} \approx 0.22$ at.% Ti (cf. Sec. 4.2.1).

The experimentally determined kinetic behavior of the precipitate number density, of their mean radius, and of the supersaturation are displayed in Fig. 4-57a–c and compared with the predictions of the N-model. For the computations, they took into account the result from the SANS evaluation which yielded the homogenized sample to already contain $\approx 2 \cdot 10^{25}$ clusters/m^3 with $\bar{R} \approx 0.7$ nm. These could immediately grow by further depleting the matrix from solute atoms. Moreover, at $t = 0$ the supersaturation was still large enough for nucleating new clusters with smaller radii at a nucleation rate J^* (Fig. 4-57a). Thus, during the first minutes of aging the cluster number density increased. At this stage, the alloy contained a sort of bimodal cluster distribution: the larger ones formed at a smaller supersaturation during quenching, and the smaller ones resulting from nucleation at 350 °C. Due to both nucleation of new clusters and growth of pre-existing ones, the supersaturation and, hence, the nucleation rate decreased rapidly; after aging for ≈ 3 min nucleation is virtually terminated. After ≈ 10 min the critical radius R^*, which is correlated with the momentary supersaturation, reached the mean value $\bar{R}$ of the global size distribution. At this instant, R^* has grown beyond the mean radius of the smaller freshly nucleated clusters; these now redissolve leading to a further decrease of N_v. Now the size distribution is again governed by the larger precipitates which formed during quenching. After about 500 min, N_v decreases with t as expected from the LSW theory.

With regard to the accuracy of both the SANS experiment and, in particular, the SANS data evaluation, the agreement between the experimental kinetic data and those from the N-model is rather good for an interfacial energy $\sigma_{\alpha\beta} = 0.067$ J/m^2. This value is identical to that which was determined for the less concentrated Cu-1.9 at.% Ti alloy (Sec. 4.7.4.4). In the early stages ($t \leqq 10$ min) the experimental $\bar{R}$ is considerably larger than the theoretical one. This simply reflects the fact that the scattering power of a particle is biased with R^6; hence, for $t \leqq 10$ min, essentially the radius of only the larger particles within the bimodal distribution was determined. The diffusion coefficient ($D = 3 \cdot 10^{-16}$ cm^2/sec) was found to be a factor of ≈ 10 smaller

VCH Verlagsgesellschaft, 6940 Weinheim
Autor:
Material Science & Technology, Vol. 5
Hersteller: Herr Schmitt
Umbruch:
Fahnen:
K. Tritsch, Würzburg
1. Korr.:

flects the concentration dependence of D, or whether it was caused by differences in the homogenization temperatures of the two alloys (Cu–2.9 at.% Ti: $T_H = 780$ °C, Cu–1.9 at.% Ti: $T_H = 910$ °C).

4.7.6 Influence of the Loss of Particle Coherency on the Precipitation Kinetics

In many two-phase systems the particles loose coherency once they have grown beyond a certain size R_I (Sec. 4.2.1). The associated increase of the interfacial energy and decrease of the solubility limit (cf. Fig. 4-1) leads to an enhanced driving force and, hence, to accelerated kinetics for further coarsening of the incoherent microstructure with respect to the coherent one. This effect can also be accounted for by the Numerical Model. This is shown in Fig. 4-58 for Fe–1.38 at.% Cu aged at 500 °C. As inferred from CTEM the Cu-rich particles transform at $R_T \approx 2.8$ nm from the metastable b.c.c. structure into the f.c.c. equilibrium structure. The associated loss of coherency occurs at particle number densities well beyond the maximum number density $N_{v,max}$ (Fig. 4-58). Thus, following the procedure outlined in Sec. 4.7.4.4, the coherent interfacial energy could be determined by fitting the N-model to the experimental (SANS) kinetic data of the still coherent system. The value $\sigma_{\alpha\beta} \approx 0.27$ J/m^2 obtained is considerably smaller than the corresponding value $\sigma_{\alpha\beta}^{inc} \approx 0.50$ J/m^2 which was derived from a thermodynamical analysis of the Fe–Cu system (Kampmann and Wagner, 1986). As is shown in Fig. 4-58, the loss of coherency, in fact, leads to a momentary acceleration of the growth kinetics. It is, however, not sufficient to bridge the discrepancy between the experimental kinetic data and the theoretically predicted one displayed in Fig. 4-58. As the predicted kinetics are much more sluggish than the experimentaly determined ones, one might speculate that neglecting particle interaction accounts for the observed discrepancy. Inspection of Fig. 4-44, however, reveals that a consideration of finite volume effects in the Fe–1.38 at.% Cu system with $f_p \approx 1\%$ would increase the coarsening rate only by less than a factor 1.3 whereas a factor of ≈ 10 is required to match the results from the N-model and the SANS experiments at the later stages of precipitation. At present, it can not be decided whether the various theories dealing with finite volume effects (Sec. 4.6.3) are still insufficient or whether some heterogenous precipitation at lattice defects accounts for the observed discrep-

VCH Verlagsgesellschaft, 6940 Weinheim
Autor:
Material Science & Technology, Vol. 5
Umbruch:
Fahnen:
K. Tritsch, Würzburg

At a first glance, the experimental kinetic data for $\bar{R}(t)$ and $N_v(t)$ in Fig. 4-58 might be seen as being amenable to a LSW analysis in terms of Eq. (4-62). Analyses of the SANS data for $t \gg 10^3$ min, however, yielded the width of the particle size distribution to be much broader (standard deviation: $\sigma \approx 0.31$) than expected from the LSW theory or its modifications ($\sigma \approx 0.23$). Furthermore, the measured supersaturation was still far from being close to zero. Hence, the conditions for a LSW analysis of the experimental data are not at all fulfilled.

4.8 Self-Similarity, Dynamical Scaling and Power-Law Approximations

4.4.1 Dynamical Scaling

According to the LSW-theory and its extensions to finite volume fractions (Sec. 4.6) the distribution of relative particle sizes $R/\bar{R}$ evolves during extended aging ($t \to \infty$) towards an asymptotic, time-invariant form (Eq. (4-64)), the particular shape of which depends on the precipitated volume fraction (Fig. 4-45). The final time-invariance of $f(R/\bar{R})$ reflects the fact that once the precipitated volume fraction has reached its equilibrium value, consecutive configurations of the precipitate microstructure are geometrically similar in a statistical sense, i.e., all consecutive configurations are statistically uniform on scale which is considerably larger than some characteristic length such as the mean particle size $\bar{R}$ or the mean center-to-center distance $\bar{L} = N_v^{-1/3}$. The *self-similarity* of the microstructural evolution has found its expression in the *dynamical scaling* of the structure function $S(\varkappa, t)$ (Binder and Stauffer, 1974; Binder et al., 1978). Furukawa (1981) proposed $S(\varkappa, t)$ to satisfy after some transient time t_0 a scaling law of the form:

$$S(\varkappa, t) = I^3(t)\, \tilde{F}(\varkappa \cdot l(t)) ; \; t \geqq t_0 \qquad (4\text{-}80)$$

$\tilde{F}(\varkappa \cdot l(t)) \equiv \tilde{F}(x)$ is the time-independent scaling function. As the scaling parameter, $l(t)$ denotes some characteristic length and contains exclusively the time dependence of $S(\varkappa, t)$.

Strong theoretical support for the validity of the scaling hypothesis, Eq. (4-80), during the later stages of decmposition was first provided by Monte Carlo simulations of the time evolution of binary model alloys (Sec. 4.5.6). From these studies it was concluded that there is a small though systematic dependence of $\tilde{F}(x)$ on the initial supersaturation, at least for small x (Lebowitz et al., 1982); for large values of x, the scaling function appears to be universal in that it becomes independent of temperature and precipitated volume fraction, and even of the investigated material (Fratzl et al., 1983). By analogy to the Porod-law of small-angle scattering, in this regime $\tilde{F}(x)$ decays in proportion to x^{-4}.

VCH Verlagsgesellschaft, 6940 Weinheim
Autor:
Material Science & Technology, Vol. 5
Hersteller: Herr Schmitt
Umbruch:
Fahnen:
K. Trittsch, Würzburg
1. Korr.:

In experiments which are designed to test the validity of the scaling behavior, $l(t)$ is commonly related to either the Guinier-radius, the mean particle radius or to either $\varkappa_m^{-1}(t)$ or $\varkappa_1^{-1}(t)$ of $\varkappa_m$ and $S(\varkappa, t)$, respectively. The scaling function $\tilde{F}(x)$ is then simply obtained, for instance, by plotting $\varkappa_m^3 \cdot S(\varkappa, t)$ versus $\varkappa/\varkappa_m$. If scaling holds, $\tilde{F}(\varkappa/\varkappa_m)$ is time-independent[4]. After some initial transient time this, in fact, was observed in the glass systems B_2O_3–PbO Al_2O_3 (Craievich et al., 1981, 1986) and in several binary alloys such as Mn-Cu (Fig. 4-59), Al-Zn (e.g. Simon et al., 1984; Hoyt and de Fontaine, 1989) or Ni-Si (Polat et al., 1989). Dynamical scaling behavior was also found in some ternary alloys such as AlZnMg (Blaschko and Fratzl, 1983). For CuNiFe which was studied by means of anomalous SAXS (Lyon and Simon, 1987), the scaling behavior is found to be obeyed only by the partial structure functions indicating that this system does not behave like a pseudo-binary system. For Fe-Cr the results are controversial. In contrast to Katano and Iizumi (1984) and Furusaka et al. (1986), La Salle and Schwartz reported that dynamical scaling do *not* hold. The decomposition kinetics in Fe-Cr at about 500 °C are fairly sluggish and it may well be that even after the longest chosen aging time (100 h) the system had not yet reached the scaling region where the microstructure displays self-similarity.

4 In order to test whether experimental data satisfy the scaling law, Fratzl et al. (1983) have proposed a direct method by which the evaluation of R_G, $\bar{R}$, $\varkappa_m$, or $\varkappa_1$ can be avoided and by means of which $\tilde{F}(x)$ can be determined graphically.

VCH Verlagsgesellschaft, 6940 Weinheim
Autor:
Material Science & Technology, Vol. 5
Hersteller: Herr Schmitt
Umbruch:
Fahnen:
K. Trittsch, Würzburg
1. Korr.:

In principle, the structure function $S(\varkappa, t)$ contains all information on the various structural parameters of a decomposing solid such as $f(R, t)$, $N_v(t)$, $\bar{R}(t)$, morphology, etc. which, for instance, may control its mechanical properties. In practice, however, commonly only $\bar{R}$ and N_v and neither $f(R, t)$ nor the morphology can be extracted from experimental data. This stems mainly from a lack of knowledge of the interparticle interference function which contains the spatial correlations of the precipitate microstructure and which manifests itself in the appearance of a maximum in the $S(\varkappa, t)$-curves of less-diluted systems. Furthermore, both the limited range of $\varkappa$ over which $S(\varkappa, t)$ can be measured and the large background in conventional small-angle scattering experiments often render the quantitative extraction of information on the precipitate microstructure rather difficult.

From the practical point of view, scaling analyses are sometimes seen to allow *all* information contained in $S(\varkappa, t)$ to be deciphered. Provided the explicit form of $\tilde{F}(x)$ could be predicted on grounds of a first-principle theory, it could be compared with experimental data and employed for a comparison of $S(\varkappa, t)$-curves taken from different materials. Up to now, however, this is not yet feasible. For this reason, various *phenomenological theories* for $\tilde{F}(x)$ have been conceived (e.g. Furukawa, 1981; Hennion et al., 1982) amongst which the model of Rikvold and Gunton (1982) may be regarded as the one which is most convenient for a comparison with experimental data as it contains the precipitated volume fraction as the only parameter. This model assumes the two-phase microstructure to consist of a 'gas' of spherical second phase particles (with an identical scattering form factor) each of which is surrounded by a zone depleted from solute atoms. With simple approximations on the probability distribution for pairs of particles with certain interparticle spacings, the explicit analytical form for $\tilde{F}(x)$ was derived. However, due to the various assumptions invoked, the Rikvold-Gunton model is restricted to smaller precipitated volume fractions. In spite of its simplicity, fair agreement was reported between the theoretical $\tilde{F}(x)$ and the scaling functions obtained from computer simulations and from scaling analyses of $S(\varkappa, t)$-curves taken from decomposed Al–Zn and Al–Ag–Zn alloys (Simon et al., 1984). In contrast, in a more recent study of Al–Zn (Forouhi and de Fontaine, 1987) and of Ni–Si (Chen et al., 1988) the predicted $\tilde{F}(x)$ was found to be much broader than the experimental ones; scaling analyses for borate glasses also could not verify the theoretically predicted form of $\tilde{F}(x)$ (Craievich et al., 1986). This may stem from the inadequate assumptions on the chosen probability distribution in which long-range correlations are neglected and/or from precipitate morphologies deviating from spheres, e.g. platelets in Al–Zn.

As a concluding remark to this section it is probably fair to state that scaling analyses currently can neither furnish the practical metallurgist with more information on the precipitate microstructure nor on its dynamic evolution than has been possible by conventional analyses of $S(\varkappa, t)$-curves prior to the emergence of the scaling hypotheses. It is felt that precise information on the size distribution, the morphology, and the spatial arrangement of precipitates in a two-phase microstructure becomes more readily available from studies employing direct imaging techniques, e.g. CTEM or AFIM, in particular, as dynamical scaling only holds in the later stages of aging where the precipitate microstructure, in general, can be easily imaged and resolved by these techniques. Furthermore, once dynamical scaling is satisfied, the system is close to the asymptotic limit where the LSW-theory or its extensions may be applied for a prediction of its dynamic evolution during further aging.

VCH Verlagsgesellschaft, 6940 Weinheim
Autor:
Material Science & Technology, Vol. 5
Herstellen: Herr Schmitt
Umbruch:
Fahnen:
K. Tritsch, Würzburg
1. Korr.:

VCH Verlagsgesellschaft, 6940 Weinheim
Autor:
Material Science & Technology, Vol. 5
Umbruch:
Fahnen:
K. Tritsch, Würzburg

4.8.2 Power-Law Approximations

So far no explicit assumption has been made about the time dependence of the chosen characteristic length, e.g. $\varkappa_m^{-1}(t)$, entering the scaling law Eq. (4-80). As the self-similarity of a precipitate microstructure and, hence, the scaling law is implicitely contained in the LSW-theory of coarsening (cf. Eq. (4-64)), the region of validity of dynamical scaling coincides with the LSW-regime of coarsening. $\varkappa_m^{-1}$ is thus expected to show the simple power-law behavior,

$$\varkappa_m^{-1}(t) \sim t^a \tag{4-81}$$

with $a = 1/3$. Accordingly, if scaling holds, the maximum of the structure function must evolve in time as

$$S_m(t) \sim t^b \tag{4-82}$$

with $b = 3a$ (Eq. (4-80)). Such a power-law behavior was frequently corroborated by scattering experiments on materials which were aged in the scaling region, and also by computer simulations (e.g. Lebowitz et al., 1982) which indicated that scaling would hold.

The more recent theoretical developments on the kinetics of phase separation have predicted various other values for the exponent a. On the basis of their cluster-diffusion-coagulation model (Sec. 4.6.4), for *intermediate times* Binder and coworkers predict $a = 1/6$ and $a = 1/5$ or $1/4$ for low and intermediate temperatures, respectively (Binder and Stauffer, 1974; Binder, 1977; Binder et al., 1978). As is shown in Fig. 4-31 b, approximation of $S_m(t)$, which displays some curvature, by a power-law (Eq. (4-82)) yields $b = 0.7$ rather than 0.48 as implied by scaling. The LBM-theory of spinodal decomposition which accounts for some coarsening at *earlier* stages (Sec. 4.5.4) yields $a = 0.21$. As outlined in Sec. 4.5.6, these values agree quite well with the corresponding ones ($a = 0.16$ to 0.25 and $b = 0.41$ to 0.71, depending on the supersaturation and 'aging temperature') obtained from fitting power-laws to the corresponding data from computer simulations.

Inspired by the theoretical predictions, many scattering experiments on alloys were interpreted in terms of power-law approximations. Frequently the existence of two well-defined kinetic regimes with distinct values of a has been reported (e.g. Fig.

CH Verlagsgesellschaft, 6940 Weinheim
Autor:
Material Science & Technology, Vol. 5
Herstellerin: Herr Schmitt
Umbruch:
Fahnen:
K. Tritsch, Würzburg
1. Korr.:

a and b are found close to the values 1/3 and 1 as predicted by the LSW theory. Sometimes this has been taken as evidence (e.g. Katano and Iizumi, 1984) for the first regime to be dominated by the cluster-diffusion-coagulation mechanism (Sec. 4.6.4), whereas in the second one the evolution proceeds according to the LSW mechanism via the evaporation and condensation of single solute atoms.

However the interpretation of $S_m(t)$ and $\varkappa_m(t)$ in terms of two distinct kinetic regimes, each of which is well described by a power-law, seems rather debatable. A closer examination of the $S_m(t)$ and $\varkappa_m$ curves (e.g. Fig. 4-32 b) always reveals some curvature prior to reaching the scaling region. This clearly shows that the exponents a and b are time-dependent; thus, apart from the LSW-regime, a power-law approximation must be seen as a rather poor description for the dynamic evolution of a decomposing solid and commonly does not disclose the specific growth mechanism dominating at a certain aging regime. This becomes particularly evident by employing the Numerical Model (Sec. 4.7.3) for a derivation of the exponent $a(t) = \partial \log \bar{R} / \partial \log t$. As the N-model comprises nucleation, growth, and coarsening as concomitant processes on the basis of just *one* growth mechanism – single-atom evaporation or condensation in the LSW sense – a plot of $a(t)$ versus t allows a closer examination on the validity of power-law approximations at any instant to be made. This is shown in Fig. 4-60 for Cu –1.9 at.% Ti, the experimental kinetic data of which are well described by the N-model (cf. Fig. 4-53). Towards the end of the nucleation regime, $a(t)$ increases sharply from ≈ 0.15 to its maximum value $a = 0.5$ which is indicative of a diffusion-controlled growth of the particles. The duration of the growth regime where $\bar{R}$ evolves according to the parabolic power-law $\bar{R} \sim t^{1/2}$ is rather short for this alloy (cf. Sec. 7.4.3). At the end of the growth regime where the particle number density has reached its maximum value (Fig. 4-55), $a(t)$ drops within about 250 s to

CH Verlagsgesellschaft, 6940 Weinheim
Autor:
Material Science & Technology, Vol. 5
Herstellerin: Herr Schmitt
Umbruch:
Fahnen:
K. Tritsch, Würzburg
1. Korr.:

a value of less than 0.1. In the subsequent transition regime at intermediate times, $a(t)$ increases continuously and approaches only slowly the LSW-coarsening regime where dynamical scaling holds. Evidently, there is no time regime between the appearance of the growth regime and the LSW-region where power-law behavior is observed. On the other hand, it may be inferred from Fig. 4-60 that the kinetic evolution of $\bar{R}$ during intermediate aging stages might be artificially interpreted in terms of power-laws if the time window covered by the experiment was too short; in this case any exponent between 0.15 and 0.33 may be derived. Thus, if the time window for the kinetic experiment is not properly chosen, $a \approx 0.2$ may be obtained though without the cluster-diffusion-coagulation mechanism being operative. As has been pointed out in Sec. 7.4.3, with increasing supersaturation the growth regime with $\bar{R} \propto t^{1/2}$ disappears completely and $a(t)$ takes values only between zero and 1/3. Furthermore, the transition period where $a < 1/3$ becomes shorter. In this case, LSW-coarsening and dynamical scaling are observed after rather short aging times. This illustrated in Fig. 4-61 for Cu–2.9 at.% Ti which already satisfies dynamical scaling after aging for ≈ 250 min at 350 °C whereas for the less concentrated Cu–1.9 at.% Ti alloy scaling only holds after $\approx 5 \cdot 10^4$ min.

4.9 Acknowledgements

The authors would like to thank Prof. R. Bormann and Dr. H. Mertins for their critical comments on this chapter and Mrs. Ch. Körten, E. Schröder, and H. Schütt for their kind endurance and assistance in preparing the manuscript.

4.10 References

Aalders, C., Van Dijk, S., Radelaar, S. (1984), in: *Decomposition of Alloys: The early stages*: Haasen, P., Gerold, V., Wagner, R., Ashby, M.F. (Eds.). Oxford: Pergamon Press, pp. 149–155.
Aaron, H.B., Fainstain, D., Kotler, G.R. (1970), *J. Appl. Phys. 41*, 4404.
Aaronson, H.I., Russell, K.C. (1982), in: *Solid-State Phase Transformations*: Aaronson, H.I., Laughlin, D.E., Sekerka, R.F., Wayman, C.M. (Eds.). Warrendale: Met. Soc. AIME, pp. 371–399.
Aaronson, H.I., Kinsman, K.R., Russell, K.C. (1970a), *Scr. Metall. 4*, 101.
Aaronson, H.I., Laird, C., Kinsman, K.R. (1970b), in: *Phase Transformations*: Aaronson, H.I. (Ed.). Metals Park, Ohio: Am. Soc. of Metals, pp. 313–396.
Acuna, R., Craievich, A.F. (1979), *J. Non-Cryst. Solids 34*, 13.
Agarwal, S.C., Herman, H. (1973), in: *Phase Transitions and Their Application in Materials Science*: Henisch, H.K., Roy, R. (Eds.). New York: Pergamon, pp. 207–222.
Ardell, A.J. (1967), *Acta Metall. 15*, 1772.
Ardell, A.J. (1968), *Acta Metall. 16*, 511.
Ardell, A.J. (1970), *Met. Trans. 1*, 525.
Ardell, A.J. (1972), *Acta Metall. 20*, 61.
Ardell, A.J., Nicholson, R.B. (1966), *Acta Metall. 14*, 1793.
Ardell, A.J., Nicholson, R.B., Eshelby, J.D. (1966), *Acta Metall. 14*, 1295.
Auger, P., Danoix, F., Menand, A., Bonnet, S., Bourgoin, J., Guttmann, M. (1989), in: *Proc. Intl. Workshop Intermediate Temperature Embrittlement Processes in Duplex Stainless Steels*. Oxford: In press.
Bartel, T.L., Rundman, K.B. (1975), *Metall. Trans. 6A*, 1887.
Bates, F.S., Wiltzius, P. (1989), *J. Chem. Phys. 91*, 3258.
Becker, R., Döring, W. (1935), *Ann. Phys. 24*, 719.
Beddoe, R., Haasen, P., Kostorz, G. (1984), in: *Decomposition of Alloys: the early stages*: Haasen, P., Gerold, V., Wagner, R., Ashby, M.F. (Eds.). Oxford: Pergamon Press, pp. 233–238.
Biehl, K.-E., Wagner, R. (1982), in: *Solid–Solid Phase Transformations*: Aaronson, H.I., Laughlin, D.E., Sekerka, R.F., Wayman, C.M. (Eds.). Warrendale: The Metallurgical Society of AIME, pp. 185–189.
Binder, K. (1977), *Phys. Rev. B15*, 4425.
Binder, K. (1980), *J. Phys. (Paris) C4*, 51.
Binder, K. (1983), *J. Chem. Phys. 79*, 6387.
Binder, K. (1984), *Phys. Rev. A29*, 341.
Binder, K., Heermann, D.W. (1985), in: *Scaling Phenomena in Disordered Systems*: Pynn, R., Skjeltorp, T. (Eds.). New York: Plenum Press, pp. 207–230.
Binder, K., Stauffer, D. (1974), *Phys. Rev. Lett. 33*, 1006.
Binder, K., Stauffer, D. (1976), *Advan. Phys. 25*, 343.
Binder, K., Billotet, C., Mirold, P. (1978), *Z. Physik B30*, 183–195.
Binder, K., Kalos, M.H., Lebowitz, J.L., Marro, J. (1979), *Colloid Interface Sci. 10*, 173.
Blaschko, O., Fratzl, P. (1983), *Phys. Rev. Lett. 51*, 288.
Blaschko, O., Ernst, G., Fratzl, P., Auger, P. (1982), *Acta Metall. 30*, 547.
Bonfiglioli, A.F., Gunner, A. (1966), *Acta Metall. 14*, 1213.
Bouchard, M., Thomas, G. (1975), *Acta Metall. 23*, 1485.
Bouchon, A., Bostel, A., Blavette, D. (1990), in: Proc. Int. Field Emission Symp. Smith, G.D.W., Miller, M.K. (Eds.). *J. Phys. (Paris)*, in press.
Bradsford, A.D., Wynblatt, P. (1979), *Acta Metall. 27*, 489.

VCH Verlagsgesellschaft, 6940 Weinheim
Autor:
Material Science & Technology, Vol. 5
Umbruch:
Fahnen:
K. Trilsch, Würzburg

Brenner, S.S., Camus, P.P., Miller, M.K., Soffa, W.A. (1984), *Acta Metall. 32*, 1217.
Cahn, J.W. (1962), *Acta Metall. 10*, 179, 907.
Cahn, J.W. (1965), *J. Chem. 42*, 93.
Cahn, J.W. (1966), *Trans. AIME 242*, 166.
Cahn, J.W., Charles, R.J. (1965), *Physics and Chemistry of Glasses 6*, 181.
Cahn, J.W., Hilliard, J.E. (1958), *J. Chem. Phys. 28*, 258.
Cahn, J.W., Hilliard, J.E. (1959a), *J. Chem. Phys. 31*, 539.
Cahn, J.W., Hilliard, J.E. (1959b), *J. Chem. Phys. 31*, 688.
Cerri, A., Schmelczer, R., Schwander, P., Kostorz, G., Wright, A.F. (1987), in: *Proc. MRS Symp.*, Vol. 82: *Characterization of Defects in Materials*; Siegel, R.W., Weertman, J.R., Sinclair, R. (Eds.). Pittsburgh: Materials Research Society, p. 169.
Chan, K.S., Lee, J.K., Shiflet, G.J., Russell, K.C., Aaronson, H.I. (1978), *Met. Trans. 9A*, 1016.
Chen, H. (1986), *Scripta Metall. 20*, 1759.
Chen, H., Polat, S., Epperson, J.E. (1988), in: *Dynamics of Ordering Processes in Condensed Matter*; Komura, S., Furnkawa, H. (Eds.). New York: Plenum Press, pp. 245–250.
Cockayne, D.J.H., Gronsky, R. (1981), *Phil. Mag. A44*, 159.
Cook, H.E. (1970), *Acta Metall. 18*, 297.
Cranevich, A. (1975), *Phys. Chem. Glasses 16*, 133.
Cranevich, A.F., Olivier, J.R. (1981), *J. Appl. Cryst. 14*, 144.
Cranevich, A., Sanchez, J.M. (1981), *Phys. Rev. Lett. 47*, 1308.
Cranevich, A.F., Sanchez, J.M., Williams, C.E. (1986), *Phys. Rev. B34*, 2762.
Davies, C.K.L., Nash, P., Stevens, R.N. (1980), *Acta Metall. 28*, 179.
Davies, D.M., Ralph, B. (1972), *J. Microscopy 96*, 343.
de Fontaine, D. (1969), *Trans. AIME 245*, 1703.
de Fontaine, D. (1971), *J. Appl. Crystallogr. 4*, 15.
de Fontaine, D. (1973), *J. Phys. Chem. Sol. 34*, 1285.
Doherty, R.D. (1982), *Metal Science 16*, 1.
Doherty, R.D. (1983), in: *Physical Metallurgy*; Cahn, R.W., Haasen, P. (Eds.), Vol. 2. Amsterdam: North Holland, Physics Publishing, pp. 933–1030.
Doi, M., Miyazaki, T. (1986), *Mater. Sci. Eng. 78*, 87.
Doi, M., Miyazaki, T., Wakatsuki, T. (1984), *Mater. Sci. Eng. 67*, 247.
Doi, M., Fukasa, M., Miyazaki, T. (1988), *Phil. Mag. A 57*, 831.
Eckerlebe, H., Kampmann, R., Wagner, R. (1986), *Atomic Transport and Defects in Metals by Neutron Scattering*; Janot, C., Petry, W., Richter, D., Springer, T. (Eds.). Berlin: Springer Verlag, pp. 66–72.
Enomoto, Y., Kawasaki, K., Tokuyama, M. (1987), *Acta Metall. 35*, 907, 915.
Epperson, J.E. (19■■), in: *Dynamics of Ordering Processes in Condensed Matter*; Komura, S., Furnkawa, H. (Eds.). New York: Plenum Press, pp. 245–250.
Ernst, F., Haasen, P. (1988), *Phys. Stat. Sol. (a), 104*, 403.
Ernst, F., Xiao, S.Q., Haider, F., Wilbrandt, P.-J. (1987), *Scr. Metall. 21*, 1139.
Eshelby, J.D. (1957), *Proc. R. Soc. A241*, 376.
Feder, J., Russel, K.C., Lothe, J., Pound, G.M. (1966), *Advan. Phys. 15*, 111.
Ferguson, P., Jack, K.H. (1984), *Phil. Mag. A50*, 221.
Ferguson, P., Jack, K.H. (1985), *Phil. Mag. A52*, 589.

VCH Verlagsgesellschaft, 6940 Weinheim
Autor:
Material Science & Technology, Vol. 5
Herstellier: Herr Schmitt
Umbruch:
Fahnen:
K. Trittsch, Würzburg
1. Korr.:

Forouhi, A.R., de Fontaine, D. (1987), *Acta Metall. 35*, 1863.
Frenkel, J. (1939), *J. Phys. (USSR) 1*, 315.
Frittel, P., Lebowitz, J.L., Marro, J., Kalos, M.H. (1983), *Acta Metall. 31*, 1849.
Furukawa, H. (1979), *Phys. Rev. Lett. 43*, 136.
Furukawa, H. (1981), *Phys. Rev. A23*, 1535.
Furusaka, M., Ishikawa, Y., Yamaguchi, S., Fujino, Y. (1986), *J. Phys. Soc. Japan. 55*, 2253.
Gaulin, B.D., Spooner, S., Morii, Y. (1987), *Phys. Rev. Lett. 59*, 668.
Gerling, R., Schimansky, F.-P., Wagner, R. (1988), *Acta Metall. 36*, 575.
Gerold, V., Merz, W. (1967), *Scr. Metall. 1*, 33.
Glatter, O. (1982), in: *Small Angle X-Ray Scattering*; Glatter, O., Kratky, O. (Eds.). London: Academic, p. 167.
Gleiter, H. (1983), in: *Physical Metallurgy*; Cahn, R.W., Haasen, P. (Eds.), Vol. 1. Amsterdam: North Holland Physics Publishing, pp. 649–713.
Goldstein, M. (1965), *J. Am. Ceram. Soc. 48*, 126.
Gronsky, R., Okada, M., Sinclair, R., Thomas, G. (1975), *33rd Ann. Proc. E.M.S.A.*, 22.
Grüne, R. (1988), *Acta Metall. 36*, 2797.
Grüne, R., Oehring, M., Wagner, R., Haasen, P. (1985), in: *Rapidly Quenched Metals*, Vol. I; Steeb, S., Warlimont, H. (Eds.). Amsterdam: North Holland, pp. 261–265.
Gunton, J.D. (1984), in: *Decomposition of Alloys: the early stages*; Haasen, P., Gerold, V., Wagner, R., Ashby, M.F. (Eds.). Oxford: Pergamon Press, pp. 1–10.
Haasen, P., Wagner, R. (1985), *Ann. Rev. Mat. Sci. 15*, 43.
Hashimoto, T., Itakura, M., Hasegawa, H. (1986a), *J. Chem. Phys. 85*, 6118.
Hashimoto, T., Itakura, M., Hasegawa, H. (1986b), *J. Chem. Phys. 85*, 6773.
Hennion, M., Ronzaud, D., Guyot, P. (1982), *Acta Metall. 30*, 599.
Herring, C. (1953), in: *Structure and Properties of Solid Surfaces*; Gomer, R., Smith, C.S. (Eds.). Chicago, IL: Univ. of Chicago Press, pp. 5–149.
Hilliard, J.E. (1970), in: *Phase Transformations*; Aaronson, H.I. (Ed.). Metals Park, Ohio: Am. Soc. of Metals, pp. 497–560.
Hirata, T., Kirkwood, D.H. (1977), *Acta Metall. 25*, 1425.
Horiuchi, S., Izumi, F., Kikuchi, T., Uchida, K. (1984), *Phil. Mag. A50*, L29.
Hornbogen, E. (1967), *Aluminium 43*, 115.
Hoyt, J.J. (1989), *Acta Metall. 37*, 2489.
Hoyt, J.J., Sluiter, M., Clark, B., Kraitchman, M., de Fontaine, D. (1987), *Acta Metall. 35*, 2315.
Hoyt, J.J., Clark, B., de Fontaine, D. (1989a), *Acta Metall. 37*, 1597.
Hoyt, J.J., de Fontaine, D. (1989b), *Acta Metall. 37*, 1611.
Hütten, A., Haasen, P. (1985), *J. Phys. (Paris) C7*, 205.

VCH Verlagsgesellschaft, 6940 Weinheim
Autor:
Material Science & Technology, Vol. 5
Herstellier: Herr Schmitt
Umbruch:
Fahnen:
K. Trittsch, Würzburg
1. Korr.:

100

Izumitani, T., Hashimoto, T. (1985), *J. Chem. Phys. 83*, 3694.
Jantzen, C. M. E., Herman, H. (1978), in: *Phase Diagrams. Materials Science and Technology*, Vol. 5: Alper, A. M. (Ed.). New York: Academic Press, pp. 128–185.
Johnson, W. C. (1984), *Acta Metall. 32*, 465.
Johnson, W. C., Voorhees, P. W., Zupon, D. E. (1988), *Met. Trans. 20A*, 1175.
Kalos, M., Lebowitz, J. L., Penrose, O., Sur, A. (1978), *J. Stat. Phys. 18*, 39–52.
Kampmann, R., Wagner, R. (1984), in: *Decomposition of Alloys: the early stages*: Haasen, P., Gerold, V., Wagner, R., Ashby, M. F. (Eds.). Oxford: Pergamon Press, pp. 91–103.
Kampmann, R., Wagner, R. (1986), in: *Atomic Transport and Defects in Metals by Neutron Scattering*: Janot, C., Petry, W., Richter, D., Springer, T. (Eds.). Berlin: Springer Verlag, pp. 73–77.
Kampmann, R., Eckerlebe, H., Wagner, R. (1987), in: *Phase Transitions in Condensed Systems – Experiments and Theory*: Cargill, G. S., Spaepen, F., Tu, K.-N. (Eds.). *MRS-Symp. Proceedings*, Vol. 57. Materials Research Society, Pittsburgh, Pa., pp. 525–542.
Katano, S., Iizumi, M. (1982), *J. Phys. Soc. Japan 51*, 347.
Katano, S., Iizumi, M. (1984), *Phys. Rev. Lett. 52*, 835.
Kaufman, L. (Ed.) (1977), *CALPHAD, 1*. Oxford: Pergamon Press. (Volumes are published annually, from 1977 onwards)
Kaufman, L., Bernstein, H. (1970), *Computer Calculations of Phase Diagrams*. New York: Academic Press.
Kawasaki, K. (1966), *Phys. Rev. 145*, 224 and *148*, 375.
Kawasaki, K. (1972), in: *Phase Transitions and Critical Phenomena*, Vol. 2: Domb, C., Green, M. S. (Eds.). New York: Academic Press, p. 2.
Khachaturyan, A. G. (1983), *Theory of Phase Transformations in Alloys*. New York: John Wiley.
Khachaturyan, A. G., Hairapetyan, V. N. (1973), *Phys. Stat. Sol. (b) 57*, 801.
Kirkwood, D. H. (1970), *Acta Metall. 18*, 563.
Kuo, S. Y., Virkar, A. V. (1987), *J. Am. Ceram. Soc. 70*, C-125.
Langer, J. S. (1971), *Ann. Phys. 65*, 53.
Langer, J. S. (1973), *Acta Metall. 21*, 1649.
Langer, J. S. (1975), in: *Fluctuations, Instabilities, and Phase Transitions*: Riste, T. (Ed.). New York: Plenum Press, pp. 19–42.
Langer, J. S., Schwartz, A. J. (1980), *Phys. Rev. A21*, 948.
Langer, J. S., Bar-On, Miller, H. D. (1975), *Phys. Rev. A11*, 1417.
LaSalle, J. C., Schwartz, L. H. (1984), in: *Decomposition of Alloys: The early stages*: Haasen, P., Gerold, V., Wagner, R., Ashby, M. F. (Eds.). Oxford: Pergamon Press, pp. 104–109.
Laughlin, D. E. (1976), *Acta Metall. 24*, 53.
Laughlin, D. E., Cahn, J. W. (1975), *Acta Metall. 23*, 329.

VCH Verlagsgesellschaft, 6940 Weinheim
Autor:
Material Science & Technology, Vol. 5
Hersteller: Herr Schmitt
Umbruch:
Fahnen:
K. Trittsch, Würzburg
1. Korr.:

Lebowitz, J. L., Kalos, M. H. (1976), *Scripta Metall. 10*, 9.
Lebowitz, J. L., Marro, J., Kalos, M. H. (1982), *Acta Metall. 30*, 297.
Lee, J. H., Johnson, W. C. (1982), in: *Solid-State Phase Transformations*: Aaronson, H. I., Laughlin, D. E., Sekerka, D. F., Wayman, C. M., (Eds.). Warrendale: Met. Soc. AIME, pp. 127–150.
Lee, J. K., Barnett, D. M., Aaronson, H. I. (1977), *Metall. Trans. 8A*, 963.
Lee, Y. W., Aaronson, H. I. (1980), *Acta Metall. 28*, 539.
LeGoues, F. K., Aaronson, H. I. (1984), *Acta Metall. 32*, 1855.
LeGoues, F. K., Aaronson, H. I., Lee, Y. W., Fix, G. J. (1982), in: *Solid-Solid Phase Transformations*: Aaronson, H. I., Laughlin, D. E., Sekerka, R. F., Wayman, C. M. (Eds.). Warrendale: The Metallurgical Society of AIME, pp. 427–431.
LeGoues, F. K., Lee, Y. W., Aaronson, H. I. (1984a), *Acta Metall. 32*, 1837.
LeGoues, F. K., Lee, Y. W., Aaronson, H. I. (1984b), *Acta Metall. 32*, 1845.
LeGoues, F. K., Wright, R. N., Lee, Y. W., Aaronson, H. I. (1984c), *Acta Metall. 32*, 1865.
Lifshitz, I. M., Slyozov, V. V. (1961), *Phys. Chem. Solids 19*, 35.
Liu, Z. G., Wagner, R. (1984), *J. Phys. Colloq. C9*, 441.
Livak, R. J., Thomas, G. (1974), *Acta Metall. 22*, 589.
Lyon, O., Simon, J. P. (1987), *Phys. Rev. B35*, 5164.
Lyon, O., Simon, J. P. (1988), *J. Phys. F. Metal Physics 18*, 1787.
Marqusee, J. A., Ross, J. (1983), *J. Chem. Phys. 79*, 373.
Marro, J., Bortz, A. B., Kalos, M. H., Lebowitz, J. L. (1975), *Phys. Rev. B12*, 2000.
Marro, J., Bortz, A. B., Kalos, M. H., Lebowitz, J. L. (1977), *Phys. Rev. B15*, 3014.
Martin, J. W., Doherty, R. D. (1976), *Stability of Microstructure in Metallic Systems*. Cambridge: University Press, p. 163.
Miller, M. K., Brenner, S. S., Burke, M. G., Soffa, W. A. (1984), *Scripta Metall. 18*, 111.
Miller, M. K., Horton, L. L., Spooner, S. (1986), in: Proc. 32nd Intl. Field Emission Symp.: *J. Phys. (Paris) 47, Coloque C2*: Miller, M. K., Brenner, S. S. (Eds.). Paris: Les Editions de Physique, pp. 409–416.
Mirold, P., Binder, K. (1977), *Acta Metall. 25*, 1435.
Miyazaki, T., Imamura, H., Kozakai, T. (1982), *J. Mater. Sci. Eng. 54*, 9.
Miyazaki, T., Seki, K., Doi, M., Kozakai, T. (1986), *J. Mater. Sci. Eng. 77*, 125.
Morral, J. E., Cahn, J. W. (1971), *Acta Metall. 19*, 1037.
Mullins, W. W. (1986), *J. Appl. Phys. 59*, 1341.
Nelson, G. F. (1969), *Phys. Chem. Glasses 10*, 54.
Nishi, T., Wang, T. T., Kwei, T. K. (1975), *Macromolecules 8*, 227.
Okada, M., Han, C. C. (1986), *J. Chem. Phys. 85*, 5317.

101

VCH Verlagsgesellschaft, 6940 Weinheim
Autor:
Umbruch:
Fahnen:

-971-

Park, M.W., Mitchell, T.E., Heuer, A.H. (1975), *J. Am. Ceram. Soc. 58*, 43.
Park, M.W., Mitchell, T.E., Heuer, A.H. (1976), *J. Mater. Sci. 11*, 1227.
Penrose, O. (1978), in: *Lecture Notes in Physics*, Vol. 84. Garrido, L., Seglar, P., Shepherd, P.J. (Eds.) Heidelberg: Springer Verlag, pp. 210–234.
Penrose, O., Lebowitz, J.L., Marro, J., Kalos, M.H., Sur, A. (1978), *J. Stat. Phys. 19*, 243–267.
Pike, B.C., Messoloras, S., Stewart, R.J. (1989), *Scripta Metall. 23*, 983.
Piller, J., Wagner, W., Wollenberger, H., Mertens, P. (1984), in: *Decomposition of Alloys: the early stages*. Haasen, P., Gerold, V., Wagner, R., Ashby, M.F. (Eds.) Oxford: Pergamon Press, pp. 156–164.
Polat, S., Marsh, C., Little, T., Ju, C.P., Epperson, J.E., Haydn Chen (1986), *Scripta Metall. 20*, 1759.
Polat, S., Haydn Chen, Epperson, J.E. (1989), *Met. Trans. 20 A*, 699.
Radmilovic, V., Fox, A.G., Thomas, G. (1989), *Acta Metall. 37*, 2385.
Rikvold, P.A., Gunton, J.D. (1982), *Phys. Rev. Lett. 49*, 286.
Rindone, G.E. (1975), *Bull. Cent. Glass Ceram. Research Inst. Calcutta 22*, 119.
Riontino, R.J., Laughlin, D.A. (1977), *Metall. Trans. 8 A*, 1285.
Rundman, K.B., Hilliard, J.E. (1967), *Acta Metall. 15*, 1025.
Russel, K.C. (1970), in: *Phase Transformations*. Aaronson, H.I. (Ed.). Metals Park: Am. Soc. Metals, p. 219.
Russel, K.C. (1980), *Advances in Colloid and Interface Sci. 13*, 205.
Sato, R., Han, C.C. (1988), *J. Chem. Phys. 88*, 2057.
Sato, K., Tagawa, K., Inoue, Y. (1989), *Mater. Sci. Engin. A111*, 45.
Sauthoff, G., Pitsch, W. (1987), *Phil. Mag. B 56*, 471.
Servi, I.S., Turnbull, D. (1966), *Acta Metall. 14*, 161.
Seward, T.P., Uhlmann, D.R., Turnbull, D. (1968), *J. Am. Ceram. Soc. 51*, 634.
Shewmon, P.G. (1965), *Trans. TMS-AIME 233*, 736.
Shillet, G.J., Lee, Y.W., Aaronson, H.I., Russell, K.C. (1981), *Scripta Metall. 15*, 719.
Si-Qun Xiao (1989), Ph.D. thesis, Univ. of Göttingen.
Simon-J.P., Lyon, O. (1989), *Acta Metall. 37*, 1727.
Simon, J.P., Guivot, P., DeSalva, A.G. (1984), *Phil. Mag. A 49*, 151.

102

103

Sinclair, R., Thomas, G. (1974), *32nd Ann. Proc. E.M.S.A.*, 500.
Singh, J., Lele, S., Ranganathan, S. (1980), *J. Mater. Sci. 15*, 2010.
Singhal, S.P., Herman, H., Kostorz, G. (1978), *J. Appl. Cryst. 11*, 522.
Skripov, V.P., Skripov, A.V. (1979), *Sov. Phys. Usp. 22*, 389.
Snyder, H.L., Meakin, P. (1983a), *J. Chem. Phys. Soc. 79*, 5588.
Snyder, H.L., Meakin, P. (1983b), *Macromolecules 16*, 757.
Snyder, H.L., Meakin, P. (1985), *J. Polym. Sci. 73*, 217.
Stauffer, D. (1979), *Phys. Rep. 54*, 1.
Steiner, D., Beddoe, R., Gerold, V., Kostorz, G., Schmelczer, R. (1983), *Scripta Metall. 17*, 733.
Stubican, V.S., Schultz, A.H. (1970), *J. Am. Ceram. Soc., 53*, 211.
Sur, A., Lebowitz, J.L., Marro, J., Kalos, M.H. (1977), *Phys. Rev. B15*, 3014.
Taylor, K.A. (1985), Sc.D. Thesis *Aging Phenomena in Ferrous Martensites*, MIT, Cambridge, MA.
Tien, J.K., Shewmon, P.G., Foster, J.S. (1973), *Scripta Metall. 7*, 1171.
Tokuyama, M., Kawasaki, K. (1984), *Physica A123*, 386.
Tsumuraya, K., Miyata, Y. (1983), *Acta Metall. 31*, 437.
Vintaykin, Y.E., Dmitriyev, V.B., Udovenko, V.A. (1979), *Phys. Met. Metall. 46*, 97.
von Alvensleben, L., Wagner, R. (1984), in: *Decomposition of Alloys: The early stages*: Haasen, P., Gerold, V., Wagner, R., Ashby, M.F. (Eds.) Oxford: Pergamon Press, pp. 143–148.
Voorhees, P.W., Glicksman, M.E. (1984), *Acta Metall. 32*, 2001, 2013.
Volmer, M., Weber, A. (1926), *Z. Phys. Chem. 119*, 277.
Wagner, C. (1961), *Z. Elektrochem. 65*, 581.
Wagner, R., Brenner, S.S. (1978), *Acta Metall. 26*, 197.
Wagner, W., Poerschke, R., Wollenberger, H. (1984), in: *Decomposition of Alloys: the early stages*: Haasen, P., Gerold, V., Wagner, R., Ashby, M.F. (Eds.). Oxford: Pergamon Press, pp. 170–179.
Wagner, R., Kampmann, R., Jiang, B., Beaven, P.A. (1988), in: *Proc. Int. Conf. Cu '86 – Copper Tomorrow – Technology, Products, Research*: Ceresara, S. (Ed.). Barga die Lucca, pp. 119–127.
Wahi, R.P., Stajer, J. (1984), in: *Decomposition of Alloys: the early stages* Haasen, P., Gerold, V., Wagner, R., Ashby, M.F. (Eds.) Oxford: Pergamon Press, pp. 165–169.
Wendt, H., Haasen, P. (1983), *Acta Metall. 31*, 1649.
West, A.W., Kirkwood, D.H. (1976), *Scripta Metall. 10*, 681.
Wiltzius, P., Bates, F.S., Dierker, S.B., Wignall, G.D. (1987), *Phys. Rev. A36*, 2991.
Wiltzius, P., Bates, F.S., Heffner, W.R. (1988), *Phys. Rev. Lett. 60*, 1538.
Wood, J.V., Mills, P.F., Bingham, J.K., Bee, J.V. (1979), *Met. Trans. 10 A*, 535.
Yoshida, S., Fukasa, M., Miyazaki, T. (1987), *J. Japan. Inst. Metals 51*, 18.
Zeldovich, J.B. (1943), *Acta Physicochim. USSR 18*, 1.
Zener, C. (1949), *J. Appl. Phys. 20*, 950.

General Reading

Binder, K. (1987), *Advances on Phase Transitions and Disorder Phenomena*. Busiello, G., De Cesare, L., Mancini, F., Marinaro, M. (Eds.). Singapore: World Scientific, pp. 1–71. (Kinetics of First Order Transitions)

Christian, J.W. (1975), *The Theory of Transformations in Metals and Alloys*, 2nd ed. Oxford: Pergamon Press. (General Diffusive Phase Transformations in Solids)

Doherty, R.D. (1983), in: *Physical Metallurgy*, Vol. 2. Cahn, R.W., Haasen, P. (Eds.). Amsterdam: North Holland Physics Publishing, pp. 933–1030. (General Diffusive Phase Transformations in Solids)

de Fontaine, D. (1982), in: *Metallurgical Treatises*. Tien, J.K., Elliott, J.F. (Eds.). Warrendale, Pa.: The Metallurgical Society of AIME, pp. 423–444. (Kinetics of First Order Transitions)

Gaskell, D.R. (1983), in: *Physical Metallurgy*, Vol. 1. Cahn, R.W., Haasen, P. (Eds.). Amsterdam: North Holland Physics Publishing, pp. 271–326. (Metallurgical Thermodynamics)

Glatter, O., Kratky, O. (1982), *Small Angle X-Ray Scattering*. London: Academic. (Experimental Techniques; SAXS)

Gunton, J.D., Droz, M. (1984), *Lecture Notes in Physics*, Vol. 183 – *Introduction to the Theory of Metastable and Unstable States*. Berlin: Springer Verlag. (Kinetics of First Order Transitions)

Gunton, J.D., San Miguel, M., Sahni, P.S. (1983), in: Vol. 8, *Phase Transitions and Critical Phenomena*. Domb, C., Lebowitz, J.L. (Eds.). London: Academic Press, pp. 267–466. (Kinetics of First Order Transitions)

Hobbs, L.W., Westmacott, K.W., Williams, D.B. (Eds.) (1986), *Proc. of the Materials Research Society Symposium*, Vol. 62: *Materials Problem Solving with the Transmission Electron Microscope*. (Experimental Techniques; CTEM)

Kostorz, G. (1979), in: *Neutron Scattering*. Kostorz, G. (Ed.). New York: Academic, p. 227. (Experimental Techniques; SANS)

Martin, G. (1978), in: *Solid State Phase Transformations in Metals and Alloys. Aussois: Les Editions de Physique*, pp. 337–406. (Kinetics of Phase Separation in Solids)

Penrose, O., Lebowitz, J.L. (1979), in: Vol. 7, *Studies in Statistical Mechanics*. Lebowitz, J.L., Montroll, E. (Eds.). Amsterdam: North Holland, pp. 293–340. (Kinetics of First Order Transitions)

Russell, K.C. (1980), *Advances in Colloid and Interface Science 13*, 205. (Nucleation in Solids)

Smith, D.J. (1983), *Helv. Phys. Acta*, 36, 463 (Experimental Techniques; HREM)

Wagner, R. (1982), *Field Ion Microscopy in Materials Science*. Vol. 6, *Crystals-Growth, Properties and Applications*. Freyhardt, H.C. (Ed.). Berlin: Springer Verlag. (Experimental Techniques; AFIM)

Williams, D.B. (1984), *Practical Analytical Electron Microscopy in Materials Science*. New York: VCH Publishers. (Experimental Techniques; ATEM)

VCH Verlagsgesellschaft, 6940 Weinheim
Autor:
Material Science & Technology, Vol. 5
Hersteller: Herr Schmitt
Umbruch:
Fahnen:
K. Trillsch, Würzburg
1. Korr.:

Table 4-1. Some small angle scattering experiments – sometimes jointly employed with other microanalytical tools for studying the morphology – primarily designed for an investigation of spinodal decomposition. If not otherwise stated the concentrations are in at.%. (N.d. not determined.)

Decompositing solid	Experimental technique	Morphology of two-phase microstructure	Authors
Metallic alloys			
Al–4 wt.% Cu	SAXS	Modulated structure	Naudon et al., 1976
Al–22% Zn	SAXS		Gerold and Merz, 1967
Al–22% Zn	SAXS, TEM	Modulated structure	Agarwal and Herman, 1973
Al–20.7 ... 49.1% Zn	SAXS		Bonfiglioli and Guinier, 1966
Al–5.3 ... 6.8% Zn	SANS	GP-zones	Hennion et al., 1982
Al–5.3 ... 12.1% Zn	SANS, TEM		Guyot and Simon, 1982; Simon and Guyot, 1984
Al–22 Zn–0.1 Mg	SAXS, TEM	Interconnected spherical clusters at early times; regularly spaced platelets at later stages	Forouhi and de Fontaine, 1987
Al–12 ... 32% Zn	SAXS (synchrotron radiation)		Hoyt et al., 1989a, b
Al–2.4% Zn–1.3% Mg	SANS		Blasenke et al., 1982, 1983
Al–3.8 ... 9% Li with additions of Cu, Mn	SANS	N.d.	Pike et al., 1989
Au–60% Pt	SANS		Singhal et al., 1978
Fe–28% Cr–10% Co	SANS, TEM, AFIM	'Sponge-like' structure	Miller et al., 1985
Fe–34% Cr	SANS	N.d.	Katano and Iizumi, 1984
Fe–29.5% Cr–12.5% Co	Anomalous SAXS (synchotron source)	N.d.	Simon and Lyon, 1989
Fe–52% Cr	SANS	N.d.	La Salle and Schwartz, 1984
Fe–20 ... 60% Cr	SANS	N.d.	Furusaka et al., 19■
Cu–2.9% Ti	SANS, TEM	Modulated structure	Eckerlebe et al., 1986
CuNiFe	SANS	Modulated structure	Aalders et al., 1984
CuNiFe	SANS, TEM, AFIM	Mottled structure	Wagner et al., 1984
CuNiFe	Anomalous SAXS (synchotron source)	N.d.	Lyon and Simon, 1987

VCH Verlagsgesellschaft, 6940 Weinheim
Autor:
Material Science & Technology, Vol. 5
Umbruch:
Fahnen:
K. Trillsch, Würzburg

Cu–2% Co	SANS	N.d	Steiner et al., 1983
Mn–25...52% Cu	SANS (analysis of integrated intensity)	N.d	Vintaykin et al., 1979
Mn–33% Cu	SANS	N.d	Gaulin et al., 1987
Ni–13% Al	SANS	Anisotropic clustering	Beddoe et al., 1984
Ni–12.5% Si	SANS, SAXS, TEM ('side bands')	Modulated structure	Polat et al., 1986, 1989
Ni–11.5% Ti	SANS/TEM	Modulated structures	Cerri et al., 1987
Glasses, oxides[a]			
B_2O_3–(15 wt.% PbO – – 5 wt.% Al_2O_3) (quasi-binary system)	SAXS		Craievich, 1975 Acuña and Craievich, 1979 Craievich and Olivieri, 1981
B_2O_3–(27 wt.% PbO – – 9 wt.% Al_2O_3)	SAXS (synchrotron source)		Craievich et al., 1986
Vycor-glass	SANS	'Sponge-like' structure consisting of a SiO_2-rich and a B_2O_3-alkali oxide-rich phase	Wiltzius et al., 1987
SiO_2–13 mole% Na_2O	SAXS, TEM	'Sponge-like' structure	Nelson, 1969
TiO_2–(20...80 mole%) SnO_2	SAXS, TEM, X-ray diffraction ('side band' analysis)	Lamellar modulations along [001] (Fig. 4)	Park et al., 1976
Polymer mixtures			
Critical mixture of perdeuterated and protonated 1,4-polybutadiene	Light scattering		Wiltzius et al., 1988, Bates and Wiltzius, 1989
polybutadiene and styrene-butadiene copolymer mixtures			Izumitani and Hashimoto, 1985
polystyrene-polyvinylmethylether (PS-PVME)	Light scattering		Sato and Han, 1988, Snyder et al., 1983a, 1983b, Hashimoto et al., 1986a, 1986b, Okada and Han, 1986

[a] For a comprehensive survey on oxides and glasses up to 1978, see Jantzen and Herman, 1978.

Table 4-1. Cont.

Decomposing solid	Experimental technique	Morphology of two-phase microstructure	Authors

Table 4-1. Cont.

Decomposing solid	Experimental technique	Morphology of two-phase microstructure	Authors

VCH Verlagsgesellschaft, 6940 Weinheim
Autor:
Material Science & Technology, Vol. 5
Herausgeber: Herr Schmitt
Umbruch:
Fahnen:
K. Trittsch, Würzburg
1. Korr.:

Table 4-2. TEM and AFIM studies on phase separating solids which revealed 'spinodal precipitate microstructures'. If not otherwise stated the concentrations are in at.%.

Decomposing solid	Experimental technique	Morphology of two-phase microstructure	Authors
Al–4 wt.% Cu	TEM ('side-bands')	Modulated structure	Rioja and Laughlin, 1977
Al–(2.4...3%) Li	HREM, X-ray diffraction		Radmilovic et al., 1989
$Cu_{1-x}Mn_xAl$	TEM ('side-bands')	Modulated structure; at later stages Cu_2MnAl + Cu_3Al-plates	Bouchard and Thomas, 1975
Cu–(1.5...5.2 wt.%) Ti	TEM ('satellite analysis')	Modulated structure	Laughlin and Calin, 1975
Cu–2.7% Ti	AFIM	Modulated structure	Biehl and Wagner, 1982
Ni–12% Ti	AFIM	Modulated structure	Grüne, 1988
Ni–29% Cu–21% Pd	TEM	Modulated structure	Murata and Iwama, 1981
Ni-base superalloys	AFIM	Short wavelength (≤ 2.5 nm) Cr fluctuation in γ-phase	Bouchon et al., 1989
Nimonic 80A	TEM ('side-bands')	Modulated structure	Wood et al., 1979
Fe–25% Be	AFIM	Modulated structure	
CuNiFe	AFIM	Interconnected percolated structure (cf. Fig. 4-19c)	Pfeler et al., 1984
CuNiFe	TEM ('side-bands')	Modulated structure (cf. Fig. 4-18)	Wahi et al., 1984, Ivak and Thomas, 1974
Co–10% Ti	FIM	Modulated structure	Davies and Ralph, 1972
Cu–3 wt.% Ti – – 1...2 wt.% Fe	TEM ('side-bands')	Modulated structure	Singh et al., 1980
Steels			
Cast Duplex stainless	TEM, AFIM	After decomposition original ferritic Fe–Cr–Ni shows 'sponge-like' structure	Auger et al., 1989
Ferrous martensite Fe–15 wt.% Ni – 1 wt.% C	TEM	Tweed structure	Taylor, 1985
Fe–25 wt.% Ni – – 0.4 wt.% C	TEM	Tweed structure	Taylor, 1985
Austenitic Fe–30 wt.% Mn	TEM ('side-bands')	Modulated structure; formation of K-carbides $(Fe,Mn)_3AlC_x$ at later stages	Kazunori, 1989
Fe–13...20% Mn	X-ray diffraction ('side-bands'), TEM	Modulated structure at early times; isolated Fe_2Mo particles at later stages	Miyazaki et al., 1980
Amorphous alloys			
$Ti_{50}Be_{40}Zr_{10}$	AFIM	Wavy composition profile	Grüne et al., 1984
Glasses, oxides			
TiO_2–60 mole% SnO_2	TEM	Tetragonal system with lamellar modulations along [001]	Srubican and Schultz, 1970
TiO_2–50 mole% SnO_2	HREM	Tetragonal system with lamellar modulations along [001]	Horiuchi et al., 1984
SiC–(50...75 mole%) AlN	TEM ('satellites')	Modulated structure	Kuo and Virkar, 1987

Table 4-2. Cont.

Decomposing solid	Experimental technique	Morphology of two-phase microstructure	Authors

VCH Verlagsgesellschaft, 6940 Weinheim
Autor:
Material Science & Technology, Vol. 5
Herausgeber: Herr Schmitt
Umbruch:
Fahnen:
K. Trittsch, Würzburg
1. Korr.:

108

Table 4-3. Correlation between the width of the miscibility gap and the coherent interfacial energies $\sigma_{\gamma\beta}$ for various two-phase alloys as determined from a fit of the N-model to experimental kinetic data

Alloy at.%		Aging temperature C	Composition type of precipitates	Width of coherent miscibility gap at.%	Coherent interfacial energy $\sigma_{\gamma\beta}$ J m^{-2}
Ni 14 Al	1	550	γ'-Ni_3Al	≈ 15	≈ 0.016
Ni-26 Cu 9 Al	2	550	$\gamma'(Cu,Ni)_3Al$	≈ 20	≈ 0.052
		540	Not determined	≈ 20	≈ 0.050
		580	Not determined	≈ 20	≈ 0.052
Cu 1.9 Ti	3	350	β'-Cu_4Ti	≈ 20	≈ 0.067
Cu-2.7 Ti	4	350	β'-Cu_4Ti	≈ 20	≈ 0.067
Cu-1.5 Co	5	500	>95 at.% Co	≈ 95	≈ 0.171
Fe-1.4 Cu	6	400, 500	>98 at.% Cu	≈ 100	≈ 0.250
Fe-0.64 Cu	6	400	>98 at.% Cu	≈ 100	≈ 0.250

1. Wendt, Haasen, 1983 (AFIM)
2. Liu, Wagner, 1984 (AFIM)
3. v. Alvensleben, Wagner, 1984 (AFIM, CTEM)
4. Eckerlebe, Kampmann, Wagner, 1986 (SANS)
5. Gust, 1986, unpublished (magnet)
6. Kampmann, Wagner, 1986 (SANS)

Papier 109

Figure 4-1. Schematic phase diagram of a binary alloy displaying a miscibility gap. Dashed lines show the metastable coherent solvus line and a possible metastable intermetallic phase β'. The long arrow indicates the quenching process.

Figure 4-2. Neon field ion image of γ'-precipitates (bright images in dark matrix) in Ni-36.8 at.% Cu-8 at.% Al aged for the given times at 580 °C (Liu and Wagner, 1984).

a) 2 min.; $\bar{D}$ = 2.4 nm

b) 180 min.; $\bar{D}$ = 8 nm

c) 420 min.; $\bar{D}$ = 11 nm

Figure 4-3. Time evolution of the mean radius $\bar{R}$, the number density N_v, and the supersaturation Δc of γ'-precipitates in Ni-36 at.% Cu-9 at.% Al during aging at 500 °C (Liu and Wagner, 1984).

Figure 4-4. Free energy as a function of concentration for a binary alloy with a miscibility gap. The changes in free energy and the resulting driving forces for unmixing are illustrated.

Figure 4-5. a) Phase diagram of a binary model alloy with constituents A and B. The two-phase region is subdivided by the mean-field spinodal curve into metastable (hatched) and unstable regions (cross-hatched). b) Schematic free energy versus composition curves at temperature T_1. The bold dashed curve in the two-phase region shows the 'constant' free energy $F'(c)$ of the unstable solid solution.

Figure 4-6. Spatial variation in solute distribution $c(\boldsymbol{r}) = (x, y, z)$) during a) a *nucleation and growth* reaction, and b) a continuous *spinodal* reaction at the beginning (time t_1) and towards the end (t_3) of the unmixing reaction. The notation of the compositions refers to Fig. 4-5; $c_0^{\alpha*}$ and $c_0^{\alpha s}$ are the nominal compositions of the quenched-in metastable and unstable solid solutions, respectively; R^* is the critical radius of the nuclei and λ the wavelength of the composition fluctuations. The direction of the solute flux is indicated by the arrows. After an extended reaction time (e.g. after t_3), the transformation products are similar and do not allow any conclusions to be drawn with respect to the early decomposition mode.

Figure 4-7. Free energy curves and associated driving forces for precipitates of the coherent metastable (F_β) and incoherent equilibrium (F_β) phases.

Figure 4-8. Solubility limits of Cu in Al in the presence of the metastable θ'' and θ' phases (dashed) and the stable θ phase, as a function of temperature (after Hornbogen, 1967).

Figure 4-9. HREM lattice fringe image of Al - 1 at.% Ag aged for 92 h at 413 K with silver-rich precipitates (dark areas). For imaging the Al matrix a rather large defocus (≈ 280 nm) had to be chosen which gives rise to the bright Fresnel surrounding the particles. [Reproduced by courtesy of F. Ernst (Ernst and Haasen, 1988)]

Figure 4-10. Time evolution of the particle size distribution in Al - 1 at.% Ag during aging at 413 K (after Ernst and Haasen, 1988).

Figure 4-11. SANS curves of Cu - 2.9 at.% Ti single crystals aged for the given times at 350 °C. Note that even the homogenized and quenched ('hom') specimen yields SANS intensity, indicating that phase separation has occurred during quenching (Eckerlebe et al., 1986).

Figure 4-12. Nuclear and magnetic SANS curves of Fe - 1.4 at.% Cu aged for 200 h at 400 °C. From the ratio of magnetic and nuclear scattering intensities, the composition of the copper-rich clusters can be derived. Theoretical curves are shown as full lines (Kampmann and Wagner, 1986).

Figure 4-13. HREM micrograph of GP-zones formed during quenching of Al - 1 at.% Ag. The smallest GP-zones have diameters of only ≈ 1 nm. [Reproduced by courtesy of P. Wilbrandt (Ernst et al., 1987)].

Figure 4-14. SANS curves of Cu - 2.9 at.% Ti quenched from the given homogenization temperatures T_H, and (apart from the bottom curve) subsequently aged for 10 min at 350 °C (Eckerlebe, 1986).

Figure 4-15. a) Composition and diameter $\bar{D}$ of β-precipitates in Ni - 36 at.% Cu - 9 at.% Al as a function of aging time at 580 °C. The corresponding precipitate microstructure is shown in Fig. 4-2 (Liu and Wagner, 1984). b) Composition and diameter $\bar{D}$ of the α_1 (matrix) and α_2 (precipitate) phases in Fe - 29 at.% Cr - 24 at.% Co as a function of aging time at 640 °C (Zhu et al., 1986).

Figure 4-16. Field ion image of Fe - 29 Cr - 14 Co - 2 Al - 0.15 Zr (at.%) aged into its optimum magnetic state (Zhu et al., 1986).

Figure 4-17. a) Evolution of the Cr concentration at 525 °C and 600 °C in the Cr-rich α_2 phase as a function of aging time. b) Composition of the Fe-rich (α_1) and Cr-rich (α_2) phase after aging at 525 °C for the given times (in minutes). The dashed line corresponds to the tie-line with a Fe/Co ratio of 3:1 (Zhu et al., 1986).

Figure 4-18. TEM micrographs of Cu - 48 at.% Ni - 8 at.% Fe aged for a) 8 h, b) 23 h, and c) 65 h at 500 °C. Each insert shows two satellites around the bright (002) matrix reflections. The distance between the satellites and the fundamental reflection is inversely proportional to the wavelength of composition modulations or to the precipitate spacing in modulated structures. [Reproduced by courtesy of R. P. Wahi (Wahi and Stajer, 1984)].

Figure 4-19. a) TEM dark field image of γ'-precipitates in Ni - 37 at.% Cu - 8 at.% Al aged for 167 h at 580 °C (Wagner et al., 1988). b) TEM bright field image of Cu - 36 at.% Ni - 4 at.% Cr aged for 240 h at 650 °C displaying particle alignment along the ⟨100⟩ matrix directions (Wagner et al., 1988). c) FIM micrographs of Cu - 48 at.% Ni - 8 at.% Fe aged for 8 h at 500 °C. Between each FIM micrograph 2 nm of the specimen surface were removed ['field evaporated' (Wagner, 1982)] in order to reveal the three-dimensional arrangement of the brightly imaged (Ni, Fe)-rich precipitated phase. In a the precipitates C, D, E, F, G are apparently isolated; after having removed 2 nm, they have merged into one large extended particle (b). At still greater depth (d, 6 nm) 'particle' C appears again to be isolated from the other ones by the darkly imaged matrix. [Reproduced by courtesy of W. Wagner (Piller et al., 1984)]

Figure 4-20. Computer-simulated cross-section of a spinodal structure in an isotropic solid displaying the interconnectivity of the two incipient phases 1 and 2 with equal volume fraction. After Cahn (1965).

Figure 4-21. Strain energy vs. aspect ratio of a Ag precipitate in Cu and Al matrices. The numbers 1, 4, 5, and 7 designate different orientation relationships between matrix and precipitate. The lowest strain energy is obtained if the cubic directions of both particle and matrix are parallel to each other (curves 1). δ is the linear misfit. After Lee et al. (1977).

Figure 4-22. FIM micrographs of $(Fe,Mo)_{16}N_2$ platelets (bright) in an α-iron matrix (dark). During coarsening at 600 °C for the given times the aspect ratio decreases from ≈ 0.1 (t = 0) to ≈ 0.04 (623 h), whereas the platelet thickness increases only from ≈ 0.7 nm to ≈ 1.0 nm. The platelets intersect the surface of the semi-spherical field ion tip and thus appear to be curved (Wagner and Brenner, 1978).

VCH Verlagsgesellschaft, 6940 Weinheim
Autor:
Material Science & Technology, Vol. 5
Hersteller: Herr Schmitt
Umbruch:
Fahnen:
K. Trittsch, Würzburg
1. Korr.:

Figure 4-23. Schematic representation of free energy changes associated with cluster formation as a function of cluster radius (R) or number i of atoms in the cluster. ΔF^0 is the free energy of the homogeneous solid solution, Z the Zeldovich factor

Figure 4-24. Quasi-stationary cluster size distributions of the Volmer-Weber (V-W) and Becker-Döring (B-D) theory.

Figure 4-25. Polar $\sigma_{\alpha\beta}$-plot for particles with anisotropic interfacial energies $\sigma_{\alpha\beta}$. The normals drawn at the tip of each vector $\mathbf{r}$ are the Wulff planes, the inner envelope of which gives the equilibrium shape of the precipitate. If the $\sigma_{\alpha\beta}$-plot displays deep cusps (e.g. for $\mathbf{r}_1$, $\mathbf{r}_3$, and $\mathbf{r}_5$) the Wulff construction yields a faceted polyhedron.

Figure 4-26. Composition profile of a spherical nucleus (center at $r = 0$) in four different metastable solid solutions with composition c_0 quenched to $T = 0.25\,T_c$ into the miscibility gap. The continuous line was calculated from the Cahn-Hilliard continuum model (Eq. (4-37)), the crosses represent calculations based on the discrete lattice point model. (After LeGoues et al., 1984). The computations are based on a regular solution model with the solubility limit $c_\alpha^* = 0.37 \cdot 10^{-3}$ and the spinodal composition $c_\alpha^s = 6.41 \cdot 10^{-2}$; a is the lattice parameter of an assumed f.c.c. lattice and l the interfacial width.

Figure 4-27. Nucleation barrier ΔF^* (a) and critical radius R^* (b) as a function of supersaturation at $T = 0.25\,T_c$ according to classical theory (cl. th.), nonclassical Cahn-Hilliard continuum model (C-H) and discrete lattice model (DLM). R^* is determined such that it corresponds to $(c_0 + c_c)/2$ where c_c is the composition of the nucleus at its center. (After LeGoues et al., 1984a).

Figure 4-28. Schematic concentration field in the matrix surrounding a nucleus with radius R and composition c_p.

Figure 4-29. Cluster size distribution at different aging times (arbitrary units) as obtained from a numerical solution of Eqs. (4-48) and (4-49). After Binder and Stauffer, 1976.

Figure 4-30. a) Schematic phase diagram of a binary alloy (components A and B) with a symmetrical miscibility gap.
b) Variation of the critical radius F^* of a nucleus and of the wavelength λ^* of a critical fluctuation with composition of the alloy at T_0 according to the nonclassical Cahn-Hilliard nucleation theory (C-H noncl.) and the Cahn-Hilliard spinodal theory (C-H spin.). Approaching the spinodal composition c_α^s from either the metastable or the instable region causes R^* and λ^*, respectively, to diverge. In contrast, the generalized nucleation theory of Binder and coworkers yields the size of the critical cluster to decrease steadily until it becomes comparable with the correlation length of typical thermal fluctuations. There is no

VCH Verlagsgesellschaft, 6940 Weinheim
Autor:
Material Science & Technology, Vol. 5
Hersteller: Herr Schmitt
Umbruch:
Fahnen:
K. Trillsch, Würzburg
1. Korr.:

Figure 4-31. a) Time evolution of the structure function $S(\varkappa, t)$, and b) of its peak height S_m and peak position $\varkappa_m$ as predicted by the generalized nucleation theory of Binder and coworkers for a 3-dimensional Ising model ($c_0 = 0.1$, $T/T_c = 0.6$). After Binder et al., 1978.

Figure 4-32. a) Time evolution of the structure function (SANS-experiments) of a Cu - 2.9 at.% Ti single crystal aged at 350 C for the given times. b) Time evolution of the peak height $S_m \propto d\Sigma^m/d\Omega$ and the peak position $\varkappa_m$. After Eckerlebe et al., 1986.

Figure 4-33. Time evolution of $d\Sigma/d\Omega$ for Cu–2.9 at.% Ti aged at 350 C for various constant wavenumbers $\varkappa$ (Eckerlebe et al., 1986).

Figure 4-34. Variation of $R(\varkappa, t)/\varkappa^2$ with $\varkappa^2$ as determined for two different time intervals (Eckerlebe et al., 1986).

Figure 4-35. a) Phase diagram of a binary alloy with a symmetric miscibility gap centered at c_{sym}.
b) Time evolution of the structure function of an alloy with $c_0 = c_{sym}$ quenched and aged at T_A. The insert shows the distribution function of composition configurations at two different times. At $t = 80$ s the evolving two-phase structure with compositions c_1 and c_2 or y_1 and y_2, respectively, with

$$y_1 = \frac{c_1 - c_{sym}}{c_\alpha^* - c_{sym}} \text{ and } y_2 = \frac{c_2 - c_{sym}}{c_\beta^* - c_{sym}}$$

already becomes discernible. All units are dimensionless.
c) LBM-predictions on the variation of $R(\varkappa, t)/\varkappa^2$ with $\varkappa^2$ as determined from b) according to Eq. (4-59). Quantitatively there is good agreement with the LBM-predictions and experimental results, e.g. displayed in Fig. (4-34). After Langer et al., 1975.

Figure 4-36. Time evolution of the structure function (SANS-intensity) of Fe - 40 at.% Cr aged at 515 °C for the given times. Full lines are calculated from the LBM theory with three free fitting parameters. After Furusaka et al., 1986.

Figure 4-37. The phase diagram and the spinodal curves for composition waves along ⟨001⟩, ⟨101⟩, and ⟨100⟩ directions for elastically anisotropic tetragonal TiO_2 - SnO_2. The spinodals were calculated on the basis of the regular solution model. From Park et al., 1976.

Figure 4-38. CTEM-micrograph of equimolar TiO_2 - SnO_2 displaying a lamellar structure consisting of alternating TiO_2- and SnO_2-rich layers formed after aging at 900 C for 60 min. From Park et al., 1976

VCH Verlagsgesellschaft, 6940 Weinheim
Autor:
Material Science & Technology, Vol. 5
Umbruch:
Fahnen:
K. Trillsch, Würzburg

Figure 4-39. Variation of the phase boundaries in the Fe–Ni–Cr ferrite phase with chromium content as derived from microstructural observations. After Auger et al., 1989.

Figure 4-40. Phase diagram of the 3-dimensional Ising model approximating a binary model alloy. In terms of the mean field theory (Sec. 4.2.2) 'alloys' # 1 to # 4 are quenched into the metastable regime, 'alloys' # 5 to # 7 beyond the classical spinodal line are quenched into the unstable region of the phase diagram. After Lebowitz et al., 1982.

Figure 4-41. Time evolution of the structure function at $T/T_c = 0.59$ as obtained from MC-computer simulations. With reference to Fig. 4-40:
a) is for 'alloy' # 1 with $c_0 = 0.05$ (after Lebowitz et al., 1982),
b) for 'alloy' # 4 with $c_0 = 0.2$ (after Sur et al., 1977) and
c) for 'alloy' # 5 with $c_0 = 0.5$ (after Marro et al., 1975). The given times are in units of a Monte Carlo step, i.e., the average time interval between two attempts at exchanging the occupancy of a specific site. The numerical results for $S(z, t)$ at the discrete values of z were connected by straight lines.

Figure 4-42. CTEM-analyses of the normalized γ'-particle size distribution in Ni–8.74 wt.% Ti after aging at 692 °C for the given times. For comparison, the shape-invariant distribution function f_{LSW} (Eq. (4-64)) of the LSW-theory is included. After Ardell, 1970.

Figure 4-43. Steady state distribution of the 'source/sink strength' $B_i = \text{const}\,(\bar{R}_i \cdot R_i^3)$ plotted versus the normalized particle radius $R_i/\bar{R}$. The plot represents about 2000 B_i's. After Voorhees and Glicksman, 1984. For comparison $B_{LSW} = (R/\bar{R}) - \frac{1}{3}$ is also shown. Note that if, unlike in the LSW-theory, particle interaction is properly taken into account particles with, for instance, the size $R^*_{LSW}/\bar{R}$ may grow or dissolve depending on their specific environment.

Figure 4-44. Relative coarsening rate $\alpha(f_p)/\alpha_{LSW}$ versus volume fraction as predicted by the models of Enomoto et al. (1987) (E); Voorhees and Glicksman (1984) (VG); Marqusee and Ross (1984) (MR); Tokuyama and Kawasaki (1984) (TK). α_{LSW} is defined by Eq. (4-62a).

Figure 4-45. Steady-state (time-invariant) precipitate size distributions at various volume fractions. For comparison the corresponding LSW-distribution for zero volume fraction is also shown. After Voorhees and Glicksman, 1984.

Figure 4-46. a) Shape changes and splitting of a γ'-Ni_3Al cuboidal precipitate in Ni–12 at % Al during aging at 860 °C. In (a) the particle dissolves in its center where the black matrix becomes discernible as a rod; in (b) the rod has widened along the ⟨100⟩ directions during further aging; in (c) the particle is just about to split into two paired γ'-plates.
b) Dark field CTEM image of γ'-particles in Ni–12 at % Al after aging for 40 h at 860 °C showing several paired γ'-plates apparently resulting from the splitting mechanism shown in a). From Miyazaki et al., 1982.

Figure 4-47. Variation of the elastic interaction energy between two spherical particles with various relative sizes R^0 (cf. Eq. (4.65)) as a function of the interparticle distance d (in units of the mean particle diameter $2\bar{R}$ for $R^0 = 0$) or with the volume fraction. After Miyazaki et al., 1986. The results are representative for coherent cobalt rich particles in a copper matrix.

Figure 4-48. The change of the total energy of two interacting coherent particles for three different normalized particle distances, d, or related volume fractions, f_p, as a function of their relative size, R^0. After Miyazaki et al., 1982.

Figure 4-49. Bifurcation diagram calculated for a volume fraction $f_p = 10\%$ (or $d = 1.74$) as a function of the mean particle radius. The arrows indicate the direction of decreasing total energy. In region I one large particle represents the stable configuration ($R^0 \to \pm 1$); in region II two particles with equal size ($R^0 \to 0$) are stable. (The dashed line shows when the absolute energy minimum lies in region II. The employed minimum lies in region II. The employed elastic constants, misfit strains and surface energy were adopted from the two-phase Cu–Co system. After Miyazaki et al., 1986.)

Figure 4-50. Illustration of the relationship between the 'true' continuous size distribution function $f(R, t)$ yielding the mean radius $\bar{R}$, with the related parameters of the LS-model. LS assumed a monodispersive distribution, f_{LS}, of particles with radius $\bar{R}_{LS}$. $f_p(R^*, t)\,dR^*$ is the apparent number density of particles with radii between R^* and $R^* + dR^*$. In the LS-theory, only particles in the hatched region belong to the precipitated phase.

Figure 4-51. Evolution of various scaled precipitation parameters with scaled aging time τ according to both the N-model and the MLS-model. The chosen values of $\zeta_{0,\alpha}$ correspond to those for Cu–1.9 at % Ti aged at 350 °C.

Figure 4-52. Evolution of the scaled size distribution function in Cu - 1.9 at.% Ti with aging time as computed with the N-model. For comparison, the distribution functions $f_{LSW}(\varrho, t)$, as calculated from Eq. (4-64) with the known values of $N_v(t)$ and $\bar{R}(t)$ are also shown. $D = 2.5 \cdot 10^{-15}$ cm^2 sec

Figure 4-53. Variation of $\bar{R}$, R^*, $\bar{R}_{LS}$ and of the relative supersaturation with aging time for Cu - 1.9 at.% Ti as computed with the N-model and the MLS-model for the given set of thermodynamics data; also shown are the experimental data for $\bar{R}(t)$ from von Alvensleben and Wagner, 1984.

Figure 4-54. a) Variation of R^3 and R^{*3} with time during the growth regime for Cu - 1.9 at.% Ti. During the period marked by the two arrows the kinetics follow the power-law $\bar{R} \sim t^{1/2}$.
b) Variation of the coarsening rate dR^3/dt with aging time; z_{LSW} is the value predicted by the LSW-theory.

Figure 4-55. Variation of N_v and of J^* with aging time for Cu - 1.9 at.% Ti as computed with the N-model and the MLS-model for $\sigma_{\alpha\beta} = 0.067$ J m^{-2}; for this value of $\sigma_{\alpha\beta}$ the computed $N_v(t)$-curve agrees well with the experimental data; poor agreement is obtained for $\sigma_{\alpha\beta} = 0.071$ J m^{-2}.

Figure 4-56. Decrease of the solute concentration in the matrix with aging time, as determined from Laue-scattering (○), from the integrated intensity (×), and the Guinier approximation (●).

Figure 4-57. Time evolution of (a) the cluster number density N_v and the nucleation rate J, (b) of their mean radius $\bar{R}$ and of the critical radius R^*, and (c) of the supersaturation. Experimental results: discrete symbols; computational results: full lines.

Figure 4-58. Kinetic evolution of the precipitated number density (top) and of the mean radius (bottom) as predicted by the N-model for Fe - 1.38 at.% Cu. The solid points refer to experimental data derived from nuclear and magnetic SANS experiments. The dashed lines show the accelerating effect of the b.c.c. → f.c.c. transformation of the copper rich particles on the kinetic evolution.

Figure 4-59. Time dependence of the scaling function $\bar{F}(x/x_m) = x_m^3 S(x,t)$ for Mn - 33 at.% Cu at 450 °C. For later times ($t \geq 5115$ s) $\bar{F}(x/x_m)$ becomes time independent and, hence, dynamic scaling holds (top). The structure functions taken at earlier times (965, 1602, 2239, 2886, and 3532 s) do not yet display scaling behavior (bottom). After Gaulin and Spooner, 1987.

Figure 4-60. Variation of the time-exponent a with aging time as evaluated for Cu - 1.9 at.% Ti by means of the Numerical Model.

Figure 4-61. Dynamical scaling of the structure function of Cu - 2.9 at.% Ti beyond $t = 250$ min; SANS-results from Eckerlebe et al., 1986.

M6

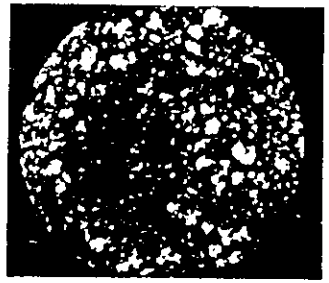

a) 2 min.; $\bar{D}$ = 2,4 nm

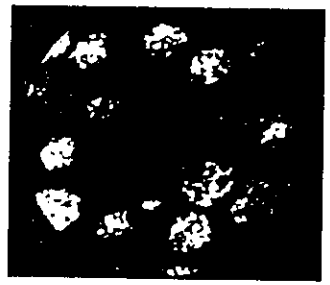

b) 180 min.; $\bar{D}$ = 8 nm

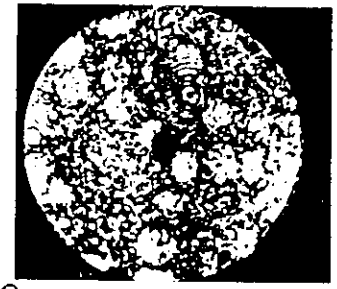

c) 420 min.; $\bar{D}$ = 11 nm

(2)

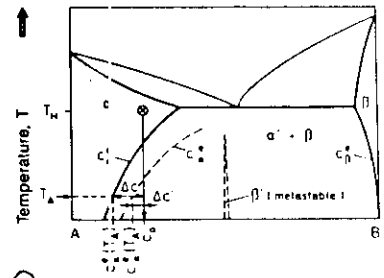

(1)

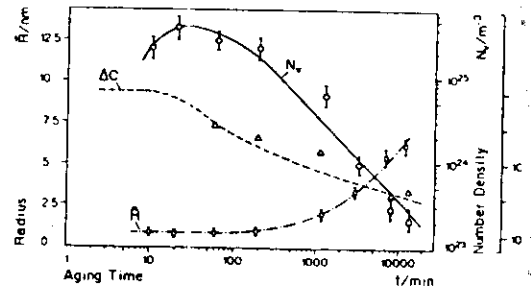

(3)

VCH Verlagsgesellschaft, 8940 Weinheim
Autor:
Material Science & Technology, Vol. 5
Hersteller: Herr Schmitt
Umbruch:
Fahnen:
K. Trilsch, Würzburg
1. Korr.:

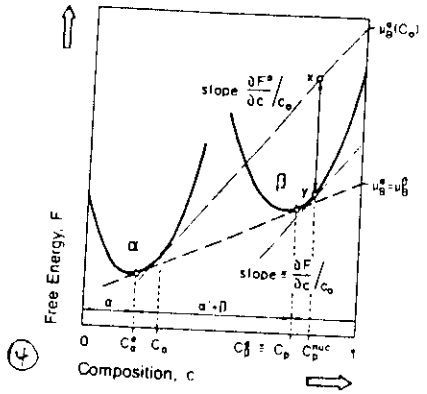
Free Energy, F
Composition, c
slope $\frac{\partial F^{\alpha}}{\partial c}\Big/_{c_0}$
slope $= \frac{\Delta F}{\Delta c}\Big/_{c_0}$
$\mu_B^{\alpha}(C_0)$
$\mu_B^{\alpha}=\mu_B^{\beta}$
α
β
α'+β
C_α^α
C_0
$C_\beta^\beta \equiv C_p$
C_p^{nuc}
1

④

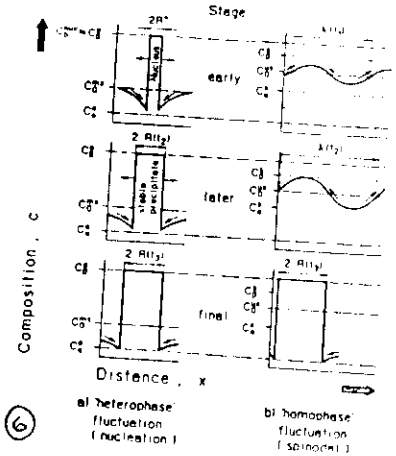
Stage
early
later
final
Composition, c
Distance, x
a) heterophase fluctuation (nucleation)
b) homophase fluctuation (spinodal)

⑥

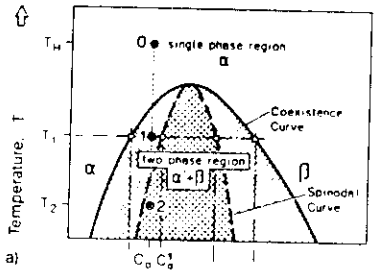
Temperature, T
single phase region
α
Coexistence Curve
two phase region
α+β
β
Spinodal Curve
T_H
T_1
T_2
1
2
C_0 C_α^1
a)

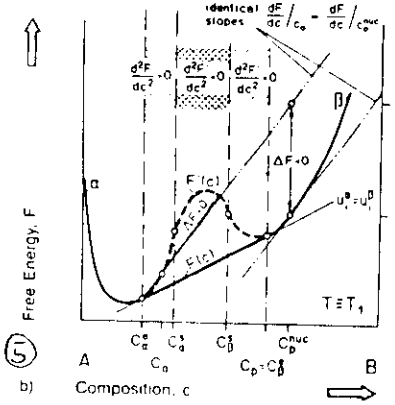
identical slopes $\frac{dF}{dc}\Big/_{c_0} = \frac{dF}{dc}\Big/_{c_p^{nuc}}$
$\frac{d^2F}{dc^2}>0$
$\frac{d^2F}{dc^2}<0$
$\frac{d^2F}{dc^2}>0$
α
β
F(c)
ΔF<0
$T \equiv T_1$
Free Energy, F
C_α^α
C_α^1
C_0
C_β^β
C_p^{nuc}
A
B
$C_p = C_\beta^\beta$
b)
Composition, c

⑤

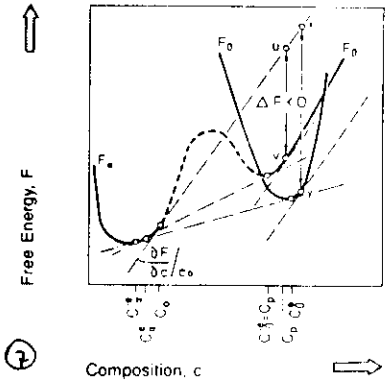
F_0
u_0
u_0'
F_0
ΔF<0
F_α
$\frac{\partial F}{\partial c}\Big/_{c_0}$
$C_\alpha^\alpha = C_0$
$C_\beta^1 = C_p$
C_p C_β^β
Free Energy, F
Composition, c

⑦

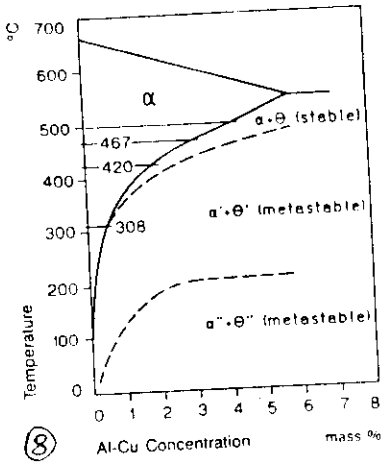
°C
Temperature
α
α+Θ (stable)
α'+Θ' (metastable)
α''+Θ'' (metastable)
467
420
308
Al-Cu Concentration
mass %

⑧

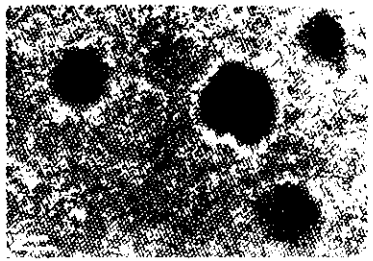

⑨

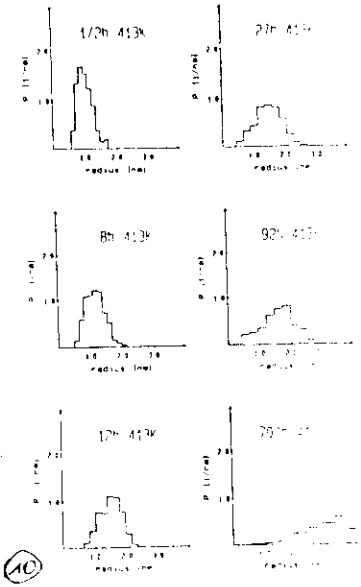
1/2h 413K
2h 413K
8h 413K
92h 413K
12h 413K
radius (nm)

⑩

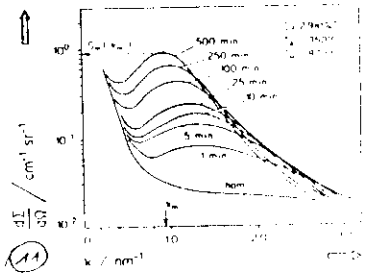
500 min
250 min
100 min
25 min
5 min
1 min
nom
$\frac{dI}{d\Omega}$ / cm^{-1} sr^{-1}
k / nm^{-1}

⑪

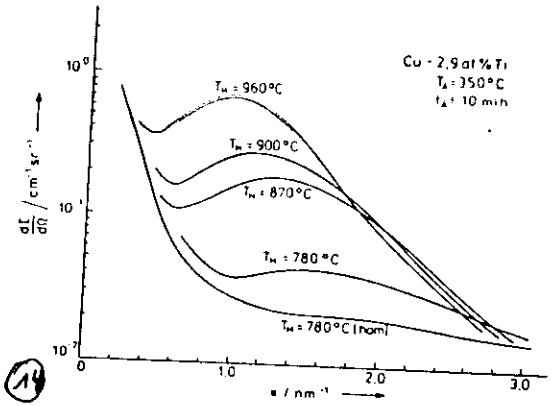

(14)

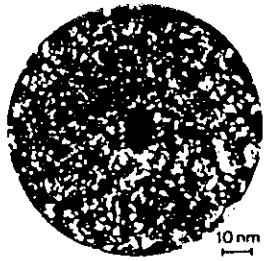

(16)

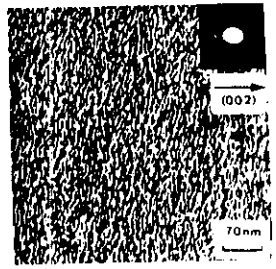

É ll [110] DF with (002)

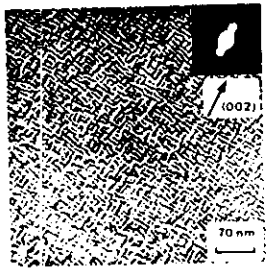

B ll [110] BF

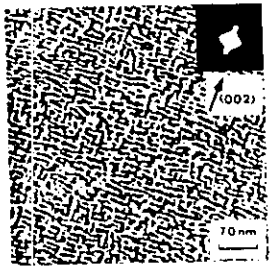

(15) B ll [110] BF

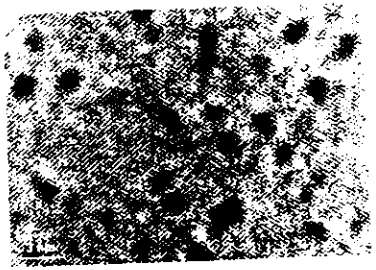

(13)

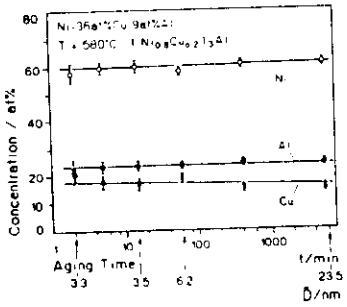

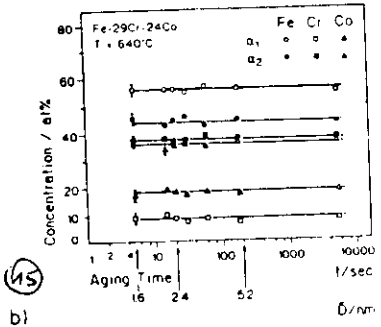

(15)

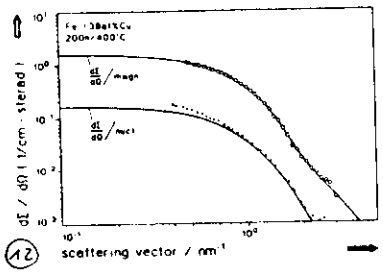

(12)

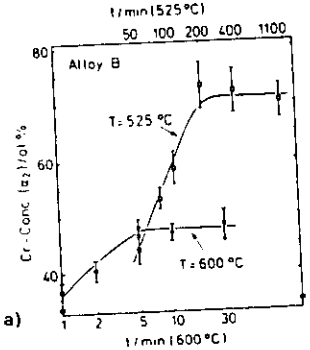

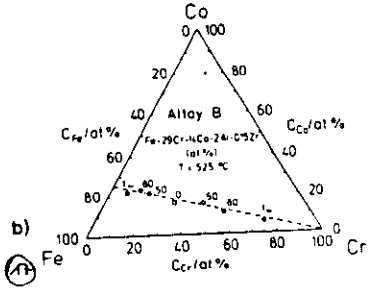

(11)

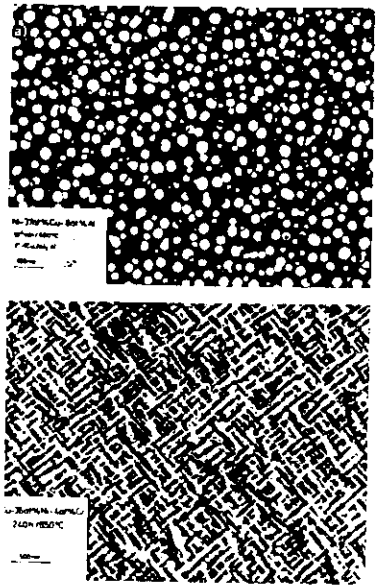

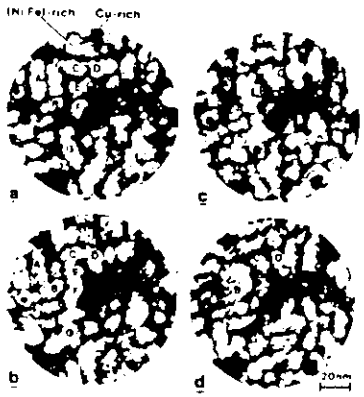

(19) Cu - 48at%Ni - 8at%Fe (8h/500°C)

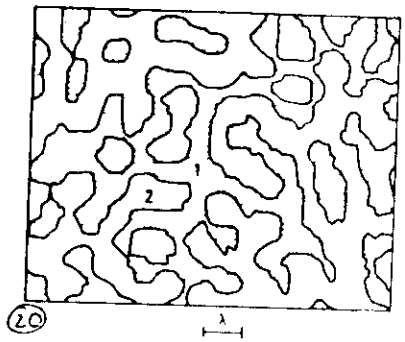

(20)

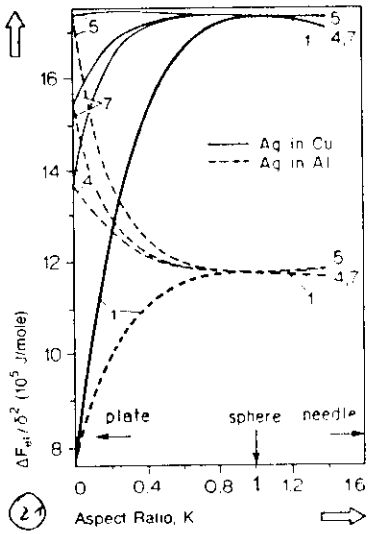

(21)

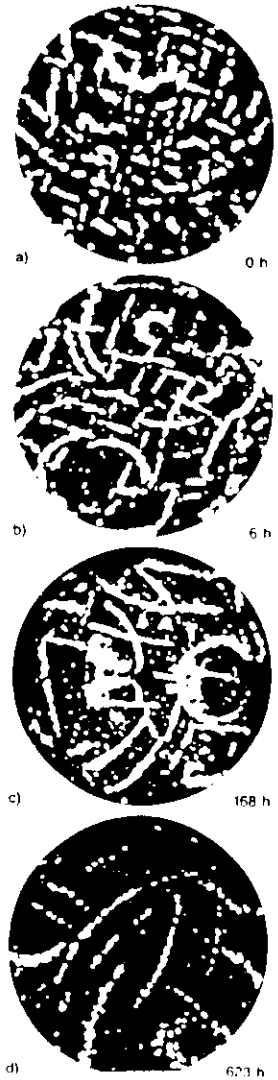

(22)

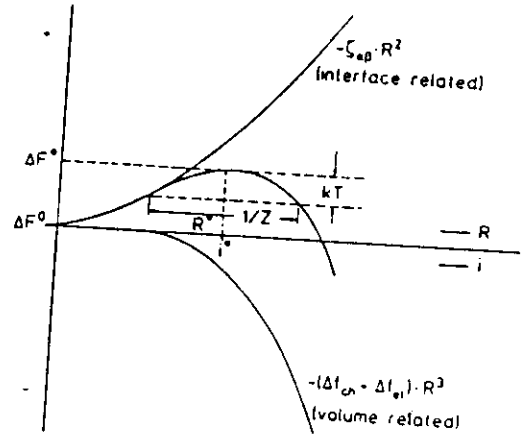
$-\zeta_{ap} \cdot R^2$
(interface related)
ΔF^*
ΔF^0
kT
R^*
1/Z
R
i
$-(\Delta f_{ch} + \Delta f_{el}) \cdot R^3$
(volume related)

(23)

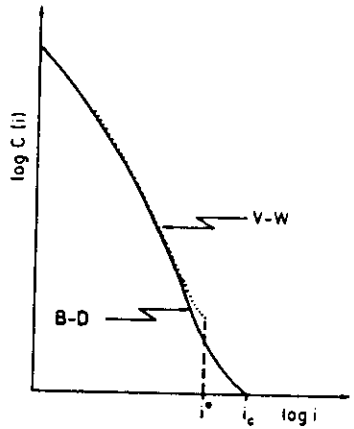
log C (i)
V-W
B-D
i^*
i_c
log i

(24)

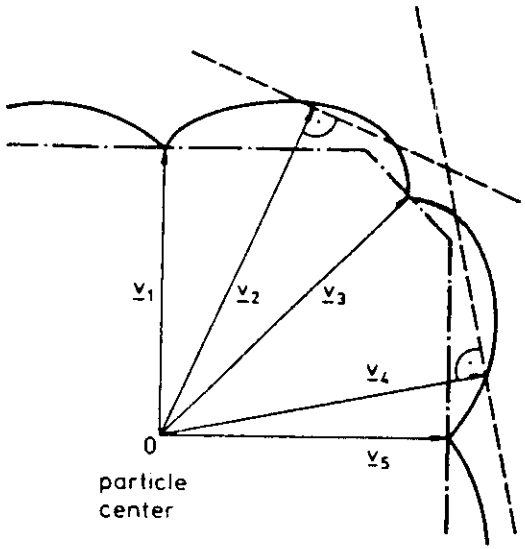

—— Polar $\zeta_{\alpha\beta}$-plot of free energy

– – – Wulff planes normal to radial vectors $\underline{v}$

–·–·– Surface of equilibrium polyhedron

66%

25

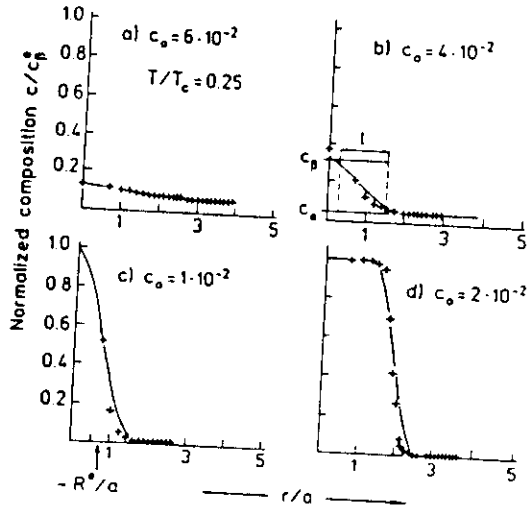

26

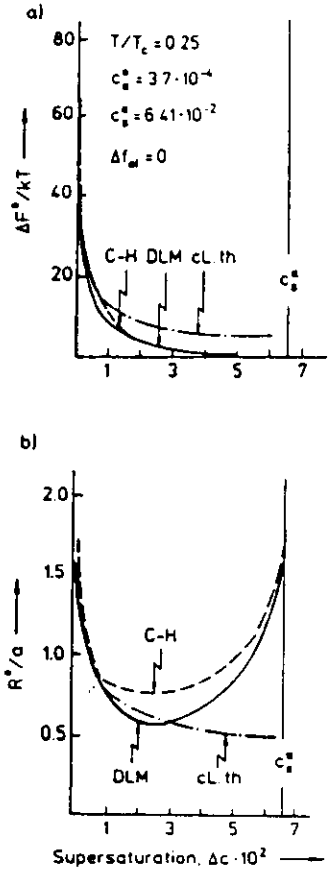
a)
$T/T_c = 0.25$
$c_a^* = 3.7 \cdot 10^{-4}$
$c_b^* = 6.41 \cdot 10^{-2}$
$\Delta f_{el} = 0$
$\Delta F^*/kT$
C-H DLM cL th
c_a^*
b)
R^*/a
C-H
DLM
cL th
c_a^*
Supersaturation, $\Delta c \cdot 10^2$

(27)

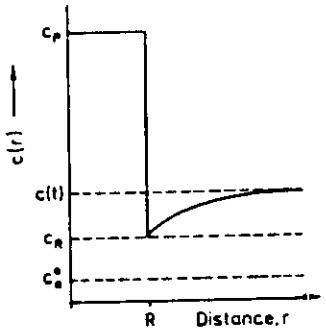
c_p
c(r)
c(t)
c_R
c_a^*
R
Distance, r

(28)

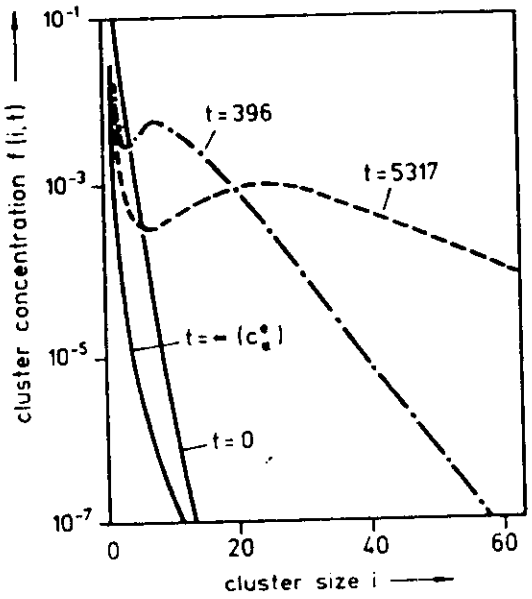
cluster concentration f (i, t)
10^{-1}
10^{-3}
10^{-5}
10^{-7}
t = 396
t = 5317
t = – (c_a^*)
t = 0
0
20
40
60
cluster size i

29

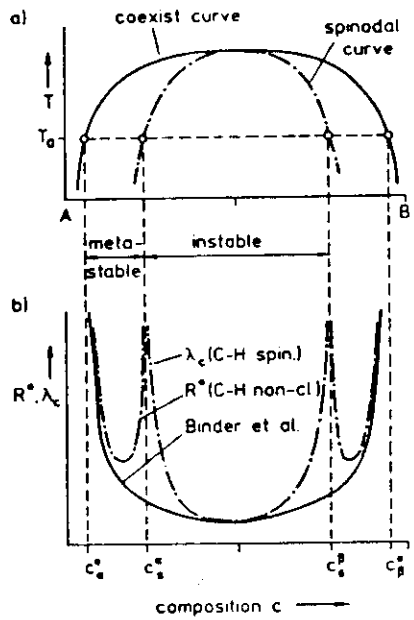
a)
coexist curve
spinodal curve
T
T_a
A
B
meta-
stable
instable
b)
R^*, λ_c
λ_c (C-H spin.)
R^* (C-H non-cl.)
Binder et al.
c_a^*
c_a^c
c_a^B
c_β^*
composition c

30

75%

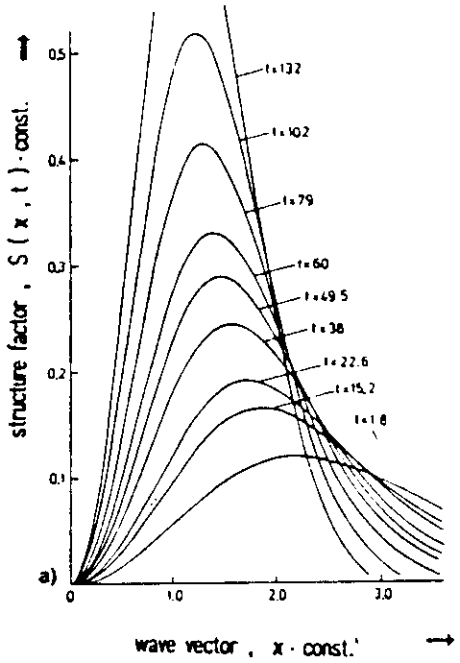
structure factor , S (x , t) · const.
t = 132
t = 102
t = 79
t = 60
t = 49.5
t = 38
t = 22.6
t = 15.2
t = 1.8
a)
wave vector , x · const.'

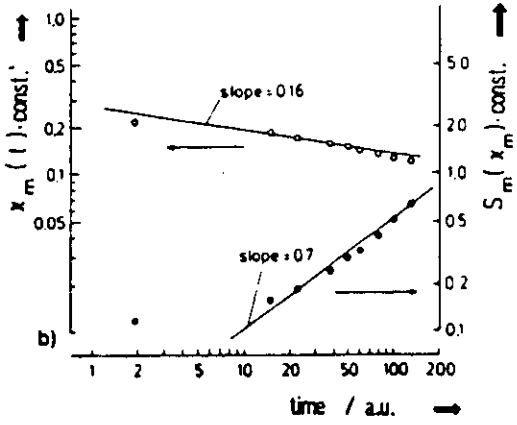
x_m (t) · const.'
S_m (x_m) · const.
slope = 0.16
slope = 0.7
b)
time / a.u.

31a/b

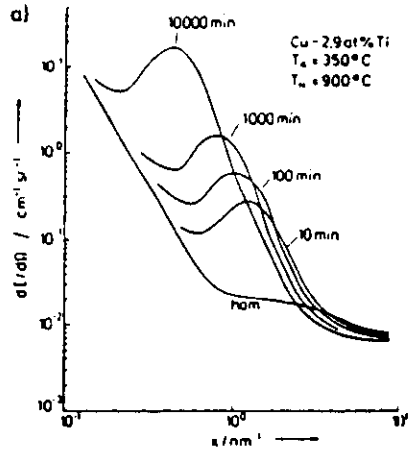
a)
10000 min
1000 min
100 min
10 min
non
Cu - 2.9 at % Ti
T_A = 350°C
T_M = 900°C
α(ω) / cm⁻¹ s⁻¹
x / nm⁻¹

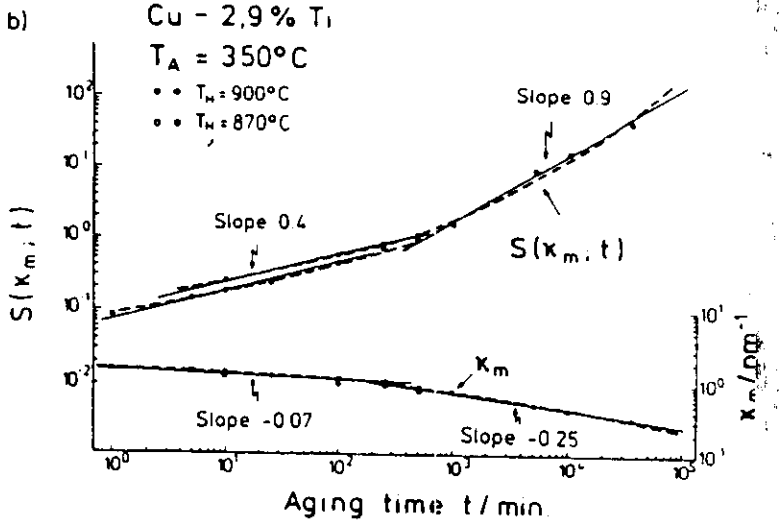
b)
Cu - 2,9 % Ti
T_A = 350°C
T_M = 900°C
T_M = 870°C
Slope 0.9
Slope 0.4
S(x_m, t)
x_m
Slope -0.07
Slope -0.25
S(x_m, t)
x_m / nm⁻¹
Aging time t / min

32

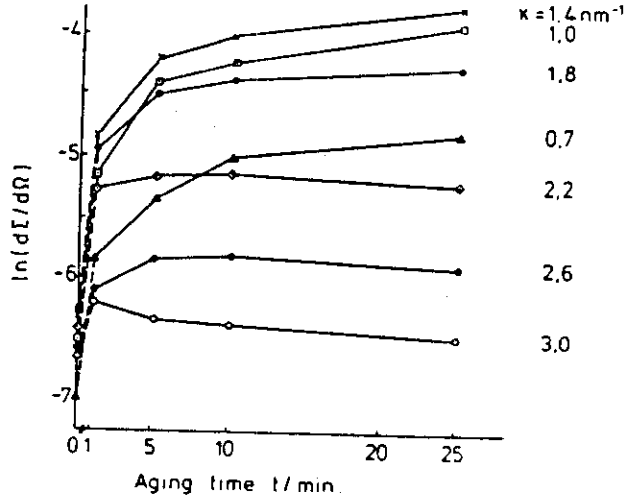
κ = 1,4 nm⁻¹
1,0
1,8
0,7
2,2
2,6
3,0
Cu - 2,9 at % Ti
T_A = 350° C
T_H = 870° C
ln(dΣ/dΩ)
-4
-5
-6
-7
0 1
5
10
20
25
Aging time t / min.

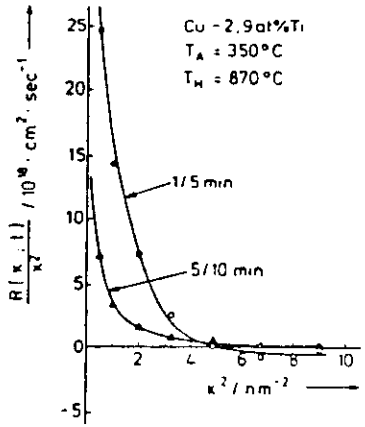
Cu - 2,9 at% Ti
T_A = 350°C
T_H = 870°C
1/5 min
5/10 min
25
20
15
10
5
0
-5
2
4
6
8
10
κ² / nm⁻²

(33)

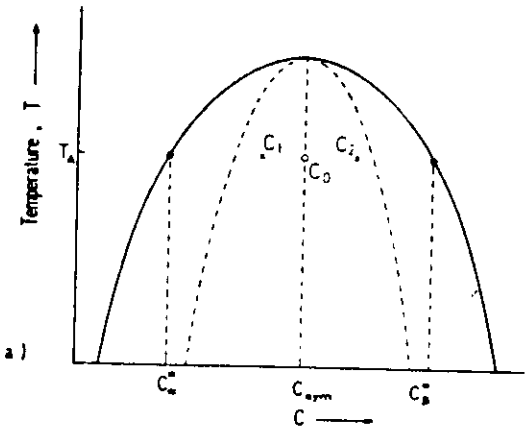

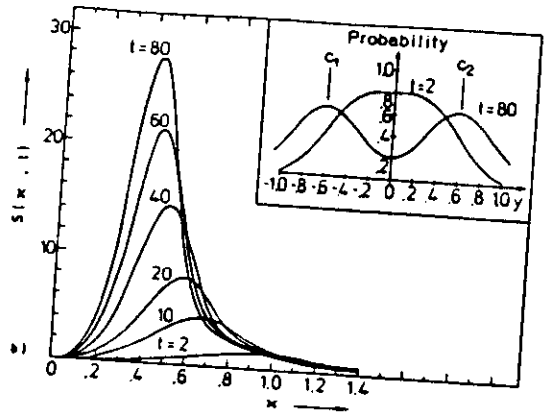

60%

Fig. 4-35b

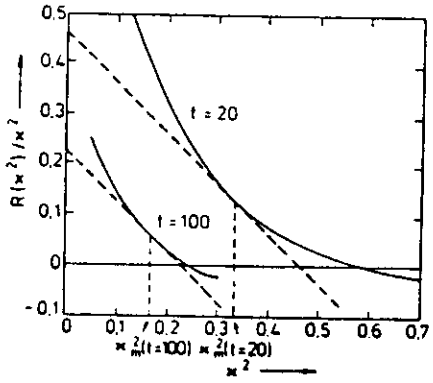

87!

Fig. 4-35

Fig. 4-35c

10%

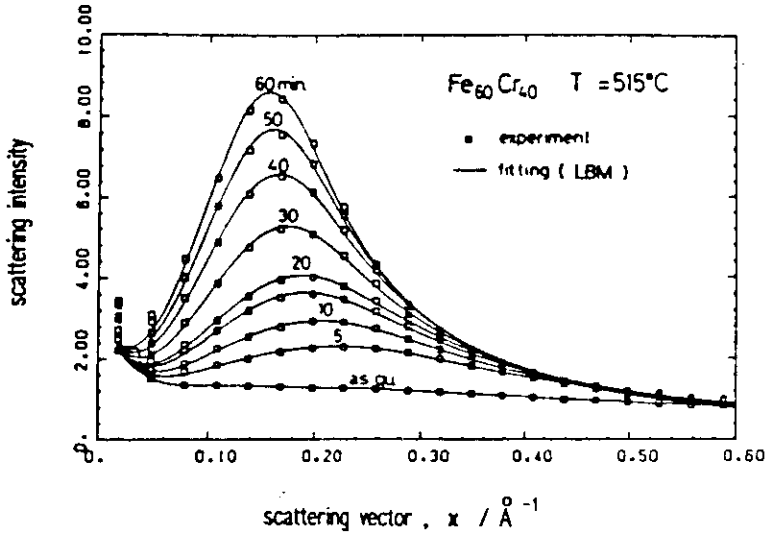
scattering intensity
10.00
8.00
6.00
4.00
2.00
0.
0.10
0.20
0.30
0.40
0.50
0.60
scattering vector , x / Å -1
60 min
50
40
30
20
10
5
as qu
Fe60 Cr40 T =515°C
experiment
fitting (LBM)

(36)

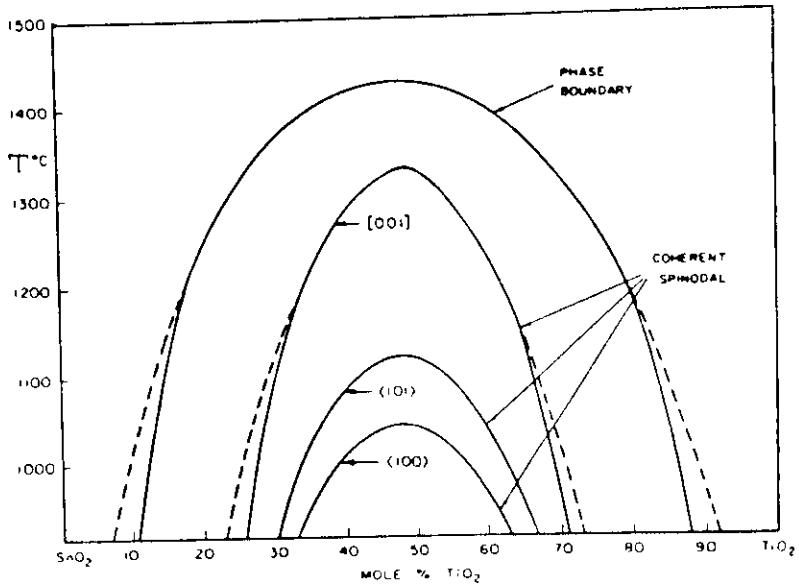
1500
1400
T°C
1300
1200
1100
1000
PHASE BOUNDARY
[001]
COHERENT SPINODAL
(101)
(100)
SiO2
10
20
30
40
50
60
70
80
90
TiO2
MOLE % TiO2

(37)

Fig

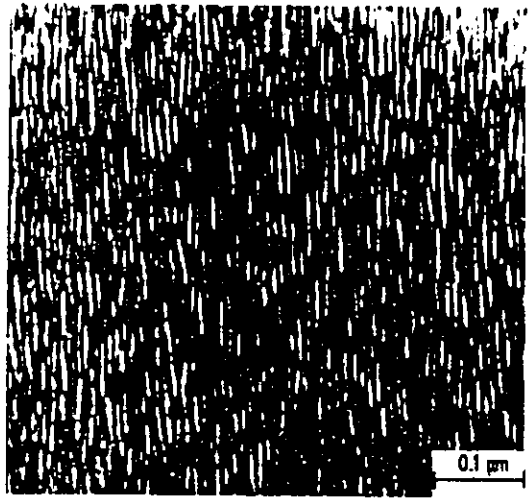
0.1 μm

38

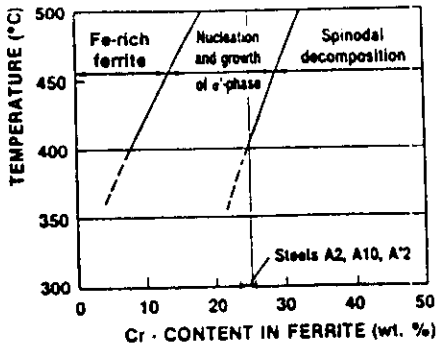
TEMPERATURE (°C)
500
450
400
350
300
Fe-rich ferrite
Nucleation and growth of α'-phase
Spinodal decomposition
Steels A2, A10, A'2
0
10
20
30
40
50
Cr - CONTENT IN FERRITE (wt. %)

39

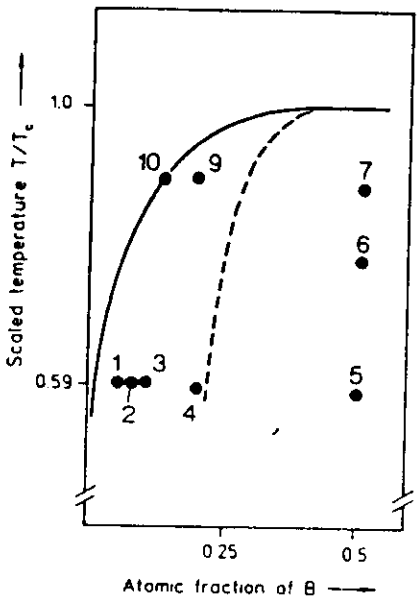

40

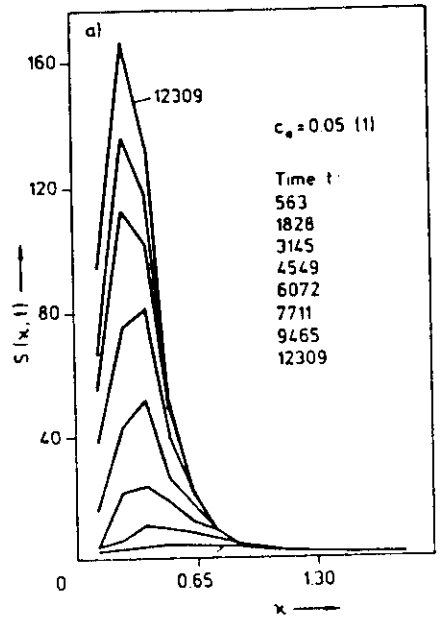

41a

45%
F 4-41a

52

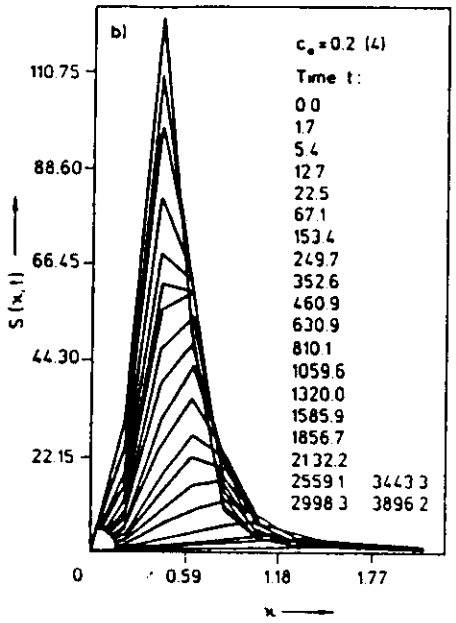

41b

+5%
= 4-40 b

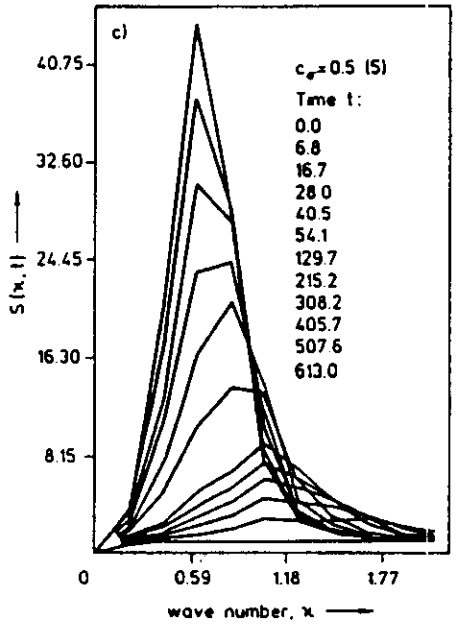

41c

+5%
= 4-40c

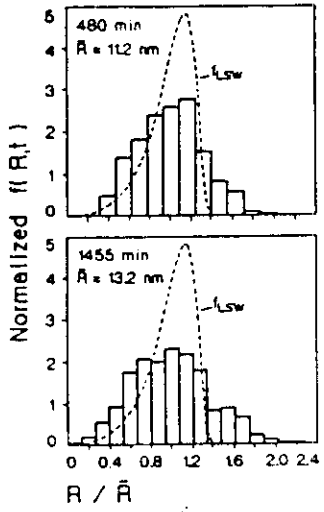
480 min
$\bar{R}$ = 11.2 nm
f_{LSW}
1455 min
$\bar{R}$ = 13.2 nm
f_{LSW}
Normalized f(R,t)
0 0.4 0.8 1.2 1.6 2.0 2.4
R / $\bar{R}$

(42)

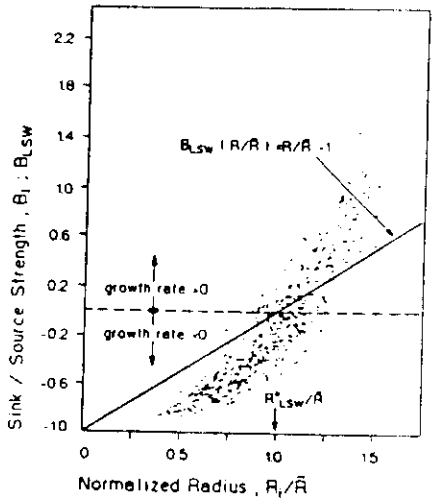
B_{LSW} (R/$\bar{R}$) =R/$\bar{R}$ -1
growth rate >0
growth rate <0
$R^*_{LSW}/\bar{R}$
Sink / Source Strength , B_i ; B_{LSW}
Normalized Radius , $R_i/\bar{R}$

(43)

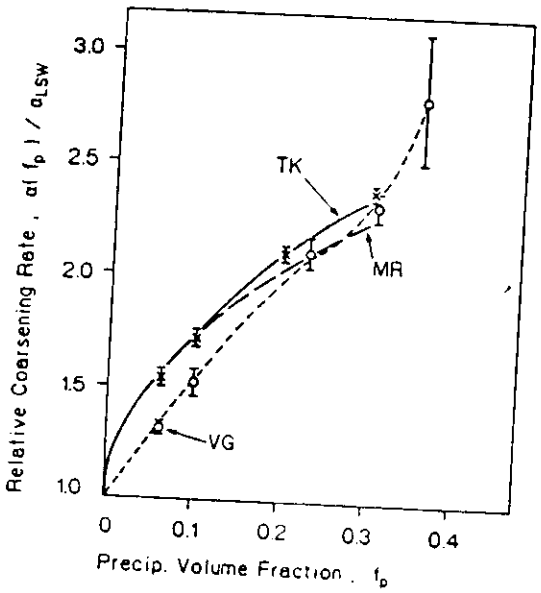
Relative Coarsening Rate , a(f_p) / a_{LSW}
3.0
2.5
2.0
1.5
1.0
TK
MR
VG
0
0.1
0.2
0.3
0.4
Precip. Volume Fraction , f_p

(44)

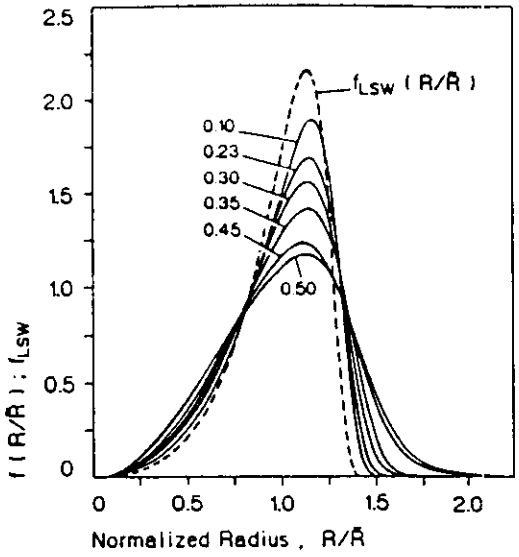
2.5
2.0
1.5
1.0
0.5
0
f_{LSW} (R/$\bar{R}$)
0.10
0.23
0.30
0.35
0.45
0.50
f (R/$\bar{R}$) ; f_{LSW}
0
0.5
1.0
1.5
2.0
Normalized Radius , R/$\bar{R}$

(45)

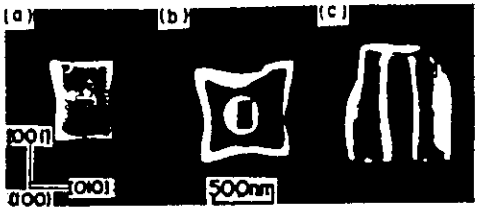

a)

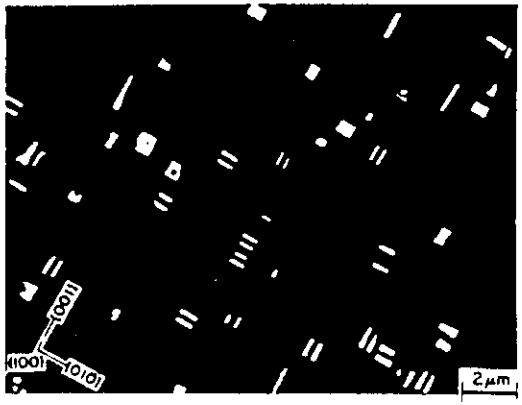

b)

(46)

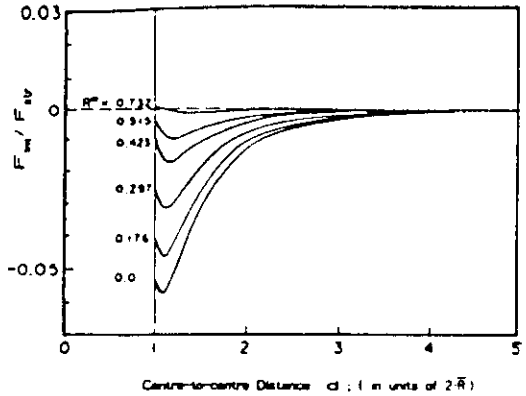

(47)

60

Fig 4-46

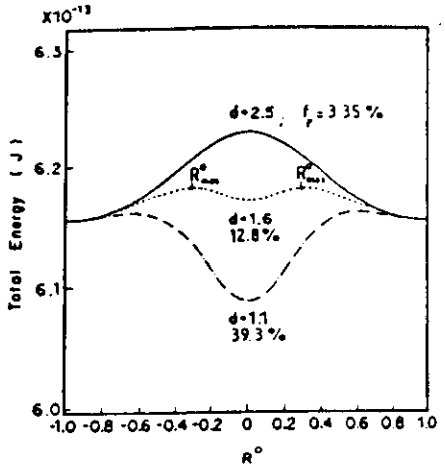

(48)

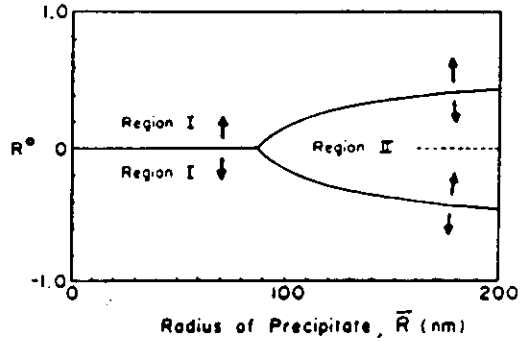

(49)

48

Fig. 4-48

66

Fig. 4-49

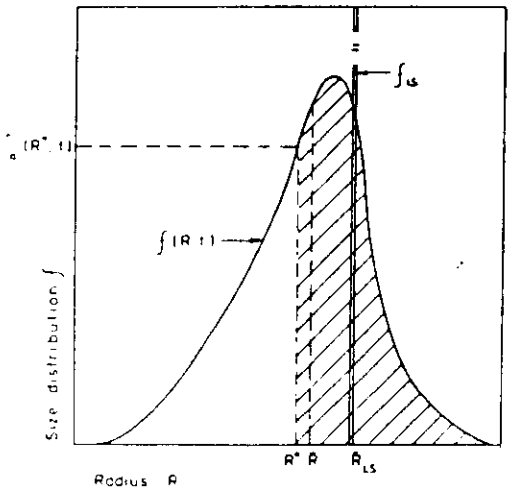
Size distribution f
Radius R
R*
R
R_LS
f(R*,t)
f(R,t)
f_LS

(50)

(51)

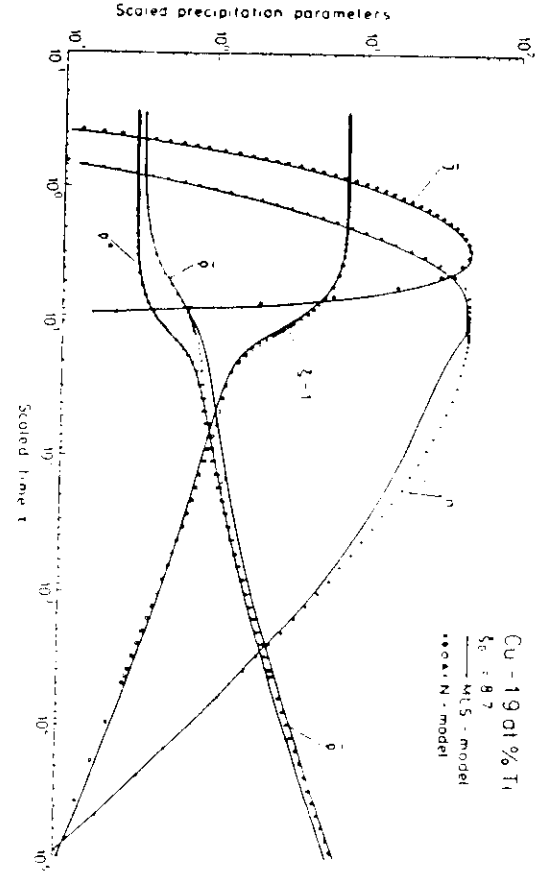
Scaled precipitation parameters
Scaled time τ
Cu - 1.9 at % Ti
ζ_c = 8.7
MLS - model
•••• LSW - model
ζ
ζ - 1
ρ
ρ*
β

Cu - 19 at % Ti
T = 350° C
$\sigma_{\alpha\beta}$ = 0.067 J/m²
D = 2.5 × 10⁻¹⁵ cm²/sec
c_∞ = 1.4 δR*/R* = 0.1
N - model
MLS - model
exp data
Particle radius R, R* / nm
$\bar{R}, \bar{R}_{LS}$
R*
Supersaturation $\frac{\bar{c}}{c_\infty} - 1$
Time t / min

Fig. 5

f(ρ, τ)
Scaled radius ρ
Cu - 19 at % Ti
T = 350° C
N - model
LSW - theory
τ = 1.09
t = 0.15 min
τ = 2.5
t = 0.35 min
τ = 8.3
t = 1.16 min
τ = 14.3
t = 2.0 min
τ = 52.2
t = 7.26 min

Fig. 4

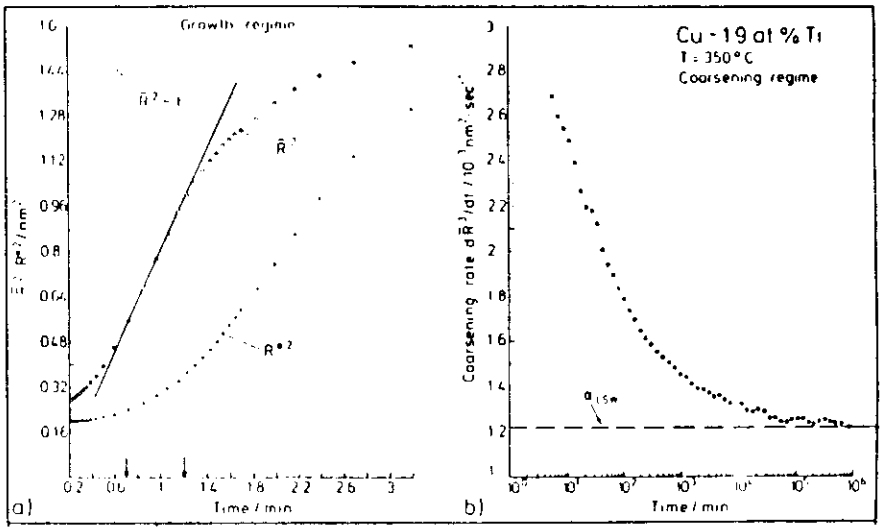
Growth regime
Cu - 19 at % Ti
T = 350°C
Coarsening regime
Time / min
Time / min
a)
b)

(54)

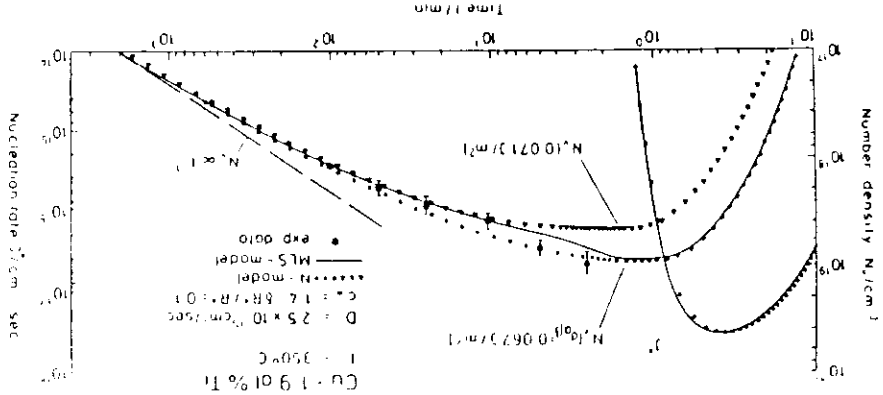
Cu - 1.9 at % Ti
T = 350°C
exp data
Time / min
Number density N_v/cm^-3

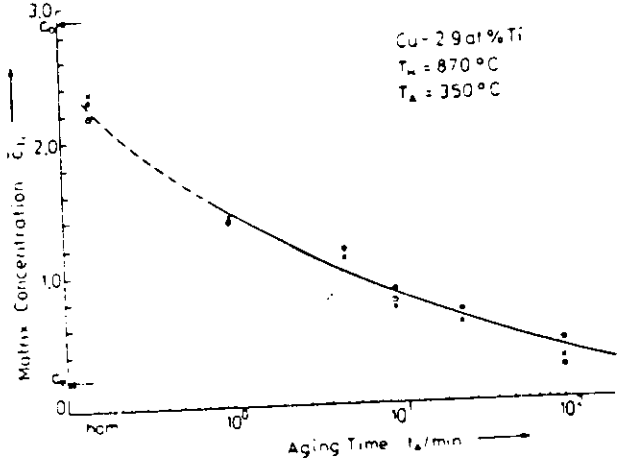
Cu - 2.9 at % Ti
T_H = 870 °C
T_A = 350 °C
Matrix Concentration $\bar{c}_i$
3.0
2.0
1.0
0
c_0
c_∞
hom
10^0
10^1
10^2
Aging Time t_A/min

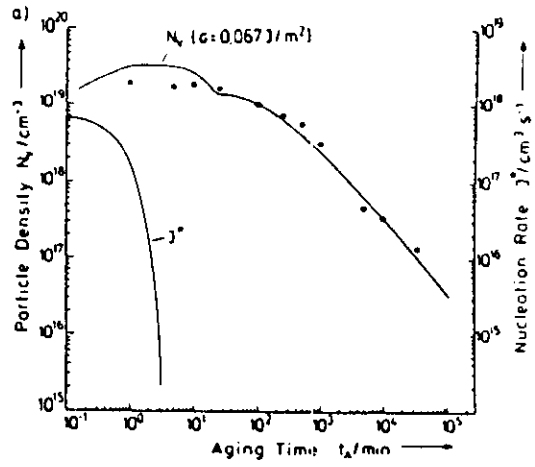
a)
N_V (σ=0.067) / m³)
Particle Density N_V/cm⁻³
Nucleation Rate J^*/cm³ s⁻¹
J^*
10^{20}
10^{19}
10^{18}
10^{17}
10^{16}
10^{15}
10^{-1}
10^0
10^1
10^2
10^3
10^4
10^5
Aging Time t_A/min

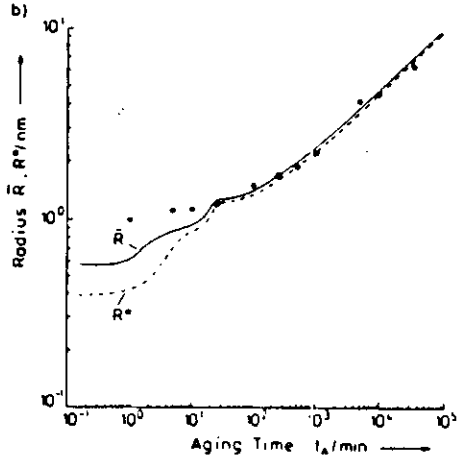
b)
Radius $\bar{R}$, R^*/nm
10^1
10^0
10^{-1}
$\bar{R}$
R^*
10^{-1}
10^0
10^1
10^2
10^3
10^4
10^5
Aging Time t_A/min

Fig. 4 (5) 80

Fig

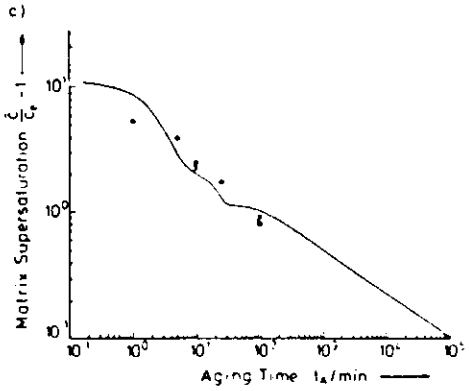

Fig. 4 (57c)

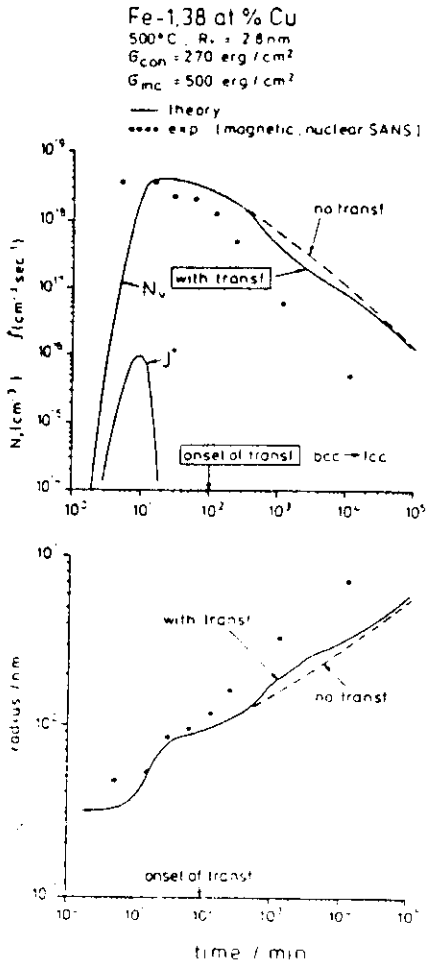

Fig. 4 (58)

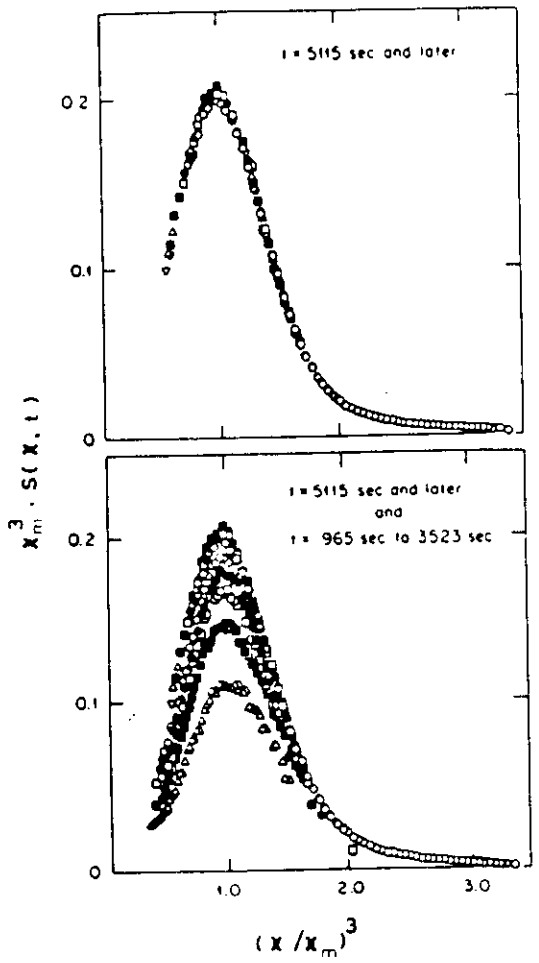
t = 5115 sec and later
t = 5115 sec and later
and
t = 965 sec to 3523 sec
0.2
0.1
0
1.0
2.0
3.0
$x_m^3 \cdot S(x,t)$
$(x/x_m)^3$

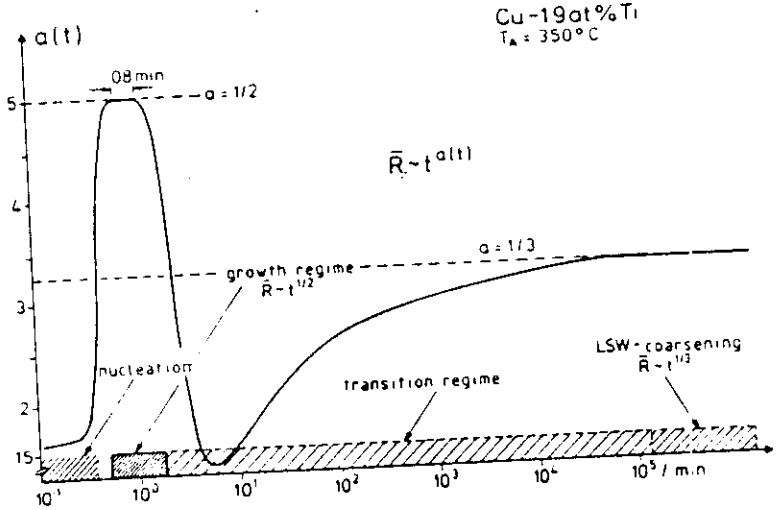
Cu-19at%Ti
T_A = 350°C
a(t)
08 min
a = 1/2
$\bar{R} \sim t^{a(t)}$
growth regime
$\bar{R} \sim t^{1/2}$
a = 1/3
nucleation
transition regime
LSW-coarsening
$\bar{R} \sim t^{1/3}$
5
4
3
2
1.5
10^{-1}
10^{0}
10^{1}
10^{2}
10^{3}
10^{4}
10^{5} / min

Fig. 4 (60)

83

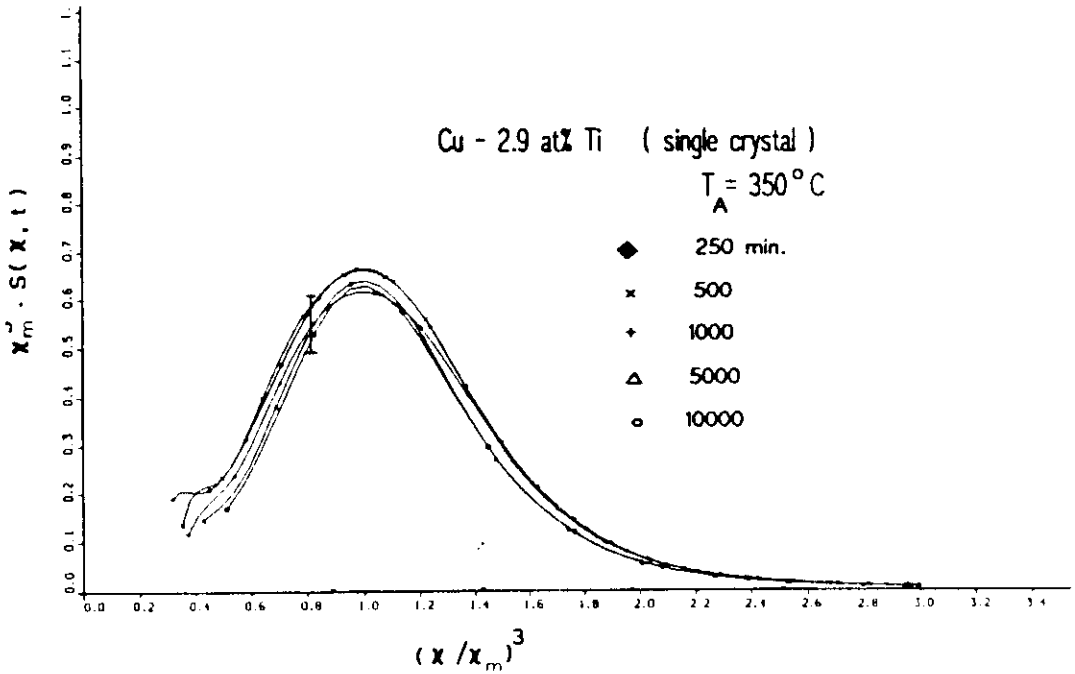
Cu - 2.9 at% Ti (single crystal)
T_A = 350 °C
250 min.
500
1000
5000
10000
$\chi_m^3 \cdot S(\chi, t)$
$(\chi / \chi_m)^3$